# Exploring the use of MODIS forest transmissivity for correcting passive microwave observation of snow-covered terrain/landscape

by

Qinghuan Li

A thesis

presented to the University of Waterloo

in fulfillment of the

thesis requirement for the degree of

Master of Science

in

Geography

Waterloo, Ontario, Canada, 2014

# AUTHOR'S DECLARATION

I hereby declare that I am the sole author of this thesis. This is a true copy of the thesis, including any required final revisions, as accepted by my examiners.

I understand that my thesis may be made electronically available to the public.

# Abstract

Snow is one of the most important parts in Earth's hydrologic cycle especially at high latitude. Observation of snow accumulation by passive microwave measurements is an effective way for estimating snow mass at the regional to hemispheric scales because microwaves have the capability of interacting with the snow and the amount of interaction is controlled by the bulk properties of a snowpack such as snow water equivalent (*SWE*) or snow depth (*SD*). Forest coverage is one of the challenges in the estimation of snow accumulation by passive microwave observations. Canopy can decrease the accuracy of *SWE* retrieval by attenuating microwave emission from the ground and by producing additional emission. Transmissivity of radiation is an important variable that describes how a tree canopy attenuates microwave emission from ground. Although transmissivity can be measured in the field or estimated by models using field data, field data are not always available especially at regional to global scales. Therefore, following the work of Metsamaki *et al*. (2005) a transmissivity model that uses reflectance data from the Moderate Resolution Imaging Spectroradiometer (MODIS) is applied for the retrieval of transmissivity at the hemispheric scale. Called SCAmod, this transmissivity estimation model uses reflectance from full snow covered conditions but can only can be applied in high latitude areas. The MOD44B land cover data set was used to extend SCAmod transmissivity data to lower latitude areas. Results show that SCAmod transmissivity data and MOD44B data are highly correlated, therefore, the application of SCAmod can be extended from regional to global scales.

SCAMod can improve the accuracy of snow mapping, but can also assist in passive microwave (PM) brightness temperature($T_b$) corrections. The influence of vegetation on passive microwave brightness temperatures were explored by compare the $T_b$s in open areas with $T_b$s in forest covered areas. A regression model between the $T_b$s contributed by the vegetation and transmissivity was derived, In general, the brightness temperature contributed by the vegetation increases with the increase of forest vegetation density (decrease of the transmissivity). In the higher frequency bands, vegetation tends to contribute more brightness temperature than lower frequency bands. In H-pol bands, vegetation will contribute more brightness temperature than V-pol bands. This finding can be used to solve *SWE* or *SD* underestimate in the forest region.

## Acknowledgements

The completion of this thesis would not have been possible without the help of a lot of people. I would like to express my most sincere gratitude to them. First and foremost, I want to thank my supervisor Dr. Richard Kelly. He is the person who introduced me into the field of quantitative remote sensing, and generously offered support, guidance and encouragement in my entire Master program. I also offer my deep appreciation to the members of my committee members: Dr. Claude Duguay, Dr. Chris Derksen and Dr. Ellsworth LeDrew. I want give special thanks to my wonderful colleagues: Joshua King, Andrew K, Nastaran Saberi, Aaron Thompson, Mike Brady, Jessie Wen Tang, Jeffrey Chan, John Coughlin, Kevin Kang and Pervaiz Mohammed. Thanks for all your support and encouragements during my Master program. Moreover, I am truly thankful to my friend Ruizhang Jin, who gave me suggestions in mathematics study and Xianda Sun, who gave me support in programing. I thank my good friend Jun Luo, who always cheers me up when I am frustrated and always gives me good suggestions when I am in trouble. Last but most important, I give my deepest gratitude to my parents for their continuous encouragement and unquestioning love.

# Table of Contents

# List of Figures

# List of Tables

# Chapter 1: Introduction

Snow is one of the most important elements in the Cryosphere. Falling snow or snow lying on the ground has an influence on both environment and climate (Folland, *et al.*, 2002). Snow also impacts on human activities, such as industry, transportation and agriculture and this can be especially important in mountainous areas (Eamer, *et al.* 2007).

As one of the most important approaches for snow observation, passive microwave (PM) is widely used especially at global scales. In addition to detecting snow extent, PM observations can be used to measure snow water equivalent (*SWE*) or snow depth (*SD*) and can be used in cloud covered conditions during both day and night. Forest canopy cover, however, is a major challenge for to PM snow estimation approaches. Canopy biomass can reduce the accuracy of *SWE* or *SD* retrieval by attenuating microwave emission from the understory snow and by producing additional emission from the canopy itself. Because forest landscapes are prevalent over wide areas, retrieval of *SWE* or *SD* in forested domains is the key challenge in the estimation of snow properties with PM at the regional scale. In previous studies, forest stem volume is a significant and important variable required to calculate attenuation or transmissivity of PM emission by a forest canopy. Unfortunately, forest stem volume data is not available in much of the world at regional to global scales. Therefore, forest

transmissivity retrieval approaches reliant on forest stem volume data will be limited by the lack of stem volume data for model application at large scales.

Therefore, the aim of this thesis is to estimate forest transmissivity using remote sensing data alone thereby enabling a way of estimating attenuation of PM emission by forests. This study follows the work of Metsamaki *et al*. (2005; 2012) in which reflectance data from MODIS observations are used to estimate transmissivity through a semi-emprirical modeling approach. The estimate of transmissivity is based on VIS/IR data but it is assumed that the transmissivity estimation model is applicable in the microwave domain and has the potential to be applied at global scale.

The work of Metsamaki *et al.* (2005; 2012) is extended from regional to global scales, and then this optical transmissivity product us used to correct forest attenuation in PM brightness temperature measurements by quantifying the nature of microwave brightness temperature interaction with this optical transmissivity product. The specific objectives, are to:

1) extend the work of Metsamaki *et al*. (2012) to northern hemispheres;
2) develop a method to apply the forest transmissivity estimates to correct PM observations in forested terrain;
3) provide an analysis of the uncertainty in the correction procedure of (2);
4) apply the corrections globally to AMSR-E data.

# Chapter 2: Literature review

## 2.1 The importance of snow research

### 2.1.1 Snow and climate change

Snow is linked with climate system in many aspects. Snow has the influence on surface energy budget and temperature at both local and global scales (Karl & Trenberth, 2003; Garcia-Herrera & Barriopedro, 2006). Furthermore, snow cover and depth also effect on atmospheric circulation (Garcia-Herrera & Barriopedro, 2006), water cycle (Mazurkiewicz, *et al.*, 2008), and surface gas exchange (Sommerfeld, *et al.*,1993).

#### 2.1.1.1 The effect of snow on surface energy budget

High reflectivity, high thermal emissivity and low thermal conductivity are the natural characteristics of snow. Moreover, snow is a sink of latent heat for atmosphere when snow is in its melting phase. These characteristics mean that snow cover can influence surface energy exchanges in various ways.

High reflectivity makes snow have a high albedo. Fresh snow can increase the surface albedo by 30-50 % (William, 1965). Table 2.1 shows a comparison of albedos for different surfaces in Arctic landscapes:

| | |
|---|---|
| Fresh Snow | 0.70-0.90 |
| Melting Snow | 0.50-0.60 |
| Water | 0.06-0.10* |
| Dry Tundra | 0.23-0.26 |
| Wet Tundra | 0.10-0.20 |
| Multiyear Sea Ice | 0.55-0.75 |
| Thick First year Sea Ice | 0.30-0.60 |
| Meltponds on sea ice | 0.15-0.40 |
| Boreal forest | 0.08-0.30 |

* Varies widely with solar zenith angle

Table 2.1 Representative albedos for Arctic surfaces(Serreze & Barry, 2014;Betts & Ball, 1997)

In snow covered areas, more solar radiation will be returned back to space compared with non-snow covered surfaces. Surface albedo, snow cover and temperature are, therefore, linked together through a land-atmosphere energy feedback mechanism called the "snow-albedo" feedback (Stephen & Ross, 2007). If temperature increases, snow covered area will decrease, which leads to surface albedo decrease which in turn produces a reduction in reflected solar radiation. The amount of absorbed solar radiation will increase with the decrease of albedo. This process is predicated on the radiation balance at the surface and the net radiation flux ($R_N$) is calculated from:

$$R_N = S_N + L_N = S\downarrow(1-a) + (L\downarrow+L\uparrow) \quad (2.1)$$

where $S_N$ is net short wave flux and $L_N$ the net long wave flux, $S\downarrow$ is downwelling shortwave radiation, $a$ is the snow albedo and $L\downarrow$ and $L\uparrow$ are the downwelling and upward longwave fluxes respectively. According to King *et al*. (2008) if the albedo drops below about 0.75, $R_N$ becomes negative and the snowpack absorbs energy whilst

above this value radiant energy is emitted away from the pack. The effect of clouds, however, is important and can dominate the balance with respect to the longwave radiation flux. So cloud forcing can be significant.

Besides surface albedo, energy exchange at the interface of ground surface and air is moderated if snow cover exists. The thermal characteristics of snow are very different than the underlying soil surface. First of all, snow has a higher thermal emissivity than most natural surfaces. This characteristic makes snow a very effective radiator for losing heat by emitting long-wave radiation. Furthermore, heat above the snow will be converted into latent heat during snow melt, making snow a sink of latent heat from the atmosphere during melt. Finally, fresh snow is an ideal insulator because it has a very low thermal conductivity. Therefore, snow cover can decrease the speed of heat loss from the underlying ground into lower atmospheric layers. This is especially the case at night, when the radiative exchange is concentrated in the surface layers of snow. Studies also show that the temperature of the snow surface may drop by more than 10 degrees overnight, but the soil surface underlying snow cover as thin as 10 cm may only drop by less than 1 degree (Jones,1994). Because of these characteristics, snow can significantly influence the surface heat budget and air temperature; as Wagner (1973) suggested, during winter time, snow makes a strong contribution for temperature moderation.

Snow can also have an environmental cooling effect. First of all, during the daytime, incoming solar radiation absorbed by the ground is decreased by the presence of snow

cover because non-melting snow generally reflects incoming solar radiation to the atmosphere. Furthermore, snow can increase the speed of heat loss by increasing long-wave radiation. Finally, melting snow is a sink for latent heat.

#### 2.1.1.2 The influence of snow cover on temperature and atmospheric circulation.

As a result of local scale processes described above, snow contributes to regional-scale changes of the Earth's surface. Snow can decrease the surface temperature by reflecting solar radiation, increase long-wave radiation emitted from the ground and absorb heat during snow melt. Thus, snow cover can modify the column of air above and, therefore, potentially moderate temperature patterns.

At the local scale, Kukla and Gavin (1981) found that average daily temperature variations for several North Dakota cities were about 10 K different between snow covered and snow free locations. Treidl (1970) also found when warm and moist air flows over the snow covered areas which are greater than 15cm deep, the temperature will be reduced 4 to 5 degrees per day because loss of heat by conduction to the surface. Furthermore, As Lamb (1972) suggested, snow cover on the ground can delay the seasonal warming in early spring if abnormally extensive snow cover persists.

At the global scale, snow also plays an important role in global temperature variations. According to Karl and Trenberth's work (2003), periods of low snow cover due to warmer temperatures +at the global scale makes the planet darker and results in increased absorption of solar radiation. Therefore, the "snow -albedo" feedback will enhance the tendency of temperature increases and snow melt especially in high

altitude regions. This effect has been explored further by Qu and Hall (2007). Furthermore, Northern Hemisphere snow cover anomalies and temperature anomalies are also correlated (Folland, *et al.*, 2002). Since the pattern of the atmospheric circulation is largely determined by the heat distribution and heat exchange process, and the snow on the ground has significant influence on the heat balance of the earth, snow becomes one of the most important factors which not only influences temperature, but also on the atmospheric circulation system.

With respect to atmospheric dynamics, the cooling effect of snow can enhance or maintain a trough of cold air in the troposphere. In turn, the cold trough will favor the persistence of snow cover. This feedback has further influence on the distribution of air pressure and the pattern of air flux. Garcia-Herrera and Barriopedro (2006) explored the snow cover-blocking relationship with a six-step conceptual model. The result suggested that, at the local and subcontinental scales, snow cover and atmospheric blocking are related.

In addition to its effect on atmospheric circulation at local scales, snow cover can also have the influence on the atmospheric circulation system at larger scales. By observing the behavior of anti-cyclone in Asian, North American and Eurasia, Foster *et al*. (1983) suggested that snow cover tends to enhance the strength and decrease the temperature of the anti-cyclone.

### 2.1.2 Snow and ecosystems

Snow is linked with the surface energy budget and atmosphere and, therefore, has a further effect on the ecosystem by influencing temperature, precipitation and wind. At the local scale, both animal and plant communities are shaped by snow in the cold region. Animals and plants evolved some special characteristics to adapt to snow covered condition. For example, animals that live in cold regions have evolved features to adapt to low temperature and snow covered condition. Invertebrate animals cannot maintain their body temperature through the metabolic process, thus usually invertebrate animals have a high mortality when temperatures drop below freezing point. Invertebrate animals in cold regions, however, can withstand lower temperatures by decrease the freezing point of bodily fluids, which reduces mortality at low temperature (Richard, 1991). The majority of vertebrates living in cold regions consist of small mammals (Merritt, 1981) and have adapted to their environment. Many vertebrates, for example, will hibernate, become less active or construct nests to conserve heat during winter. Other animals will have physiological or morphological changes such as increase metabolic rates, reduce the size or increase hair density(Jones, 1999).

In addition to animals, vegetation also has to adapt to low temperature and snow covered conditions in cold regions. The physical characteristics of the snowpack are critically important for vegetation patterns in the boreal forest, tundra and mountain vegetation communities (Walker, *et al.*, 1993). In cold regions, the environment is

harsh for vegetation because both low temperature and strong wind with snow crystals can kill or damage trees above the snow surface. Different strategies are developed by plants for surviving harsh conditions such as trapping snow or retaining dead tissue for insulation and protection, and rapid spring growth and flowering. Some plants can survive under snow in the winter, use snow layer as the insulator and protector (Jones, 1999)

Temperature, atmospheric circulation and precipitation are related. For example, abnormally snow cover in Eurasia has the impact on the Indian monsoon (Barnett, *et al.*, 1989). Therefore, at the global scale, snow cover can influence ecosystems by influence global temperature and precipitation pattern.

## 2.2 Spaceborne VIS/IR and passive microwave observations of snow

Spaceborne observation approaches make the global and daily snow mapping possible and are one of the most important tools to monitor snow cover. First, with spaceborne approaches, the observation area can be wide area in coverage. Especially in some remote areas, the spaceborne approaches can provide long term observations. Furthermore, spaceborne imaging is a reliable daily observation approach. Snow cover condition changes rapidly with temperature and precipitation, thus, daily observation is important. Spaceborne observations can be used to support management decisions and research analysis. Finally, the long term global and daily observation data of snow

provide by the spaceborne approaches are valuable in study climate change and global change.

### 2.2.1 Global VIS/IR based snow mapping

Snow is relatively easy to observe at visible wavelengths from satellites because it has a high reflectance compared with non-snow cover area. The spectral properties of snow in VIS/IR depend on the impurity and grain size of the snow (Winther, *et al.*, 1999). The reflectance of snow decrease with the increase of impurity (Aoki, *et al.*, 2000). The fallout of atmospheric aerosols is the main reason for the increased presence of impurities (Teruo, *et al.*, 2000). Snow grain size is another factor influencing surface reflectance. Grain size changes in response to melting and refreezing processes,, temperature gradient metamorphosis from vapor flow through the snow, and compaction from wind processes (Sturm & Benson, 1997). Spectral reflectance decrease with the increase of grain size. The impurity and the grain size of the snow tends to increase with time, thus, fresh snow has higher reflectance than old snow.

Distinguishing snow and cloud is one of the challenges for visible-infrared remote sensing of snow. Similar to snow, cloud also has high reflectance at VIS bands (Figure 2.1). Because the spectral characteristics of snow and cloud are different at near-infrared wavelength, this problem was largely solved by introducing IR bands, especially at the 1.6 μm wavelength where snow has very low reflectance and cloud a high or medium reflectance (Bunting & d'Entremont, 1982). Using the reflectance

characteristics in VIS and IR bands, snow and cloud can be distinguished in most situations.

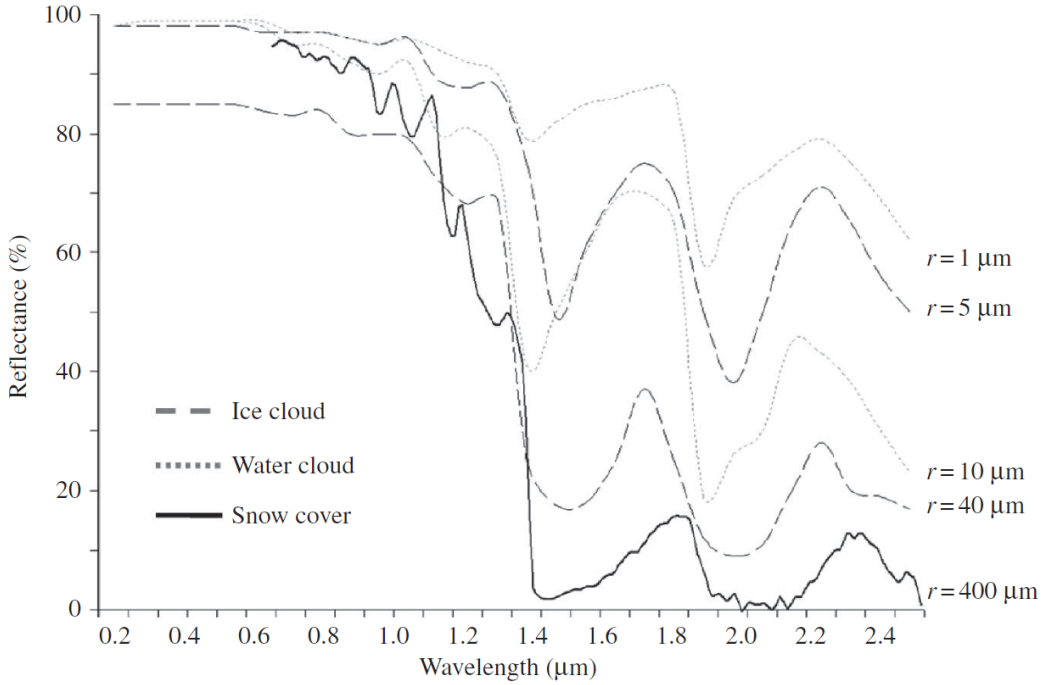


Fig.2.1 Spectral behavior of different cloud types compared with snow at VIS/IR wavelengths and for different grain sizes (r) (Dietz, *et al*., 2012).

In the 1960s, (National Oceanographic and Atmospheric Administration (NOAA ) started to globally observe snow with remote sensing instruments. Today, data sets provided by Advanced Very High Resolution Radiometer (AVHRR) and Moderate Resolution Imaging Spectroradiomete (MODIS) are two of the most important data sets for study globally snow coverage at VIS/IR bands. AVHRR has a more than 40 year record in snow cover extent observation. Since 1972, visible satellite-based snow cover observation started by NOAA (Matson, 1991). The Very High Resolution Radiometer (VHRR) was used as the primary sensor which provide image with 1.0 km spatial

resolution at the beginning. From 1978, the advanced model of VHRR (AVHRR) has been used for estimates. The AVHRR is an imaging sensor which measures the radiance emitted or reflected by the earth-atmosphere. Initially, AVHRR observed the Earth at 4 spectral bands. Then the bands increased to five (AVHRR/2) and six (AVHRR/3). The spatial resolution of this sensor is 1.1 km sub-nadir and swath width is 2922km. AVHRR observations can cover the entire Earth surface once every day (Cracknell, 1997).

The MODIS instrument is a new generation sensor which measures radiances from the Earth in VIS/IR wavelengths. The first MODIS sensor board on Terra spacecraft was launched on December 1999, and the second MODIS sensor lunched with Aqua spacecraft on May 2002. Compared with AVHRR, MODIS has higher spatial resolution (2 bands at 250 m, 5 bands at 500 m and 29 bands at 1 km) and spectral resolution (36 spectral bands ranging in wavelength from 0.4 μm to 14.4 μm) (Matson, 1991). For snow applications, this advantage makes MODIS better able to distinguish land surface objects and to discriminate more effectively snow from most clouds (Hall, *et al.*, 1995).

The MODIS automatic snow mapping algorithm was developed to calculate MODIS snow product operationally. This algorithm uses normalized difference snow index (NDSI) and normalized difference vegetation index(NDVI), enabling MODIS snow products to be more effective to distinguish cloud and snow than other instrument products since they have better ability to deal with the influence of vegetation canopy

(Hall, *et al.*, 1995). The MODIS snow cover product has been tested by comparing against with higher resolution Landsat image and snow products produced by NOAA (Hall, *et al.*, 2005).

### 2.2.2 The application of passive microwave remote sensing in snow research

Passive microwave is another effective tool in global snow observation. PM sensors can be used to measure both snow cover and snow mass at the regional or hemispheric scales. The factors influencing microwave radiation emitted from snowpack including the physical temperature of the snow, the integrated snow grain size, the snow density, and the underlying surface state (soil type, soil water state and moisture content). Microwave sensor responses can also be affected by snow liquid water content. When taken and represented effectively in retrieval algorithms, is possible to estimate depth and water equivalent of snow (Foster, *et al.*, 1984).

Compared with spaceborne VIS/IR sensors, spaceborne PM sensors usually have coarser spatial resolution, but the unique characteristics of microwave make passive microwave approach plays a very important role in snow observation. Microwave wavelengths of are longer than the VIS/IR wavelengths, and cloud or small particles in the atmosphere are transparent to microwaves. Therefore, microwave observations can be made under nearly all weather conditions (Stiles, *et al.*,1981). Furthermore, unlike VIS/IR sensors, the microwave observing sensors are independent of solar illumination, thus, observations can be made in both day and night (Hollinger, *et al.*,1990). In

summary, microwaves can be used for estimating the snow mass because microwaves have the capability of interacting with the snow and the amount of interaction is controlled by the bulk properties of a snowpack such as *SWE* or *SD*. Figure 2.2 illustrates the relationship between snow depth and the brightness temperature response from a snowpack at 37 GHz (vertical and horizontal polarization) indicating an increased scattering response that reduces the observed brightness temperatures at these frequencies (Bernier, 1987).

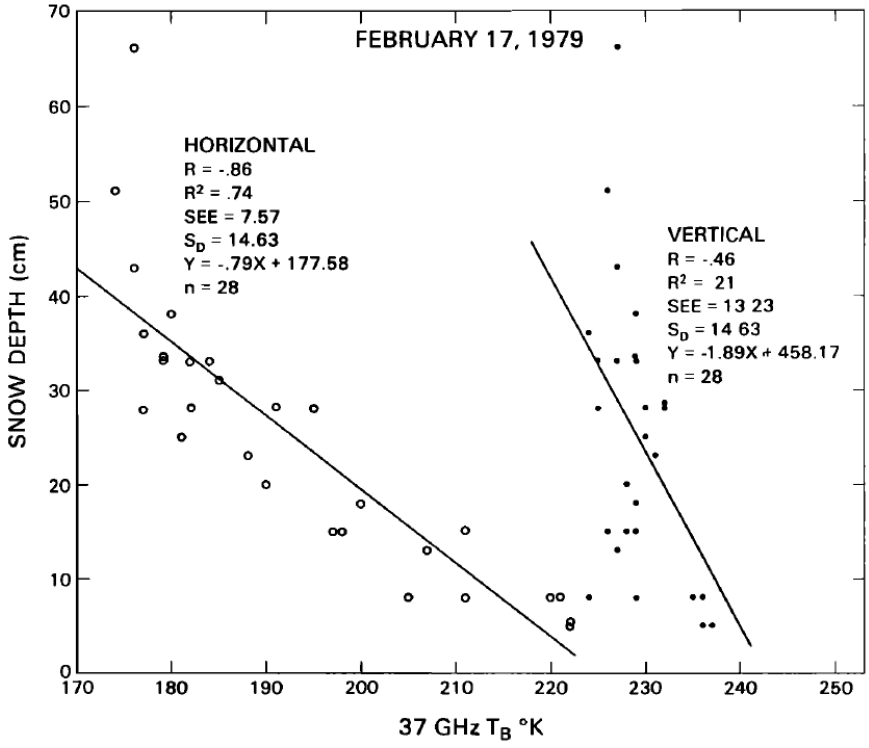


Fig.2.2 The relationship between brightness temperature and snow depth (Foster, *et al.*, 1984)

Because PM sensors can detect the snow beneath clouds and in the darkness albeit at low spatial resolution while VIS/IR observations are adversely impacted by the

presence of cloud but can observe at moderate spatial resolutions, PM sensors can complement each VIS/IR sensor observations for snow mapping (Foster, *et al.*, 2011). What is more, the algorithms to estimate *SWE* and *SD* with PM sensor have been developed in recent 30 years (Debbie, 2010; Foster, *et al*., 1996; Kelly, 2009) and although uncertainty still exists (Foster, *et al.*, 2005), PM approaches is the only spaceborne way to estimate *SWE* and *SD* globally every day and night.

The primary PM sensors used for snow monitoring are SMMR, SSM/I and AMSR-E. Scanning Multichannel Microwave Radiometer (SMMR) was launched with Nimbus-7 in 1978 to continuously observe microwave radiation emitted from the Earth surface. This sensor was developed to obtain sea surface temperatures, wind stress, sea ice coverage and terrain variables (Gloersen & Barath, 1977). Nine years later, Special Sensor Microwave Imager (SSM/I) board on Defense Meteorological Satellite Program (DMSP) launched in 1987. Compared with SMMR, SSM/I has wider swath and improved sensitivity (Hollinger, *et al*., 1990). SSMIS, the upgraded model of SSM/I, started to operate from 2003.

Advanced Microwave Scanning Radiometer - EOS (AMSR-E) was lunched onboard Aqua in 2002. This sensor was used as one of the primary sensors in snow observation. The objective of this sensor is to observe atmospheric, land, oceanic, and cryospheric parameters, including precipitation, sea surface temperatures, sea ice concentrations, snow water equivalent, surface wetness, wind speed, atmospheric cloud water, and water vapor (Lobl, 2001). AMSR-E has 12 channels with 6 frequencies and 2

polarizations. JAXA's Advanced Microwave Scanning Radiometer 2 (AMSR2) on board the Global Change Observation Mission-Water (GCOM-W1) mission is a follow on from AMSR-E and has similar characteristics. Compared with SMMR and SSM/I, AMSR-E/AMSR2 has higher spectral and spatial resolution, better sensitivity and wider swath coverage. The details of PM sensors are represented in Table 1.1:

| | SMMR | SSM/I | AMSR-E |
|---|---|---|---|
| Operational period | 1978-1987 | 1987-present* | 2002- 2011 |
| Platform | Nimbus-7 | DMSP | Aqua |
| Frequencies and IFOV (km x km) | 6.6 GHz; 156 x 156<br>10.7 GHz; 97 x 97<br>18.0 GHz; 60 x 60<br>21.0GHz; 60 x 60<br>37.0 GHz; 30 x 30<br>N/A | N/A<br>N/A<br>19.3 GHz; 69 x 43<br>22.2 GHz; 60 x 40<br>37.0 GHz; 37 x 29<br>85.5 GHz, 15 x 13 | 6.9 GHz; 74 x 43<br>10.6 GHz; 51 x 30<br>18.7 GHz; 27 x 16<br>23.8 GHz; 31 x 18<br>36.5 GHz; 14 x 8<br>89.0 GHz; 6 x 4 |
| Polarizations | H/V | H/V* | H/V |
| Incidence angle (degree) | 49 | 53 | 53 |
| Data acquisition | Every other day | Daily | Daily |
| Swath width | 780 km | 1400 km | 1600 km |
| Sensitivity (K) | 0.9–1.5 | 0.8–1.1 | 0.3–1.1 |

Notes: ⁎F08 - F14 have stopped operation, 22GHz(V) on SSM/I F15 has been degraded by a RADCAL beacon since 2006.

*22.2 GHz channel is only available in vertical polarization.

Table 2.2: Parameters of the PM sensors were used as primary sensors in snow observation (Dietz, *et al.*, 2012)

## 2.3 The challenge posed by the forest vegetation coverage on passive microwave estimates of snow

### 2.3.1 Vegetation's influence on PM measurement

Forest coverage is one of the challenges in the estimation of snow mass by PM observations. Canopy can decrease accuracy of *SWE* or *SD* retrieval by attenuating microwave emission from the ground and by producing additional emission. Because forest landscapes are one of the major land cover types, retrieval of *SWE* or *SD* in forested domains is the key challenge in the estimation of snow properties with passive microwave. The forest canopy can be represented as a dielectric mixture consisting of dielectric elements embedded in a matrix of air (Ulaby & Jedlicka, 1984; Foster *et al.*, 1991). Ferrazzoli and Guerriero (1996) provided a detailed model to describe the forest canopy's influence on the PM measurement based on the radiative transfer theory. Forest layers can be divided into two parts: crowns and trunks. For the crown part, the properties of branches and leaves are the most important elements. For the leaf, the shape (radius and thickness), moisture content, dry matter density and Eulerian angles have major influences on the microwave radiative transfer process. For branches, the branch volume, branch length to radius ratio, moisture content and Eulerian angles have influences on the microwave radiative transfer process. For the trunk part, trunk height, trunk Eulerian angle, trunk moisture content, branch and trunk dry matter density and tree height all influence on the microwave radiative transfer process (Ferrazzoli & Guerriero, 1996). But Ferrazzoli's model requires many parameters (e.g.

water content, the type of leaf, the volume of stem and branch), which limited its application at large scales.

For spaceborne observations, the radiation from the Earth surface (forest canopy, snow pack and ground) received by PM sensors is mixed with the radiation emitted from the atmosphere. As Pulliainen and Grandel (1999) suggested, the major contributions to space borne observed scene brightness temperature in forest covered can be divided as: (1) upward emitted atmospheric radiation; (2) downward emitted reflected atmospheric radiation; (3) downward emitted reflected forest canopy emission contribution; (4) downward emitted reflected snowpack emission contribution; (5) upward emitted soil emission contribution; (6) upward emitted snowpack emission contribution; (7) upward emitted forest canopy emission contribution. These paths are represented in Figure 2.3.

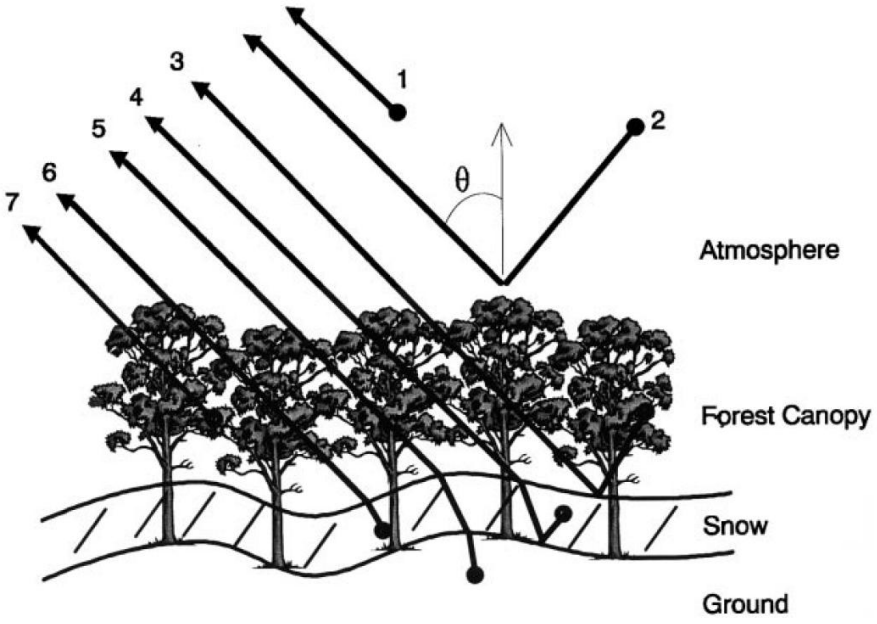


Fig.2.3. Major contributions for space-borne observed scene brightness temperature (Pulliainen & Grandel, 1999)

With the increase of forest density, both emissivity and attenuation will increase, meaning that the radiation emitted from forest layer will gradually overwhelm the emission from the underlying ground as the canopy thickens (Foster *et al.*,1991). In general, in the forest region, although more radiation emitted from the ground will be blocked by the tree canopy with increased attenuation, the measured brightness temperature will increase with the increase of forest density because emissivity from the canopy will increase as illustrated in Fig.2.4 (Kruopis, 1999).

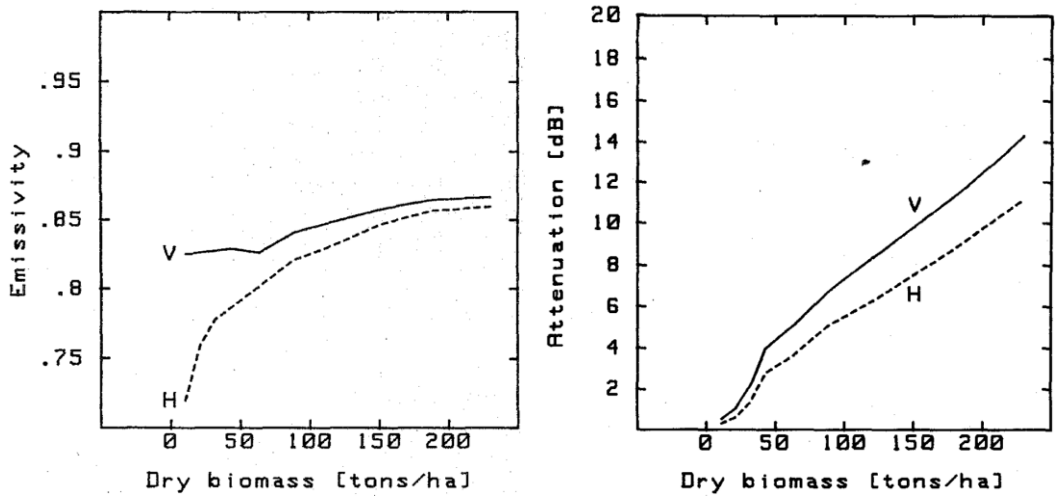


*L band, θ = 45 °

Fig.2.4 Emissivity and crown attenuation of a deciduous forest versus dry biomass at V and H polarizations (Ferrazzoli & Guerriero, 1996)

The consequence of these effects is that the radiation emitted from the below-tree ground may be overwhelmed by the microwave emission from dense forests. Therefore,

the algorithms for retrieval *SD* and *SWE* tend to underestimate at forest covered region (Foster, *et al.*, 1991):

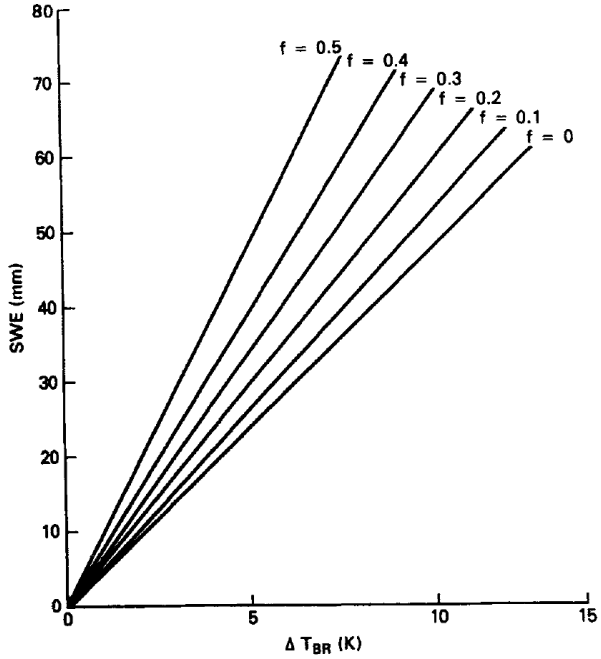


Fig.2.5 Calculated brightness temperature versus *SWE* for different fractional forest cover (Foster, *et al.*, 1991)

### 2.3.2 Correction for PM measurement in forest region

Several studies have attempted to correct the influence of forest in PM measurement. $\Delta T_b$ is the difference in brightness temperature ($T_b$) between the 18 and 37 GHz H-pol. $\Delta T_b$ have been shown to be linearly related with *SWE* and *SD*, which makes retrieval of *SWE* and *SD* with PM sensor possible, at least in principal (Foster, *et al.*,1987; Chang, *et al.*, 2003). However, forest cover will reduce $\Delta T_b$ scattering effect which leads to a negative *SWE* estimation bias when applying these semi-empirical approaches to forest covered areas. By introducing the percentage of forest cover into the original empirical

model, the bias was reduced (Chang, *et al.*, 1996). Foster *et al*. (2005) suggested that because *SWE* (or *SD*) is underestimated in forest areas, and forest fraction is positively correlated with this bias, a correction value (*F* factor) to PM $T_b$s can be applied to correct estimates of *SWE* and *SD*.

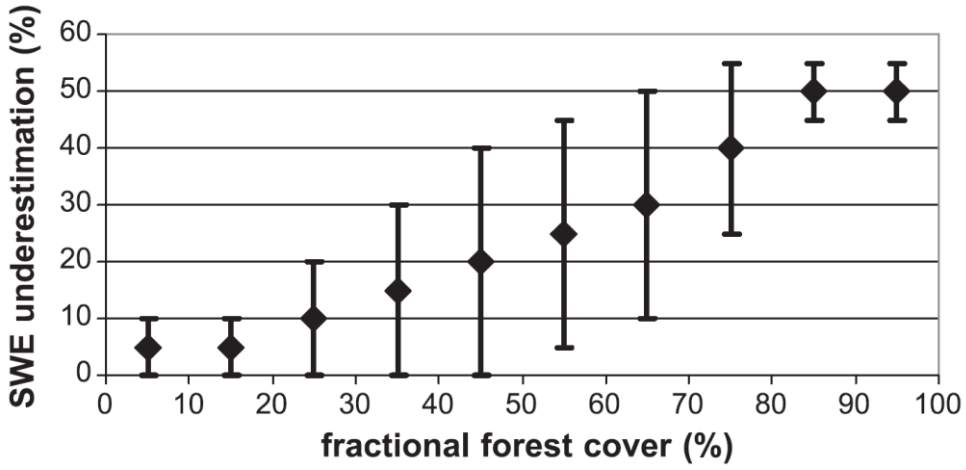


Fig.2.6 Underestimation of *SWE* due to forest covers (Foster, *et al.*, 2005)

The method proposed by Foster *et al*. (2005) only considered the percentage of forest cover, but ignored forest canopy structural variations such that the variations in forest biomass within a forest canopy are ignored. Therefore, more sophisticated models have been developed to improve the correction approach.

In the Helsinki University of Technology (HUT) snow microwave emission model the influence of forest layer was simply described as a function related to forest canopy loss factor (Pulliainen & Grandel, 1999; Butt & Kelly, 2008):

$$T_{b,\,forest} = [1 - \frac{1}{L_{can}^2}(1 - e_{snow})]T_{phys,\,forest} \qquad (2.2)$$

Where $L_{can}$ is forest canopy loss factor, which related with transmissivity: $t = 1/L_{can}$; $e_{snow}$ is emissivity of snow-covered terrain; $T_{phys,forest}$ is the physical temperature of forest layer.

Beside the HUT model, the model developed by Langlois *et al*. (2011) was developed and applied to mixed pixels with dense forests and open areas, making it suitable for air borne observations of snow in forested landscapes (Langlois, *et al.*, 2011). The function of this model can be represented as below:

$$T_{b,FOV} = FtT_{b,snow}(1-\frac{T_{phys,veg}}{T_{phys,snow}}) - Ft^2(1-\frac{T_{b,snow}}{T_{phys,snow}})T_{phys,veg} + (1-F)T_{b,snow} + FT_{phys,veg} \quad (2.3)$$

Where, $T_{b,FOV}$ is the brightness temperature in the field of view; $F$ is the forest cover fraction($F$ = 1 means completely covered by forest); $t$ is the transmissivity; $T_{b,snow}$ and $T_{b,veg}$ is the brightness temperature of snow and vegetation; $T_{phys,veg}$ and $T_{phys,snow}$ are the physical temperature of vegetation and snow.

A third model, the $\omega$-$\tau$ model, is another model that can be used to describe the influence of forest layer on PM measurement. This model simplified the parameters of forest layer into two parameters: optical depth $\tau$ and single-scattering albedo $\omega$ (Pampaloni & Paloscia, 1985; Mo, *et al.*, 2012; Roy, *et al.*, 2012):

$$T_{b,forest} = T_{b,surface} + T_{b,veg} + T_{b,veg\text{-}r} \quad (2.4)$$

$$T_{b,surace} = te_{surface}T_{phys,surface} \quad (2.4a)$$

$$T_{b,veg} = (1-\omega)(1-t)T_{phys,veg} \quad (2.4b)$$

$$T_{b,veg\text{-}r} = t(1-\omega)(1-t)(1-e_{surface})T_{phys,veg} \quad (2.4c)$$

Where $T_{b,forest}$ is the brightness temperature measured over a forest canopy; $T_{b,surface}$ is the emission of the surface under the canopy attenuated by the forest; $T_{b,veg}$ is the emission from forest; $T_{b,veg-r}$ is the downwelling forest emission reflected by the surface; $e_{surface}$ is the emissivity of the surface; and $T_{phys,veg}$ is the physical temperature of vegetation. $\omega$ is the single scattering albedo. Former studies show, the value of $\omega$ can be considered as a frequency independent parameter with a value of about 0.06 (Kerr, *et al.*, 2006; Roy, *et al.* 2012).. Because this value is small, some studies will neglect $\omega$ (Kruopis, 1999; Langlois, *et al.*, 2011) ; $t$ is transmissivity, and $t = exp(-\tau/cos\theta)$.

According to equations 2.2, 2.3 and, 2.4, transmissivity is one of the most important parameters for estimating snow in forest canopies in all three approaches. For retrieval transmissivity, the empirical model has been made based on ground and airborne measured data. For HUT model, the transmissivity was modeled based on the empirical relationship between transmissivity, frequency and stem volume as the one suggested by Kruopis *et al*. (1999) based on European Multisensor Airborne Campaign (EMAC-94/95). Roy *et al*. (2012) adapted $\omega$-$\tau$ model to fit the scale of AMSR-E, but the transmissivity retrieval procedure followed the same approach developed for airborne observations:

$$t = t(f, SV_{high}) + [1 - t(f, SV_{high})]e^{-0.0035SV} \quad (2.5a)$$

$$t(f, SV_{high}) = 0.42 + [1 - 0.42]e^{0.028f} \quad (2.5b)$$

Where $t(f, SV_{high})$ is the frequency dependent transmissivity of a very dense forest, the saturation value of forest transmissivity at a certain frequency. *SV* is the forest stem volume ($m^3$/ha), *f* is the frequency (GHz).

In the study by Langlois *et al.* (2011) based on airborne data provide by IPY (International Polar Year) campaign, forest transmissivity was estimated by comparing brightness temperaturse of forest covered areas with nearby open area. Then, they re-estimated the parameters of the model as suggested by Kruopis (1999).

# Chapter 3: Methodology

The methodology of this thesis falls into four sections that address the overall aims and specific objectives of the study. Section 3.1 describes the data sets used while section 3.2 discusses how forest transmissivity is calculated using the Metsamaki *et al.* (2012) approach. Section 3.3 then describes the implementation of the transmissivity calculations to the global scale while section 3.4 describes how the uncertainty estimates are estimated.

## 3.1 Data sets used

The data used in this study were obtained from instruments aboard the National Aeronatics and Space Administration's (NASA) Aqua and Terra platforms. Terra and Aqua are two of the major components of the NASA's Earth Observing System (EOS).

Terra was the first EOS platform to be launched on December 18, 1999. This satellite has sun-synchronous, near-polar, circular orbit. The local equatorial crossing time is approximately 10:30 a.m. in descending node. The onboard sensors including: Advanced Spaceborne Thermal Emission and Reflection Radiometer (ASTER), Clouds and the Earth's Radiant Energy System (CERES), Multi-angle Imaging SpectroRadiometer(MISR), Moderate-resolution Imaging Spectroradiometer (MODIS) and Measurements of Pollution in the Troposphere(MOPITT) . Those instruments can be used to observe the atmosphere, land surface, oceans, snow and ice and energy budget.

Aqua was launched on May 4, 2002. The major mission for this satellite is to collect the information about the Earth's water cycle. As Terra, Aqua has sun-synchronous, near-polar, circular orbit, but the local equatorial crossing time is approximately 1:30 p.m. in an ascending node instead of 10:30 a.m.. Onboard sensors including: Advanced Microwave Scanning Radiometer-EOS (AMSR-E), Moderate Resolution Imaging Spectroradiometer (MODIS), Advanced Microwave Sounding Unit (AMSU-A), Atmospheric Infrared Sounder (AIRS), Humidity Sounder for Brazil (HSB) and Clouds and the Earth's Radiant Energy System (CERES).

Most data in this study was collected by MODIS and AMSR-E. MODIS was installed in both Terra and Aqua platforms. MODIS can observe the whole earth within 1 or 2 days. MODIS has 36 spectral bands cover the range of wavelength from 0.4 μm to 14.4 μm. Spatial resolutions is different in different bands: bands 1 to 2 at 250 m, bands 3 to 7 at 500 m, and bands 8 to 36 at 1 km.

AMSR-E was installed on Aqua. This is a twelve-channel, six-frequency, passive-microwave radiometer system. It measures horizontally and vertically polarized brightness temperatures at 6.9 GHz, 10.7 GHz, 18.7 GHz, 23.8 GHz, 36.5 GHz, and 89.0 GHz The spatial resolution of the individual measurements varies from 5.4 km at 89 GHz to 56 km at 6.9 GHz (Lobl, 2001).

### 3.1.1 MODIS data

#### 3.1.1.1 MOD09A1: surface reflectance

MOD09A1 reflectance data (collection 5) from 2010-2014 during winter time was used for estimating transmissivity. Selected tiles that covered the entire continental area at latitudes greater than 45 degree north were chosen for the northern hemisphere.

MOD09A1 is a level 3 MODIS surface reflectance product which combines the best possible L2G observation during an 8-day period (Vermote, *el at.*, 1997). In this study, green band (550nm) was used.

After atmospheric correction, the top of the atmosphere signal is converted to surface reflectance. This means, that the core of this MODIS surface reflectance algorithm is atmospherically corrected. According to the uncertainty estimate by running Second Simulation of the Satellite Signal in the Solar Spectrum (6s) model (Vermote, *et al.*, 1997), the relative error of MODIS surface reflectance produce is in the range of 5-12%. Liang *et al.* (2002) compared MODIS surface reflectance values with Landsat reflectance data, and found that the accuracy of MODIS surface reflectance values is within ±5% of the Landsat data.

In this study, data selection is based on quality assurance (QA) band inside each file. Only the pixels with high observation coverage, solar zenith greater than 86 degrees, and that are not affected by clouds, cloud shadow or aerosol can be selected.

#### 3.1.1.2 MOD44B: vegetation continuous field

MOD44B are used to extend transmissivity product to lower latitude area in this study. The Terra MODIS Vegetation Continuous Fields (VCF) product is designed to represent vegetation coverage estimation globally at 500 m spatial resoution. This product is generated from regression trees with machine learning technology.

The input surface reflectance files to the model which calculate VCF product been divided into 8 time periods. For the VCF product, the quality of input surface reflectance files was used to evaluate the quality of VCF. For input surface reflectance files, cloudy, high aerosol contamination cloud shadow, or view zenith greater than 45 degree were considered poor quality. In this study, therefore, VCF data were chosen when input surface reflectance files were evaluated as good quality at least in one time period (Hansen, *et al.*,2003).

Selected VCF tiles covered the entire continental area of the northern hemisphere. Data in the fall of 2010 were used to study the relationship between transmissivity and tree coverage.

#### 3.1.1.3 MCD12Q1: land cover product

MCD12Q1 is Terra and Aqua Combined Land Cover product. This data set is used for change detection of forest coverage change during the uncertainty assessment part (section 2.4.1.1). This product is derived through a supervised decision-tree classification method. The primary land cover scheme identifies 17 classes defined by the IGBP, including 11 natural vegetation classes, three human-altered classes, and

three non-vegetated classes (Strahler, 1999). 35 tiles were selected to cover the area at latitudes greater than 30 latitude north, data from 2002 to 2012 in whose tiles were used for study forest coverage variation.

3.1.1.4 MYD11_L2: land surface skin temperature

The MYD11_L2 product provides per-pixel physical temperature at 1km resolution across the swath. Data for 2006 October 11 around 1 am were used to standardize brightness temperature in this thesis (equations 3.7 and 3.8).

This daily dataset is produced at 5 arc-minute increments, and covers both daytime and nighttime acquisitions including the polar regions under cloud-free conditions. The product has been validated via a series of field campaigns conducted in 2000-2007, and over more locations and time periods through radiance-based validation studies. The product accuracy for the study areas in this thesis is better than 1K (0.5K in most cases) (Coll, *et al.*, 2009).

### 3.1.2 AMSR-E data

The Advanced Microwave Scanning Radiometer - Earth Observing System (AMSR-E) instrument on NASA's Aqua satellite provides twice daily near-global passive microwave measurements of terrestrial, oceanic, and atmospheric variables for the investigation of global water and energy cycles. The AMSR-E Level-2A product (AE_L2A) contains brightness temperatures at 6.9 GHz, 10.7 GHz, 18.7 GHz, 23.8 GHz, 36.5 GHz, and 89.0 GHz (Ashcroft & Frank, 2013). Ascending data for 2006

October 11 ascending orbit was used in this thesis because it coincided with the MODIS skin temperature data (MYD11_L2).

| Center Freq(GHz) | 6.9 | 10.7 | 18.7 | 23.8 | 36.5 | 89.0 |
|---|---|---|---|---|---|---|
| Band Width(MHz) | 350 | 100 | 200 | 400 | 1000 | 3000 |
| Sensitivity(K) | 0.3 | 0.6 | 0.6 | 0.6 | 0.6 | 1.1 |
| IFOV(km x km) | 76 x 44 | 49 x 28 | 28 x 16 | 31 x 18 | 14 x 8 | 6 x 4 |

Table 3.1 AMSR-E sensor Characteristics

In this study, pre-snow season AMSR-E data in descending orbit mode were acquired and reprojected to 25km EASE grid. Descending orbit data were obtained at about 1:30 am local time when the temperature at this time is more stable from day to day. The study was conducted before the snow season because variations in snow depth in different areas will increase uncertainty when comparing brightness temperature between vegetation covered area and open area. Prior to the snow season, deciduous trees have shed their leaves and the vegetation canopy structure is very close to winter status.

### 3.1.3 Emissivity data

Emissivity data were provided by NSIDC. This data set is a monthly global land emissivity product based on the work of Prigent *et al.* (1997) and Norouzi *et al*. (2011).

In this study, October data were used to standardize brightness temperature in (equations 3.7 and 3.8).

The standard deviation of emissivity estimates for each month is less than 0.015. The uncertainty in atmospheric water vapor profile and physical skin temperature estimation are two major uncertainty sources in these data.

## 3.2 Global forest transmissivity estimate

### 3.2.1 General equation of SCAmod

SCAmod model was developed by the Finnish Environment Institute. It compares reflectance variation in forest-covered areas during snow free and snow covered condition and the high reflectance of snow compared with other natural targets. This model provides an effective way to measure forest transmissivity. It has been tested in Finland (Metsämäki, *et al.*, 2005), Russia and Europe (Metsamaki, *et al.*, 2012), the results from the use of the transmissivity data indicate that SCAmod is improved.

The function below is the first principle in this method. In forest covered areas, observed wavelength-dependent reflectance from a target, $\rho_{\lambda,obs}(SCA)$, is comprised of surface scattering from the ground and volume scattering from the forest canopy layer:

$$\rho_{\lambda,obs}(SCA) = (1-t_\lambda^2)\rho_{\lambda\ veg} + t_\lambda^2[SCA\rho_{\lambda\ snow} + (1-SCA)\rho_{\lambda\ ground}] \quad (3.1)$$

The volume scattering from the canopy is:

$$(1-t_\lambda^2)\rho_{\lambda,veg} \quad (3.1a)$$

and the surface scattering from ground is:

$$t_\lambda^2[SCA\rho_{\lambda,snow} + (1-SCA)\rho_{\lambda,ground}] \quad (3.1b)$$

Where $\rho_{\lambda,veg}$, $\rho_{\lambda,snow}$ and $\rho_{\lambda,\text{ground}}$ are the generally applicable reflectance contributions and are wavelength-specific reflectances of forest, snow and underlying bare ground respectively. It is the empirical value of generally applicable reflectance of snow, snow-free ground and forest canopy at wavelength $\lambda$. $t_\lambda$ is the effective transmissivity which describes the attenuation effect of vegetation canopy to radiation. For this thesis, the goal is to correct specifically for forest attenuation so that the subscript "veg" refers specifically to forest covered terrain. For the retrieval of forest transmissivity $t_\lambda^2$, equation 3.1 can be expressed as follows if SCA equal to 1. This means that if the reflectance at fully snow covered condition is known, forest transmissivity can be calculated:

$$t_\lambda^2 = \frac{\rho_{\lambda,obs}(SCA=1) - \rho_{\lambda,veg}}{\rho_{\lambda,drysnow} - \rho_{\lambda,veg}} \quad (3.2)$$

Where $\rho_{\lambda,obs}(SCA=1)$ is the observed reflectance at full dry snow cover conditions, $\rho_{\lambda,drysnow}$ is generally applicable reflectance contributor of dry snow.

### 3.2.2 Application in MODIS

Band 4 (550 nm) was selected for use in this study because it is sensitive to forest reflectance Pixels under clear-sky condition and highest quality in Quality Assessment layer (QA) were selected for transmissivity retrieval. Water flags were applied to mask water bodies. Snow coverage is identified based on both visual interpretation and the

presence of a Snow Flag in QA layer. Snow coverage over 80% is considered as a full snow condition. $\rho_{550,obs}(SCA=1)$ is the reflectance value in full snow covered condition at 550 nm.

Following the suggestion provided by the law of error propagation (Taylor, 1997), More than 7 observations were taken for each pixel for most areas. The average value for each pixel and the value of variance were calculated by equation 3.3 and equation 3.4:

$$\rho_{550,\ averge}(SCA=1)=\frac{\sum_{i=1}^{N_{obs}}\rho_{550,\ obs\ i}}{N_{obs}} \tag{3.3}$$

$$S^2_{550,obs}(SCA=1)=\frac{\sum_{i=1}^{N_{obs}}(\rho_{550,\ i}-\rho_{550,averge}(SCA=1)^2)}{N_{obs}-1} \tag{3.4}$$

Where $\rho_{550,averge}(SCA=1)$ is the average value of reflectance for each pixel in 550nm and full snow covered condition. $S^2_{550,obs}(SCA=1)$ is the variance of $\rho_{550,obs}(SCA=1)$, $\rho_i$ is the reflectance in scene i, and $N_{obs}$ is the number of observation in each pixel.

The value of generally applicable reflectance contributors are determined by the mean value of sample points based on both Land Cover Type product (IGBP) and visual interpretation. For forest and forest-free ground, sample points were taken before the onset of snow cover. For dry snow and wet snow, the sample points were taken at the snow covered area.

For the dry snow, wet snow and bare ground, 300 representative pixels were selected as sample points. For forest, reflectance was studied by different forest type with 600 representative pixels selected in total; each forest type has 100 sample points.

| | $\rho_{550,\text{drysnow}}$ | $\rho_{550,snow}$ | $\rho_{550,\text{ground}}$ |
|---|---|---|---|
| Mean Reflectance (%) | 83.57 | 69.23 | 8.98 |
| $S^2$ | 1.21 | 4.32 | 3.37 |

| | $\rho_{550,\text{EN}}$ | $\rho_{550,\text{EB}}$ | $\rho_{550,\text{DN}}$ | $\rho_{550,\text{DB}}$ | $\rho_{550,\text{mix}}$ | $\rho_{550,\text{total}}$ |
|---|---|---|---|---|---|---|
| Mean Reflectance (%) | 2.77 | 3.15 | 5.33 | 4.73 | 3.34 | 3.89 |
| $S^2$ | 0.38 | 0.54 | 1.44 | 0.47 | 0.97 | 1.75 |

Table 3.2 Mean and variances of generally applicable reflectance contributors

Table 3.2 shows the mean and variance of reflectances of dry snow, snow and ground ($\rho_{550,\text{drysnow}}$, $\rho_{550,snow}$ and $\rho_{550,\text{ground}}$ respectively). and for evergreen needle-leaf forest, evergreen broad-leaf forest, deciduous needle-leaf forest, deciduous needle-leaf and forest mixed ($\rho_{550,\text{EN}}$, $\rho_{550,\text{EB}}$, $\rho_{550,\text{DN}}$, $\rho_{550,\text{DB}}$ and $\rho_{550,\text{mix}}$ respectively). $\rho_{550,\text{total}}$ is the reflectance of forest in general, this value as calculated from all the selected forest samples.

According to Table 3.2, evergreen needle-leaf forest has the lowest reflectance, and deciduous needle-leaf forest has the highest reflectance. Since the difference of the

reflectance among different forest type is not obvious, $\rho_{550,\text{total}}$ has the ability to represent reflectance of forest canopy in general.

By knowing the value of all the variables, the forest effective transmissivity value was retrieved by equation 3.5:

$$t_{550}^2 = \frac{\rho_{550,averge}(SCA=1) - \rho_{550,veg}}{\rho_{550,drysnow} - \rho_{550,veg}} \tag{3.5}$$

Where $\rho_{550,\text{veg}}$ is reflectance of canopy in 550nm, the value of $\rho_{550,\text{total}}$ was used as $\rho_{550,\text{veg}}$. $\rho_{550,\text{drysnow}}$ is the reflectance of dry snow at 550nm.

### 3.2.3 The relationship between forest transmissivity and tree coverage

Forest transmissivity calculated by the SCAmod method is not globally implementable because the approach cannot be applied in low snow cover or snow free areas; the method requires full snow cover conditions. What is more, cloud coverage is another difficulty in obtaining forest transmissivity with this method. In order to extend the coverage of transmissivity product, forest spatial fraction data from MOD44 data are used because forest transmissivity and forest fraction have the strong correlation. Whilst this is not optimal, it provides a potential means for extending the product to more southerly regions.

For better understanding the relationship between forest transmissivity and forest fraction in globally scale, both forest transmissivity product and the MOD44B product were projected to 25km EASE grid to enable a comparison. Because spatial resolution of 500m sinusoidal projected data is much higher than 25km EASE grid, the value for

each EASE grid pixel is the mean value of the 500m sinusoidal data in equivalent location. Because cloud cover and low snow coverage, forest transmissivity estimated by SCAmod is not always available at 500m resolution, and so the value of 25km EASE grid for each pixel was considered as valid only when more than 90 percent of forest transmissivity data in 500m sinusoidal projection available within the 25 km EASE grid cell. For $S_t^2(\rho_{550,averge}(SCA=1)) < 1$, forest transmissivity value was used to estimate a linear least squares fit regression model between forest transmissivity and forest fraction. Forest transmissivity at global scale was then estimated by the forest fraction with this regression model. This estimated forest transmissivity was used to correct passive microwave brightness temperature at global scale.

## 3.3 Correcting passive microwave brightness temperature with MODIS forest transmissivity data

The premise for brightness temperature correction is straightforward: estimation of the vegetation contribution to brightness temperature ($\Delta T_{b\text{-}vegetation}$) is achieved by comparing the difference in brightness temperature between the forest region and a nearby open area. To achieve this comparsion, a three step procedure was made. The first step was to select brightness temperature data within each transect. The purpose of this step was to restrict the distance between compared forest region and open area so that the general conditions were relatively consistent. Furthermore, for each transect, grid cells with water coverage greater than 50% were avoided. In addition to vegetation emission effects, the landscape physical temperature is another factor

which will influence brightness temperature. The second step, therefore, was to minimize the influence of the physical temperature by standardizing the brightness temperature. Finally, the third step was to estimate the contribution to the brightness temperature of vegetation, $\Delta T_{b\text{-}vegetation}$. Finally, regression models between $\Delta T_{b\text{-}vegetation}$ at different frequencies and transmissivity can be made the correction procedure.

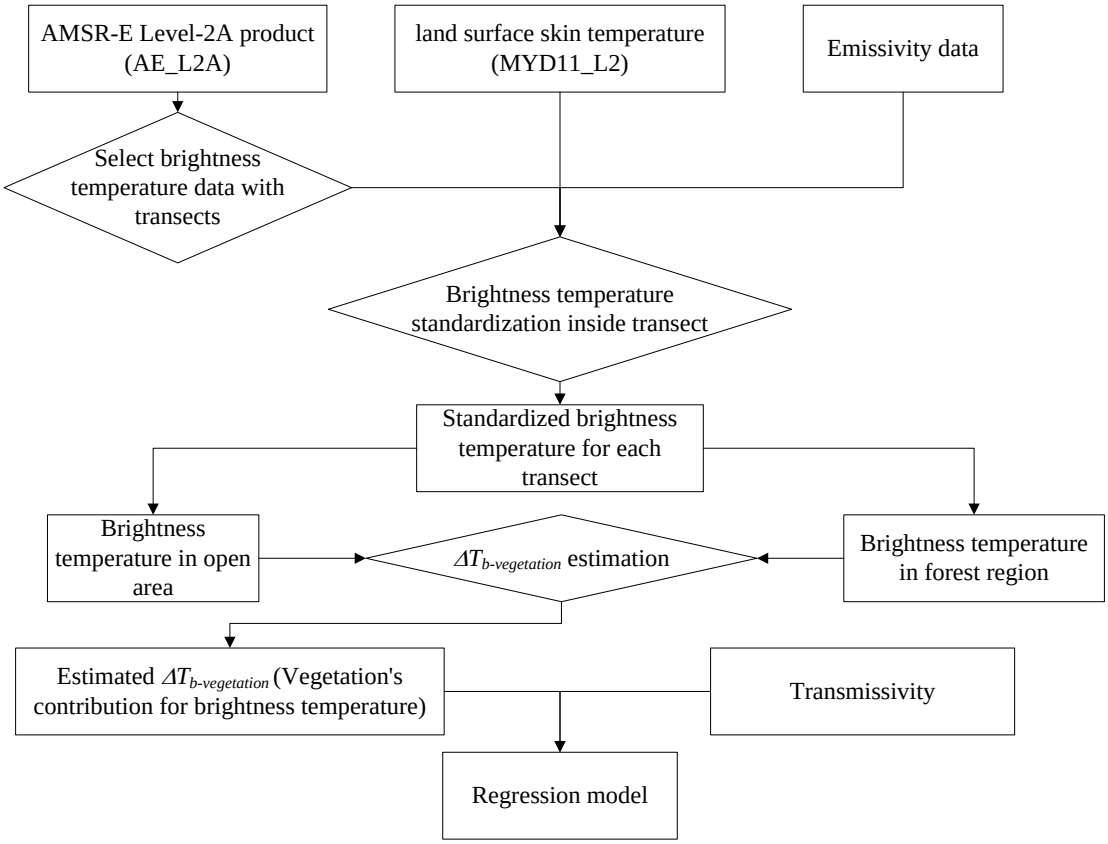


Fig.3.1 Flow diagram for brightness temperature correcting procedure

### 3.3.1 Transect identification

Eight transects were identified in this study with each transect representing a line of sample set which cross the forest covered area to the open area. Each transect is used

to represent nearby forest and ground condition like the density of canopy and the texture of soil. By comparing open area with the nearby forest covered area inside transect, the contribution of vegetation can be estimated.

Each transect used in the present study covered both high forest transmissivity area and low transmissivity area (see Fig.3.1). High percentage water grid cells (percentage of water greater than 50%) are masked out based on reporjected IGBP MODIS landcover product. Physical temperature is another major factor that could affect AMSR-E brightness temperature. Therefore, land surface temperature was also considered in the transect selection. The difference of highest and lowest physical temperature ($\Delta T$) for each transect was less than 15k.

Land surface temperature product MYD11L2, coincident with AMSR-E sensor observations, were used to explore the PM corrections. Since the key objective of this research is to correct AMSR-E brightness temperature for snow measurement, transects were chosen at latitudes greater than 30 ℃N.

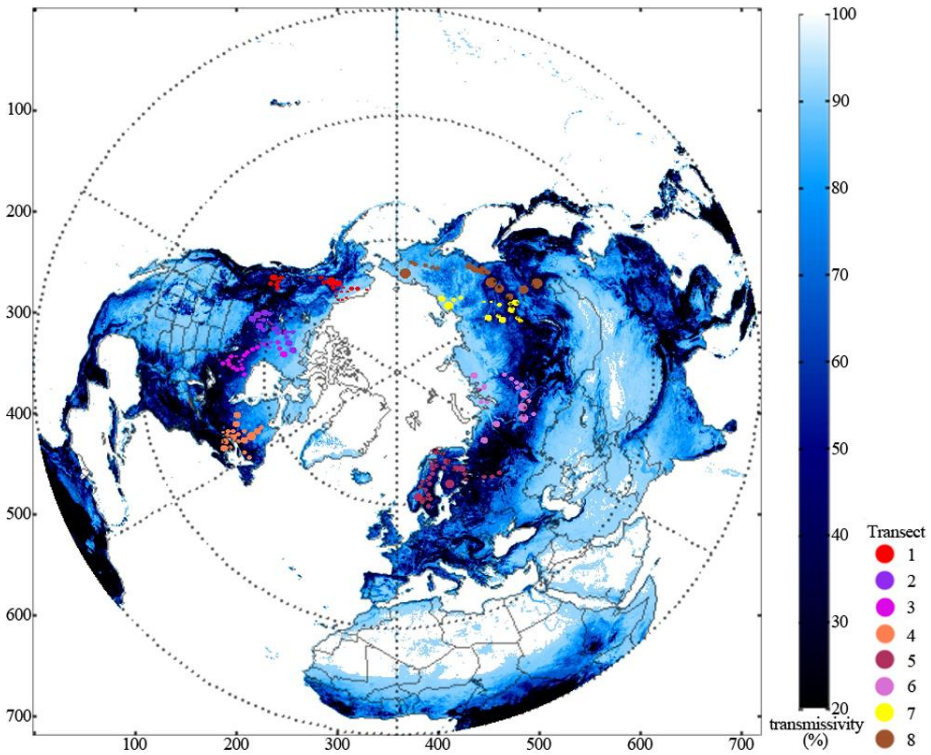


Fig.3.2 Selected transects under forest transmissivity map

| Transect ID | Highest temperature(K) | Lowest temperature(K) | $\Delta T$(K) | Average temperature(K) |
|---|---|---|---|---|
| 1 | 263.68 | 250.46 | 13.22 | 256.52 |
| 2 | 263.12 | 251.04 | 12.08 | 257.60 |
| 3 | 269.76 | 255.04 | 14.72 | 263.22 |
| 4 | 279.36 | 265.60 | 12.54 | 271.56 |
| 5 | 269.44 | 256.52 | 12.92 | 262.66 |
| 6 | 268.92 | 255.90 | 13.02 | 262.56 |
| 7 | 274.98 | 260.00 | 14.98 | 267.42 |
| 8 | 279.50 | 265.80 | 13.70 | 272.53 |
| Average | 271.10 | 257.55 | 13.40 | 264.26 |

Table 3.3(a) Description for each transect

| Transect ID | 1 | 2 | 3 | 4 | 5 | 6 | 7 | 8 |
|---|---|---|---|---|---|---|---|---|
| Sample size for transect (pixels) | 568 | 302 | 382 | 527 | 331 | 228 | 461 | 276 |
| Sample size for ground (pixels) | 158 | 106 | 88 | 68 | 72 | 36 | 65 | 52 |
| Range of transmissivity (%) | 44 to 93 | 29 to 93 | 37 to 93 | 35 to 93 | 41 to 93 | 42 to 93 | 30 to 93 | 40 to 93 |

Table 3.3(b) Description for each transect

### 3.3.2 Standardization brightness temperature inside transect

Although the influence of physical temperature on brightness temperature has been considered when transects selection, 15k difference inside each transect is still significant. For a better understanding of the relationship between vegetation and brightness temperature, the influence of physical temperature on brightness temperature must be minimized.

In the present study, the physical temperature for each pixel is defined as $T$ and the average temperature for each transect is represented by $T_{average}$. By introducing AMSR-E emissivity product, the brightness temperature under physical temperature $T$ for each pixel inside transect can be converted to the brightness temperature under the average temperature $T_{average}$. Therefore, the standardized brightness temperature was used to study the relationship between vegetation and brightness temperature.

The relationship between brightness temperature and physical temperature is defined by the following equation:

$$T_b = eT_{phy} \quad (3.6)$$

Where $T_b$ is brightness temperature, $T_{phy}$ represent physical temperature and $e$ means emissivity. Accordingly, the difference of brightness temperature $\Delta T_b$ for each pixel between temperature $T$ and $T_{average}$ can be expressed as:

$$\Delta T_b = e\,(T - T_{average}) \quad (3.7)$$

The standardized brightness temperature $T_{b\text{-}standardized}$ is defined as the differences between $T_b$ and $\Delta T_b$:

$$T_{b\text{-}standardized} = T_b - \Delta T_b \quad (3.8)$$

### 3.3.3 Brightness temperature contributed by vegetation

The standardized brightness temperature was used to study the brightness temperature contributed by vegetation. Assume ground condition inside each transect is similar, The brightness temperature of ground $T_{b\text{-}ground}$ is similar with the brightness temperature of nearby open area $T_{b\text{-}openarea}$. Defined transmissivity over 0.85 as open area, the brightness temperature of ground can be estimated:

$$T_{b-ground} = \frac{\sum_{i=0}^{N} T_{b-openarea}}{N} \quad (3.9)$$

$N$ is the number of observations for open area.

Vegetation's contribution for brightness temperature ($\Delta T_{b\text{-}vegetation}$) is estimated by comparison the standardized brightness temperature in open area with vegetation covered area:

$$\Delta T_{b\text{-}vegetation} = T_{b\text{-}standardized} - T_{b\text{-}ground} \quad (3.10)$$

### 3.3.4 AMSR-E brightness temperature correction procedure

Forest transmissivity calculated from Metsamaki's approach was estimated by comparing the reflectance of vegetation canopy with reflectance of underneath ground surface. Thus, this index has good ability to represent vegetation structure. In the present study, forest transmissivity was used for representing vegetation condition.

Vegetation's influence on AMSR-E brightness temperature is complex, thus physically based model is demanding when apply on the global scale. Comparing with physical approach, empirical approach is more feasible. By studying the statistic tendency, the relationship between $\Delta T_{b\text{-}vegetation}$ and transmissivity can be revealed.

Linear regression models between $\Delta T_{b\text{-}vegetation}$ and transmissivity have been setup. Those regression models were applied to correct AMSR-E brightness temperature.

## 3.4 Uncertainty assessment

The uncertainty assessment section includes two parts: Evaluation of uncertainty in the forest transmissivity estimate, and evaluation of the uncertainty in the $\Delta T_{b\text{-}vegetation}$ estimate.

### 3.4.1 Uncertainty assessment for forest transmissivity

3.4.1.1 Change detection

Because multiple reflectance data from different time were used when calculate forest transmissivity, the uncertainty introduces by land cover change need to discuss. Change detection was applied for estimating forest coverage variation.

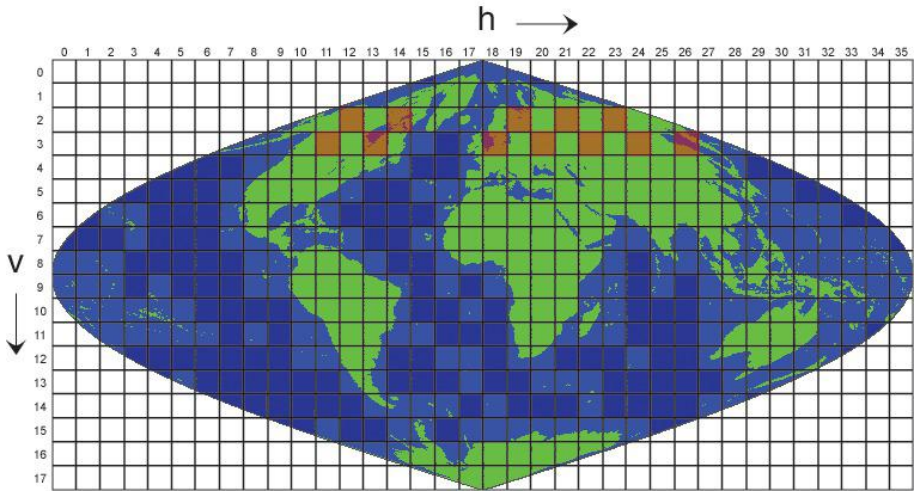


Fig.3.3 Selected tiles (Goddard Space Flight Center[modified], 2014)

The MODIS product MOD12Q1 land cover data set was used for change detection. The SCAmod method is applied in the area that latitudes greater than 45 degree north, thus, 12 tiles were selected in this area with systematic sampling. The 12 selected tiles (red tiles) marked in Fig.3.3 cover 34560000 $km^2$ and represent the area on which the transmissivity was estimated. The annual forest cover variation from 2002 to 2012 was used to evaluate if land cover change is one of the major sources of uncertainty in transmissivity estimation.

3.4.1.2 Statistical uncertainty estimation

The law of error propagation (Taylor, 1997) was applied to estimate the uncertainty of the transmissivity estimation with statistical approach:

$$S_t^2(\rho_{550,averge}(SCA=1)) = (\frac{\partial F_1}{\partial \rho_{550,averge}(SCA=1)})^2 S_{550,obs}^2(SCA=1) + (\frac{\partial F_1}{\partial \rho_{550,\ forest}})^2 S_{veg}^2 + (\frac{\partial F_1}{\partial \rho_{550,\ drysnow}})^2 S_{drysnow}^2 \quad (3.11)$$

Where $F_1$ is equation 3.2, $S_t^2(\rho_{550,averge}(SCA=1))$ is variance of $t_{550}^2$. $\rho_{550,averge}(SCA=1)$ is the average value of reflectance defined in equation 3.3, and $S_{550,obs}^2(SCA=1)$ is the variance for reflectance which has been defined in equation 3.4. The variance of vegetation and dry snow, $S_{veg}^2$ and $S_{drysnow}^2$, was given in Table 3.1.

Since all the variables in equation 3.11 are known, we can apply equation 3.11 to obtain equation 3.12. Equation 3.12 is the equation to estimate the variance of transmissivity.

$$S_t^2(\rho_{550,averge}(SCA=1)) = (\frac{1}{\rho_{550,\ drysnow} - \rho_{550,\ veg}})^2 S_{550,average}^2(SCA=1) + (\frac{\rho_{550,averge}(SCA=1) - \rho_{550,\ drysnow}}{(\rho_{550,\ drysnow} - \rho_{550,\ veg})^2})^2 S_{forest}^2 + (\frac{\rho_{550,averge}(SCA=1) - \rho_{550,\ veg}}{(\rho_{550,\ drysnow} - \rho_{550,\ veg})^2})^2 S_{drysnow}^2 \quad (3.12)$$

### 3.4.2 Uncertainty assessment for $\Delta T_{b\text{-}vegetation}$

The variance of $\Delta T_{b\text{-}vegetation}$ is contributed by $T_{b\text{-}standardized}$ and $T_{b\text{-}ground}$. Following the law of error propagation (Taylor, 1982), statistical uncertainty of $\Delta T_{b\text{-}vegetation}$ in each transect was estimated as:

$$S^2(\Delta T_{b-vegetation}) = (\frac{\partial F}{\partial T_{b-standardized}})^2 S^2(T_{b-standardized}) + (\frac{\partial F}{\partial T_{b-ground}})^2 S^2(T_{b-ground}) \quad (3.13)$$

Where $F_2$ is equation 3.10, $S^2(T_{b\text{-}standardized})$ and $S^2(T_{b\text{-}ground})$ are the variance of standardized brightness temperature and the brightness temperature of ground.

$S^2(T_{b\text{-}standardized})$ and $S^2(T_{b\text{-}ground})$ were calculated by equation 3.14 and 3.15:

$$S^2(T_{b-standardized}) = (\frac{\partial F}{\partial \Delta T_b})^2 S^2(\Delta T_b) = S^2(\Delta T_b) \quad (3.14)$$

$$S^2(T_{b\text{-}ground}) = \frac{\sum_{i=1}^{N} (T_{b\text{-}openarea} - T_{b\text{-}ground})^2}{N - 1} \quad (3.15)$$

Where $F_3$ represents equation 3.8, $S^2(\Delta T_b)$ is the variance of $\Delta T_b$ and $N$ is the number of observations for open area.

In equation 3.15, $T_{b\text{-}openarea}$ and $T_{b\text{-}ground}$ are both standardized brightness temperatures. The maximum variance introduced by this standardization procedure is 0.07 (more details in section 3.3.2.2), thus the maximum standard deviation in ($T_{b\text{-}openarea}$ - $T_{b\text{-}ground}$) contributed by the standardization procedure is less than 0.53K. Because this value is very small it was ignored in equation 3.15.

Using equation 3.7, $S^2(\Delta T_b)$ was calculated as follows:

$$S^2(\Delta T_b) = (T - T_{average} + 2)^2 S_e^2 \quad (3.16)$$

$S_e^2$ is the variance of emissivity product.

The difference of physical temperature inside each transect is less than 15k, and the accuracy of MYD11_L2 product is within 1k, therefore, ($T - T_{average}$) is less than 17k. Furthermore, according to the document of PM emissivity product, the standard deviation of emissivity product for each month is less than 0.015 (Norouzi, *et al.*, 2011).

Since $S^2(T_{b\text{-}standardized})$ and $S^2(T_{b\text{-}ground})$ were calculated out, then apply equation 3.13 to obtain equation 3.17 for estimate the accuracy of $\Delta T_{b\text{-}vegetation}$:

$$S^2(\Delta T_{b\text{-}vegetation}) = S^2(T_{b\text{-}standardized}) + S^2(T_{b\text{-}ground}) \quad (3.17)$$

The overall accuracy of $\Delta T_{b\text{-}vegetation}$ for all the transects was estimated as a weighted average, where $N$ is the total observations in all transects and $n$ is the number of observations inside transect $i$:

$$S^2_{overall}(\Delta T_{b-vegetation}) = \sum_{i=1}^{8} \frac{n}{N}(S_i^2(\Delta T_{b-vegetation})) \quad (3.18)$$

# Chapter 4: Results

This thesis is concerned with developing a correction procedure for passive microwave data using forest transmissivity estimated from MODIS observations. In this chapter the results from the three key elements of the analysis are presented. First, calculations of forest transmissivity are presented in Section 4.1 followed by the results of the approach to correct brightness temperatures from AMSR-E observations (Section 4.2). Finally, in section 4.3 an uncertainty analysis is presented that explores the errors in the brightness temperature corrections. The results follow on from the methodological descriptions described in Chapter 3. It should be noted that the $T_b$ correction procedure is applicable to AMSR2 and SSM/I passive microwave measurements.

## 4.1 Map of Forest transmissivity

### 4.1.1 Forest transmissivity estimation using the SCAmod method

Forest transmissivity estimates using the SCAmod method are shown in Fig.4.1. The data are represented in the figure as squared values for convenience of display, but the value not been squared was used in further calculations. The transmissivity data cover the region north of 45 °latitude where wintertime snow cover extent is sufficiently persistent during the MODIS era to facilitate the calculations.

At higher latitudes, vast areas of Canada, Russia, Europe and Alaska are covered by tundra and taiga landscapes whilst at at lower latitudes, the dominant land cover type is boreal forest. Because tree canopy has higher attenuation effect than tundra,

transmissivity in forest covered area is lower than tundra area. This pattern is clearly evident in Fig.4.1.

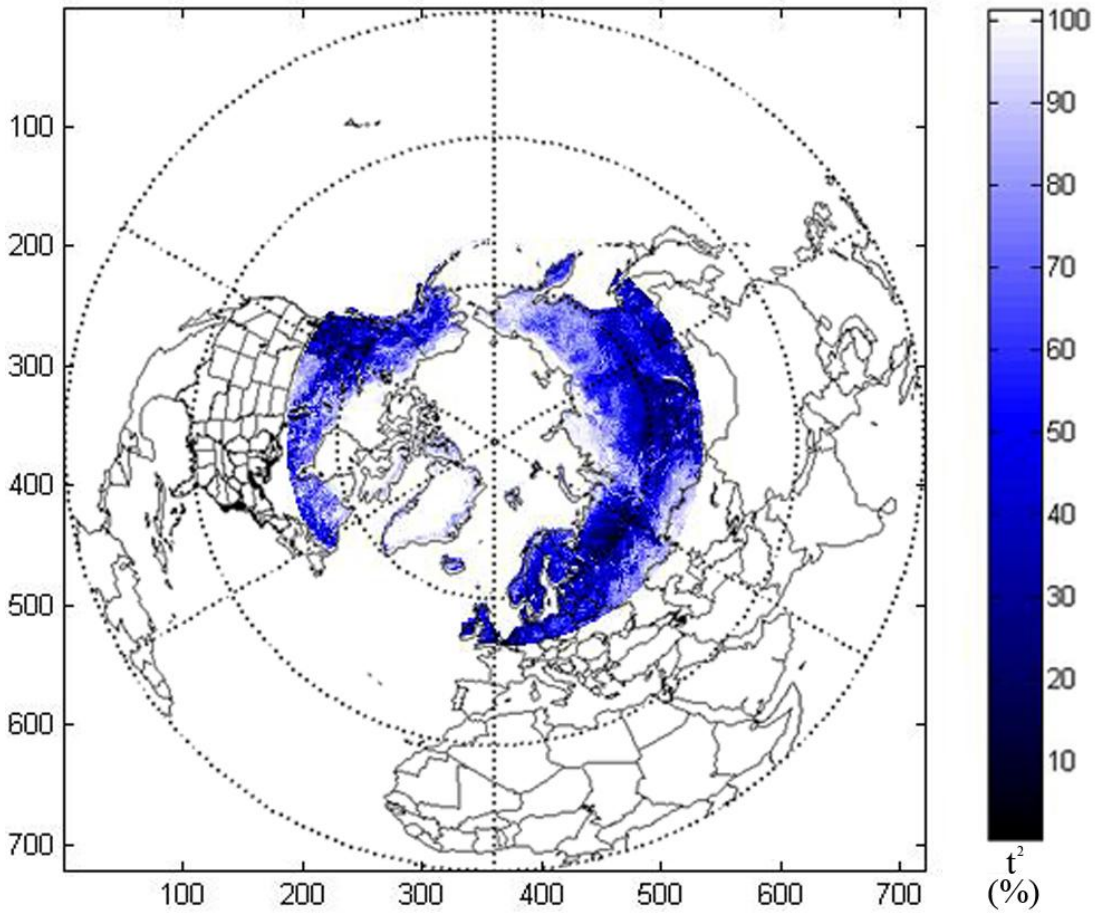


Fig.4.1 Map of squared transmissivity estimates projected to the EASE grid polar projection of the Northern Hemisphere. Missing data and oceans and significant water bodies are masked (white).

### 4.1.2 Expansion of the forest transmissivity data to lower latitude regions: the relationship between vegetation transmisssivity and forest fraction

Forest fraction data for 2006 and 2010 in the northern hemisphere were calculated from MODIS Vegetation Continuous Fields product (MOD44B) and are shown in

Fig.4.2. MODIS data were re-grided and re-projected to 25 km EASE grid to match the AMSR-E data. According to the forest fraction maps in 2006 and 2010, most forest covered areas were found in latitudinal regions below 60 ℃N. A comparison between forest fraction maps for 2006 and 2010 has been made (Fig.4.2), and *RMSE* between 2006 and 2010 is 3.98. This indicated that forest coverage revealed no fundamental change during this 4 year period at the scale of 25 km grid size.

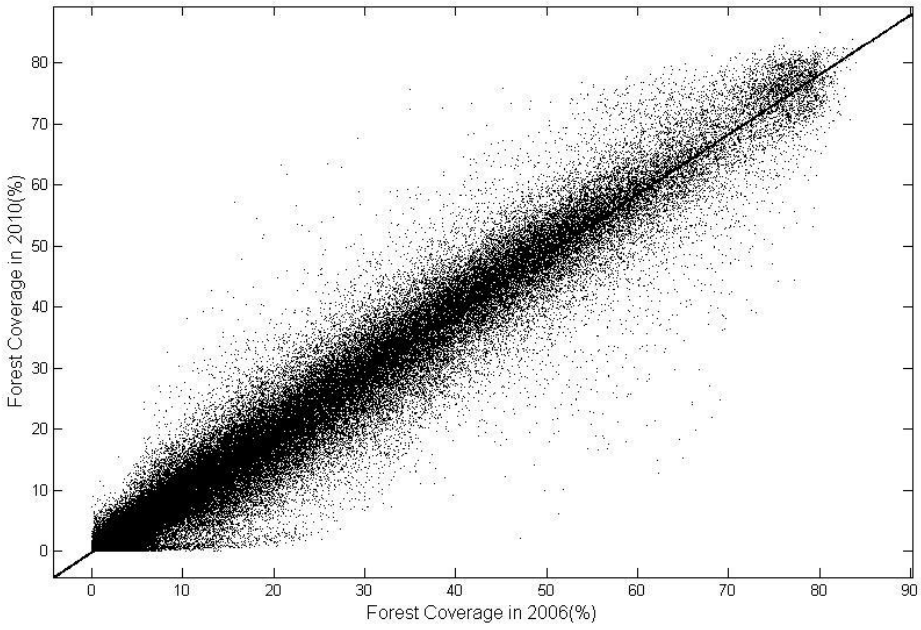


Fig.4.2 Forest coverage in 2006 VS. forest coverage in 2010

Because emissivity product is only available in 2006, thus, forest fraction data in 2006 were used to study the contribution to AMSR-E brightness temperatures.

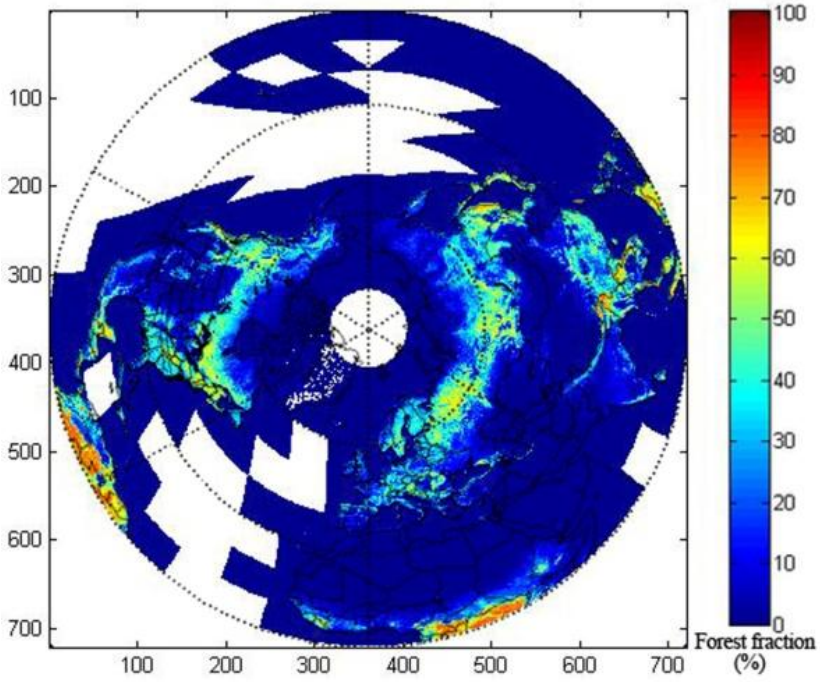


Forest fraction in 2006

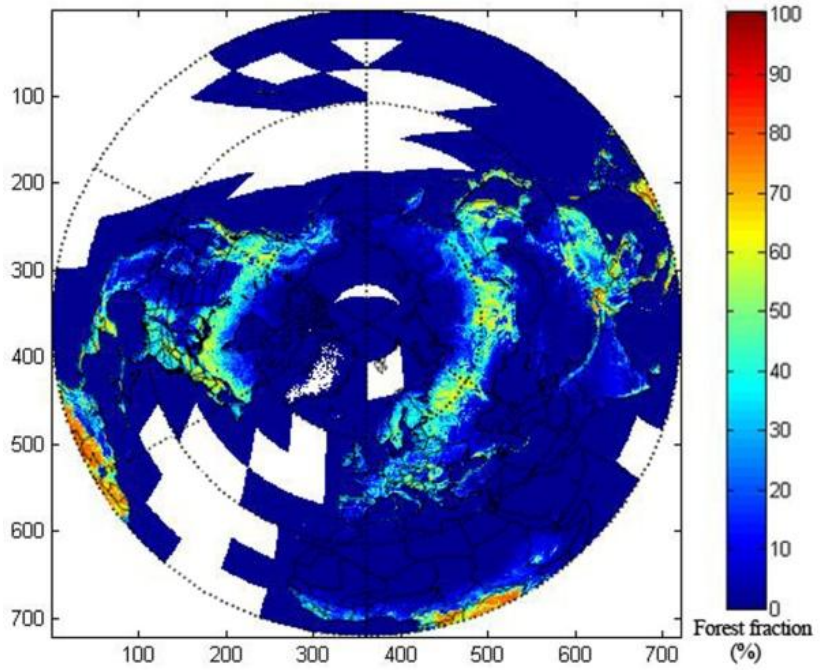


Forest fraction in 2010

Fig.4.3 Re-projected northern hemisphere forest fraction estimates from MOD44B for 2006 and 2010.

Fig.4.3 demonstrates the relationship between forest transmissivity calculated from SCAmod method and forest fraction data in 2010. Forest transmissivity is negatively related to forest fraction with higher forest fractions having lower transmissivity values and vice versa. The regression model between transmissivity (*t*) and forest fraction (*ff*) can be represent as below:

$$t = -0.88*ff + 93.75 \quad (4.1)$$

The coefficient of determination $R^2$ of this least squares regression model is 0.86; *RMSE* (or the standard error of the residuals) is 7.35. The maximum forest fraction observed is 85.91 % with a minimum of 0%.

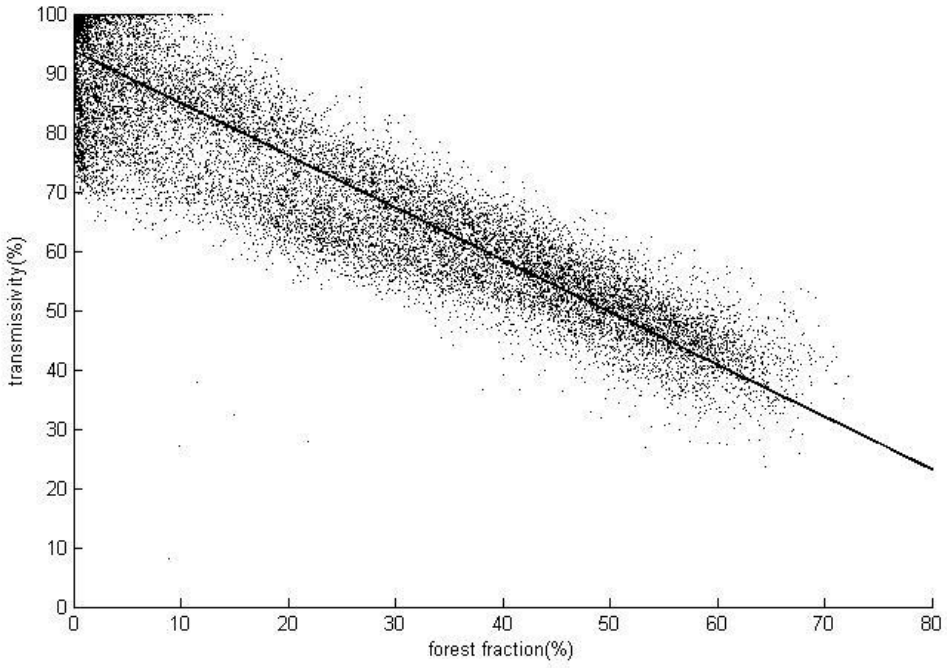


Fig.4.4 Relationship between forest fraction, MOD44B (Figure 4.3) and forest transmissivity from the SCAmod (Figure 4.1)

### 4.1.3 Forest transmissivity estimation by forest fraction

Fig.4.5 shows estimated transmissivity calculated from forest fraction data with the regression model from equation 4.1. Transmissivity values in low tree covered areas are higher than in high tree covered areas. There are two distinct forest covered areas in which transmissivity values are lower than average. First is the boreal forest region between 40 °- 60 °north. The transmissivity in this area is about 50 %. Another latitudinal region is the forest covered areas near the equator. In this low latitude region, transmssivity is typically 30 %.

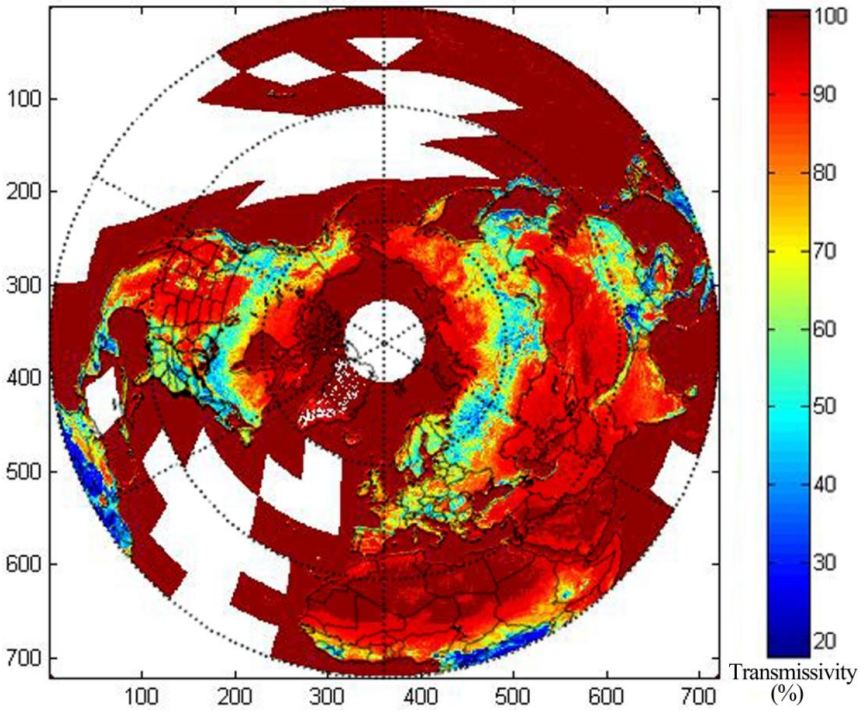


Transmissivity 2006

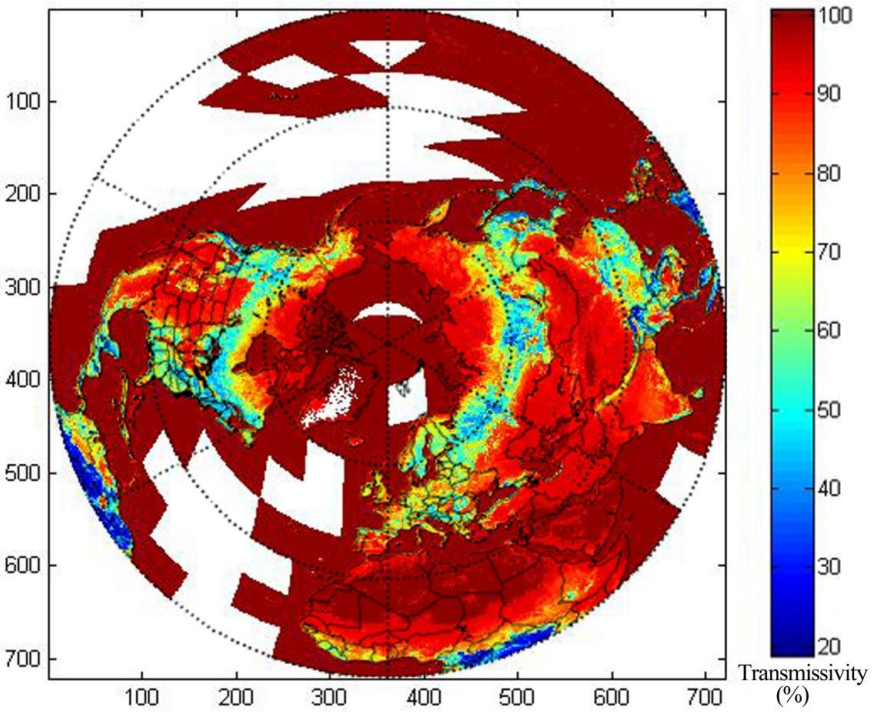


Transmissivity 2010

Fig.4.5 Estimated forest transmissivity calculated from MOD44B (Fig.4.3)

## 4.2 $\Delta T_{b\text{-}vegetation}$ estimation

Equation 3.10 was applied in $\Delta T_{b\text{-}vegetation}$ estimates. $\Delta T_{b\text{-}vegetation}$ is vegetation's contribution to scene brightness temperature and is needed to correct satellite-based brightness temperatures of snow.

Equation 3.10 calculates $\Delta T_{b\text{-}vegetation}$ inside each transect of a forest vegetated area. By studying the relationship between forest transmissivity and $\Delta T_{b\text{-}vegetation}$ inside each transect, brightness temperature corrections can be calculated according to forest transmissivity.

According to equation 3.10, to calculate $\Delta T_{b\text{-}vegetation}$ out, the brightness temperature within each transect must be standardized to $T_{b\text{-}standardized}$ at first with equation 3.7 and equation 3.8. After the brightness temperature has been standardized ($T_{b\text{-}standardized}$), $T_{b\text{-}ground}$ for each transect should be calculated according equation 3.9. Then, following equation 3.10, $T_{b\text{-}standardized}$ is compared for forest covered area is compared with $T_{b\text{-}ground}$, and a $\Delta T_{b\text{-}vegetation}$ estimated. The following sub-sections describe these steps culminating in maps of estimated forest vegetation correction maps ($\Delta T_{b\text{-}vegetation}$).

### 4.2.1 Standardized brightness temperature estimation within each forest transect

According to equations 3.7, 3.8 and 3.10 in Chapter 3, emissivity and physical land surface skin temperature data are needed to estimate the $\Delta T_{b\text{-}vegetation}$.

#### 4.2.1.1 Re-projected Emissivity data

The emissivity product for October 2010 and developed by Norouzi *et al.*(2011) is obtained for use from NSIDC. This month is chosen because in most mid- to high-latitude areas snow cover is not yet present and the emissivity (and skin temperature; see next subsection) can reveal the brightness temperature of the tree canopy alone without interference from snow. The original data set is gridded to a quarter-degree cell size and a global cylindrical, equidistant latitude-longitude projection with 1440 columns and 720 rows. Data were re-projected to 25 x 25 $km^2$ EASE grid polar projection.

According to re-projected emissivity map (Fig.4.6), in most areas emissivity is greater than 0.8. Compare forest covered area with non-forest covered area, the emissivity in the forest covered area is higher than open areas. Greenland has the lowest emissivity value in the northern hemisphere. In some areas of Greenland, the value of emissivity is lower than 0.7.

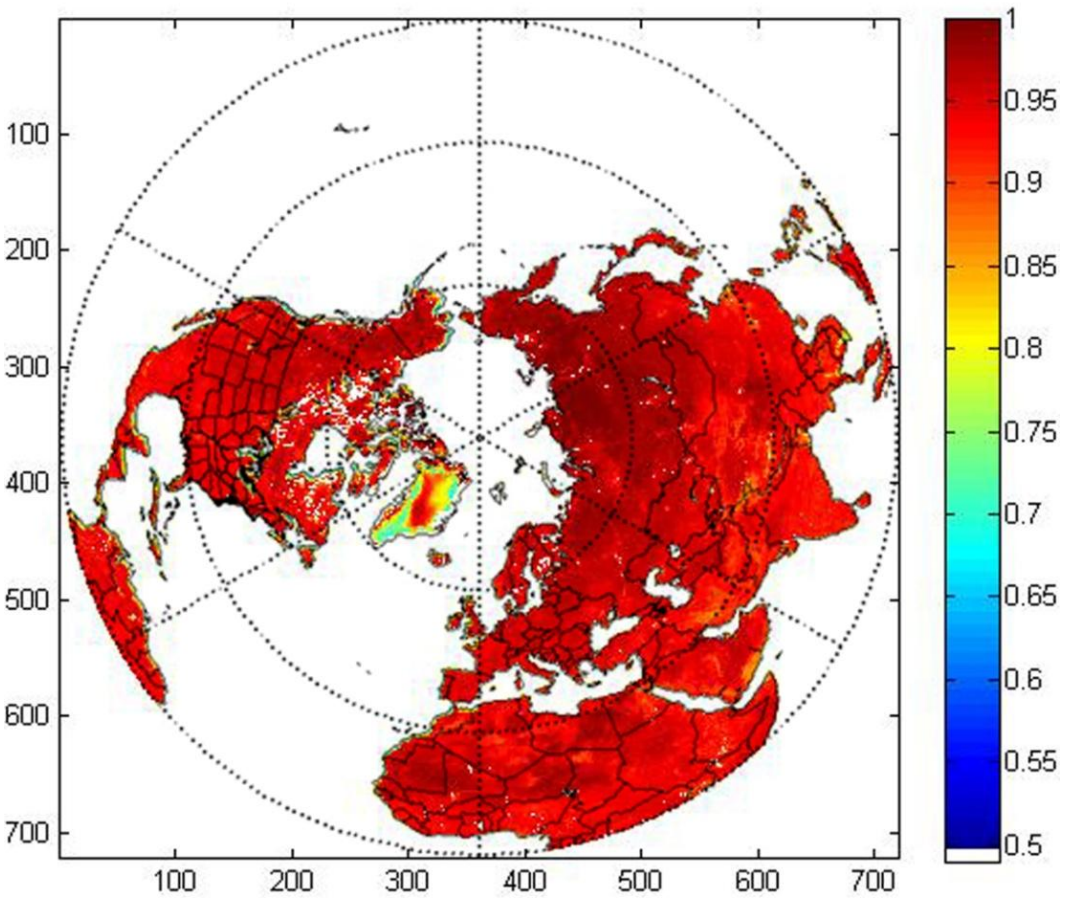


Emissivity at 18 GHz V-pol

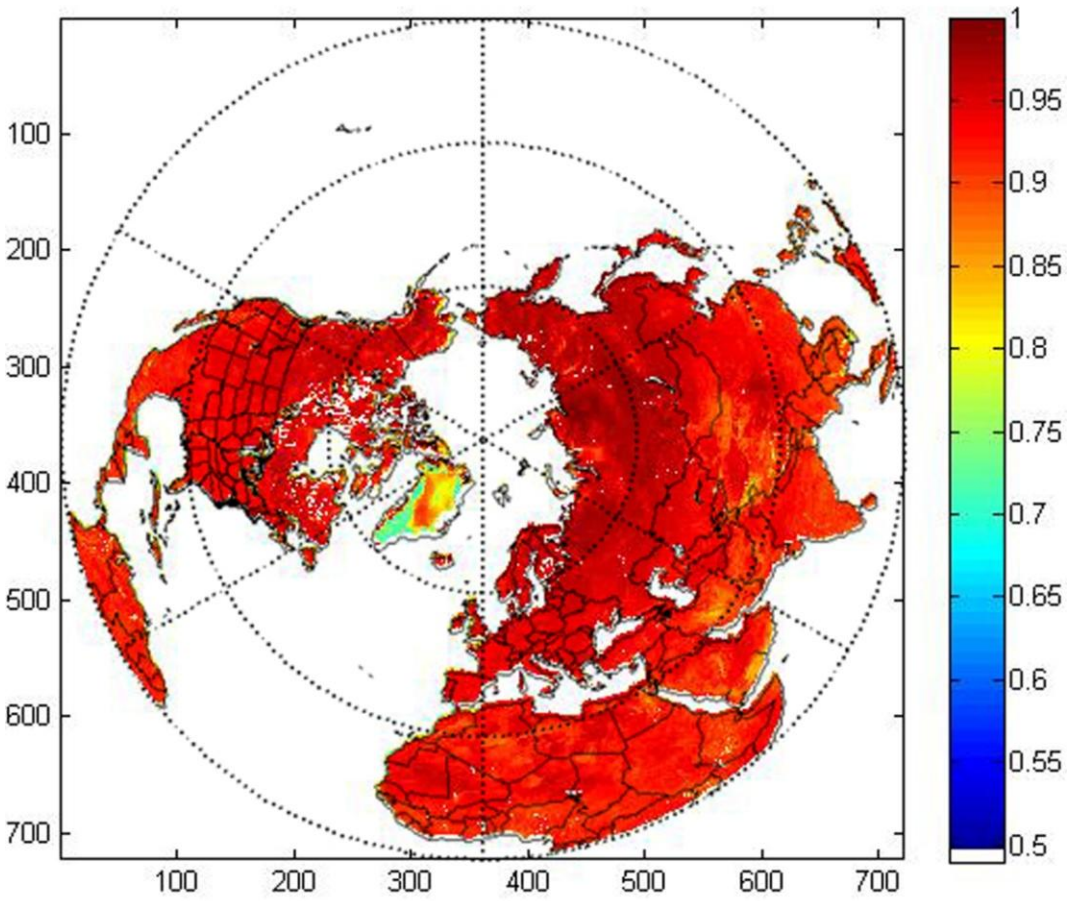


Emissivity at 36 GHz V-pol

Fig.4.6 Re-projected average emissivity estimates of the northern hemisphere for October 2010 from Norouzi *et al*., (2011)

#### 4.2.1.2 MODIS land surface temperature product

Fig.4.7 shows re-projected MODIS land surface temperature product (MYD11L2) data at 11 October 2010. The swathes of MODIS temperature data for northern hemisphere tiles were re-gridded and re-projected to 25 x 25 $km^2$ EASE grid. According to this figure, in general, temperatures in higher latitude regions are lower

than in lower latitude places. The coldest location is in the north part of Greenland, and the hottest place is near the equator. The temperature difference between coldest place and warmest place is about 50 K.

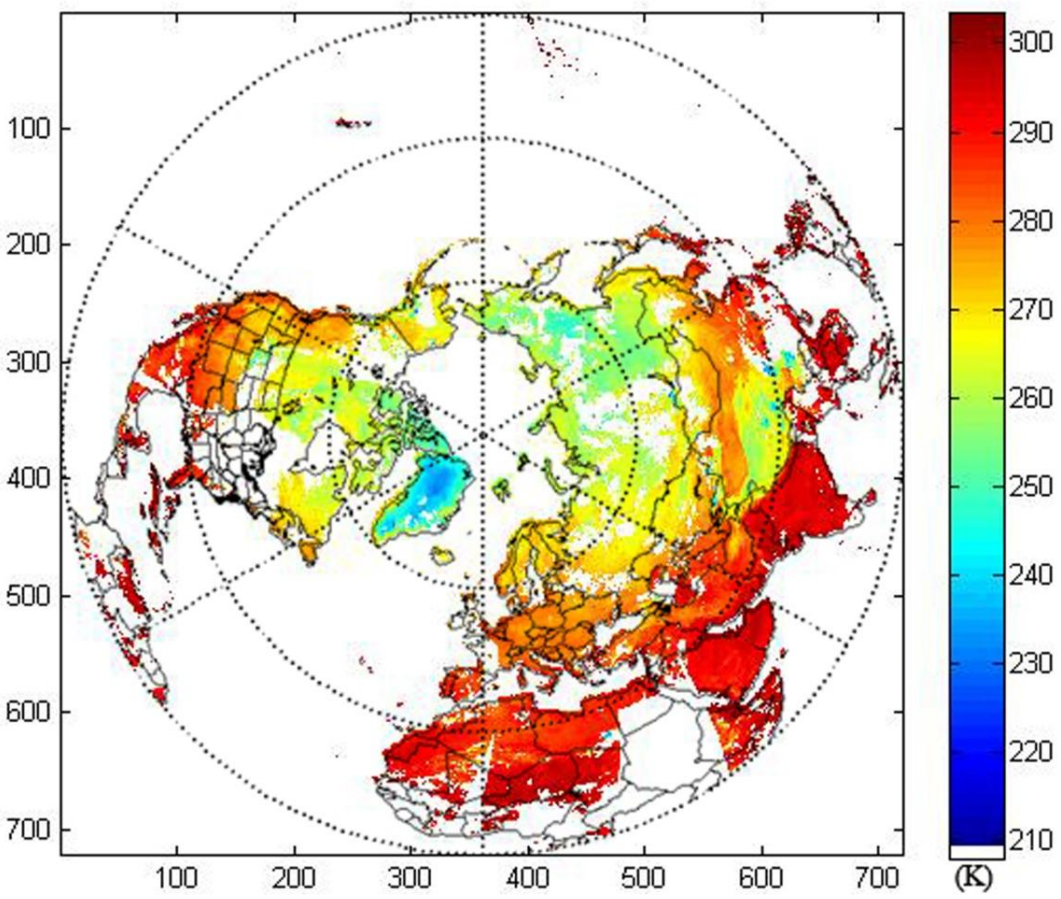


Fig.4.7 EASE-grid re-projected MODIS land surface temperature data for 11 October, 2010. Areas of persistent cloud cover are missing (white) and oceans and significant water bodies are masked.

Since emissivity data and land surface temperatures were provided, the brightness temperature at each transect (see Fig.3.1) can be standardized to $T_{b\text{-}standardized}$ value using equations 3.7 and equation 3.8.

### 4.2.2 Estimated $T_{b\text{-}ground}$ within each transect

After AMSR-E brightness temperature was converted to $T_{b\text{-}standardized}$, $T_{b\text{-}ground}$ can be calculated according to equation 3.9. $T_{b\text{-}ground}$ is the mean value of $T_{b\text{-}standardized}$ to the adjacent open area (transmissivity higher than 0.85) for each transect. Table 4.1 and Table 4.2 represent the calculated $T_{b\text{-}ground}$ at different transects for $T_b$ at vertical polarization (V-pol) and horizontal polarizations (H-pol) respectively and Figs. 3.8 and 3.9 show the data in graphical form. The details of transects can be found in Table 2.3.

| Transect ID | V6 | V10 | V18 | V23 | V36 | V89 |
|---|---|---|---|---|---|---|
| 1 | 255.52 | 254.54 | 253.12 | 253.08 | 249.93 | 236.08 |
| 2 | 251.32 | 250.80 | 250.22 | 250.37 | 247.29 | 223.46 |
| 3 | 254.75 | 254.17 | 251.87 | 251.53 | 246.05 | 225.85 |
| 4 | 251.06 | 252.88 | 254.81 | 257.41 | 256.39 | 258.75 |
| 5 | 246.78 | 247.09 | 248.51 | 250.23 | 249.88 | 243.18 |
| 6 | 239.66 | 239.79 | 241.93 | 244.17 | 244.26 | 243.44 |
| 7 | 250.81 | 252.18 | 253.73 | 254.64 | 253.55 | 249.17 |
| 8 | 261.66 | 263.14 | 263.30 | 263.74 | 260.51 | 253.42 |

Table 4.1 Estimated AMSR-E $T_{b\text{-}ground}$ at V-pol

| Transect ID | V6 | V10 | V18 | V23 | V36 | V89 |
|---|---|---|---|---|---|---|
| 1 | 255.52 | 254.55 | 253.12 | 253.08 | 249.93 | 236.08 |
| 2 | 251.32 | 250.80 | 250.22 | 250.37 | 247.29 | 223.46 |
| 3 | 254.75 | 254.17 | 251.87 | 251.53 | 246.05 | 225.85 |
| 4 | 251.06 | 252.88 | 254.81 | 257.41 | 256.39 | 258.75 |
| 5 | 246.79 | 247.09 | 248.51 | 250.23 | 249.88 | 243.18 |
| 6 | 239.66 | 239.79 | 241.93 | 244.17 | 244.26 | 243.44 |
| 7 | 250.81 | 252.18 | 253.73 | 254.64 | 253.55 | 249.17 |
| 8 | 261.66 | 263.14 | 263.30 | 263.74 | 260.51 | 253.42 |

Table 4.2 Estimated AMSR-E $T_{b\text{-}ground}$ at H-pol

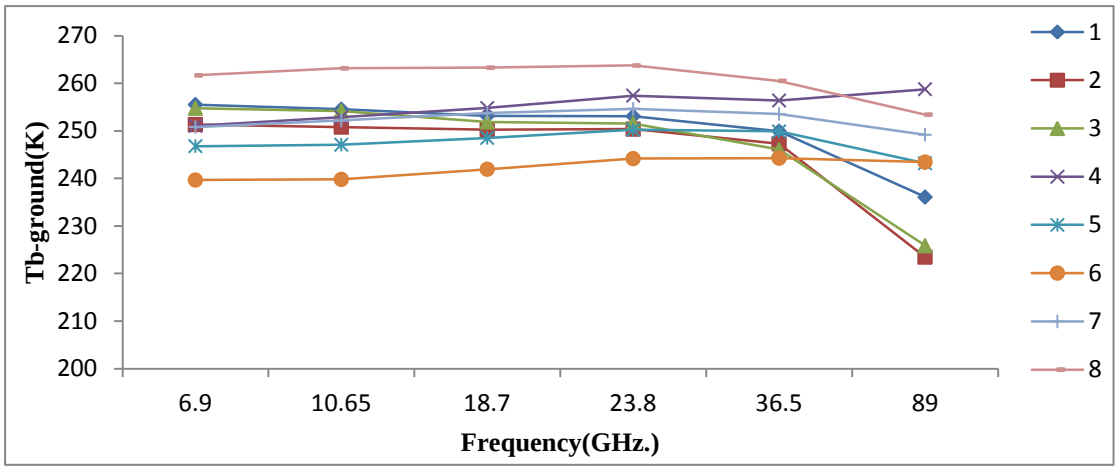


Fig.4.8 $T_{b\text{-}ground}$ at V-pol

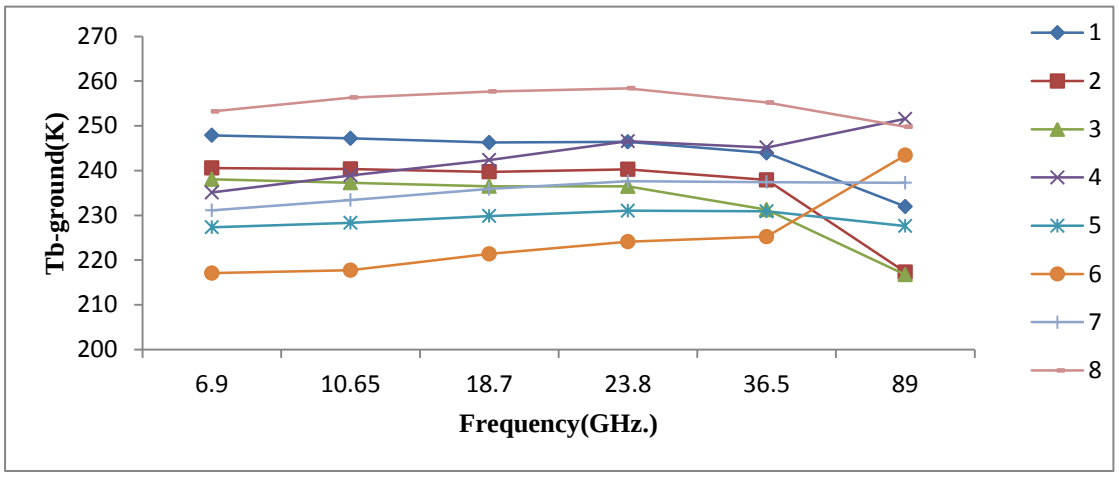


Fig.4.9 $T_{b\text{-}ground}$ at H-pol

Figs 4.8 and 4.9 compares $T_{b\text{-}ground}$ in different transects over the range of AMSR-E frequencies. The maximum difference in $T_{b\text{-}ground}$ between different transects is about 30 K with differences in the H-polarized bands greater than those for V-pol bands. The data suggest that there is a larger difference at H-pol than V-pol because layered

structures in the canopy act as stronger emitters at H-pol than at V-pol. It is also interesting to note that for most transects the variation of $T_{b\text{-}ground}$ value is small between 6.9 GHz and 36.5 GHz However, $T_{b\text{-}ground}$ values are relatively lower at 89 GHz bands except transect 4 and transect 6 where they increase relative to the lower frequency responses.

### 4.2.3 Modelling the Relationship between $\Delta T_{b\text{-}vegetation}$ and forest transmissivity

Since the brightness temperature within all the transects have been standardized to account for the effect temperature difference within each transect ($T_{b\text{-}standardized}$), and $T_{b\text{-}ground}$ values for each transect have been calculated to represent brightness temperatures of the ground only, $\Delta T_{b\text{-}vegetation}$ of the canopy at each transect can be estimated according to equation 3.10. To better understand the brightness temperature contributed by vegetation, the relationship between $\Delta T_{b\text{-}vegetation}$ and forest transmissivity is explored in the section below. This analysis enables the creation of a correction expression to represent forest canopy emission processes for each frequency and polarization using the transmissivity data.

#### 4.2.3.1 Relationship between $\Delta T_{b\text{-}vegetation}$ and forest transmissivity for all paired observations

A regression analysis was conducted to explore the relationship between $\Delta T_{b\text{-}vegetation}$ transmisivity for the entire transmissivity range and all paired brightness temperature measurements at each frequency and polarization. To assess whether a parametric or

non-parametric approach was appropriate, normality of these two variables was calculated using the skewness and kurtosis metrics.

Kurtosis is a descriptor of shape of a histogram; when data probability distribution is normal, the value of kurtosis is 3. If the distributions are more outlier-prone than the normal distribution, the value of kurtosis is larger than 3, if the distributions are flatter, the value of kurtosis is less than 3.

Skewness is another descriptor to measure the shape of the data probability distribution. This value represents the asymmetry of the probability distribution. When the data are spread out more to the left, skewness is negative. When the data are spread out more to the right, skewness is positive. If the data are normal distribution, skewness is zero.

| | Transmissivity | 6 GHz | | 10GHz | |
|---|---|---|---|---|---|
| | | V-pol | H-pol | V-pol | H-pol |
| Skewness | 0.0017 | -1.24 | -0.48 | -1.43 | -0.49 |
| Kurtosis | 1.8973 | 7.11 | 3.70 | 8.58 | 3.77 |

n = 2846

Table 4.3(a) Skewness and kurtosis for $\Delta T_{b\text{-}vegetation}$ and transmissivity

| | 18GHz | | 23 GHz | | 36 GHz | | 89GHz | |
|---|---|---|---|---|---|---|---|---|
| | V-pol | H-pol | V-pol | H-pol | V-pol | H-pol | V-pol | H-pol |
| Skewness | -1.38 | -0.47 | -1.10 | -0.46 | -0.60 | -0.40 | -0.19 | -0.19 |
| Kurtosis | 9.46 | 3.76 | 7.74 | 3.95 | 5.13 | 3.70 | 4.20 | 3.40 |

n = 2846

Table 4.3(b) Skewness and kurtosis for $\Delta T_{b\text{-}vegetation}$ and transmissivity

n is the total number of pixels in selected transects. According to Table 3.3, the distribution of H-pol is very close to normal distribution. For V-pol, the distribution has the tendency to spread to left.

Fig.4.10 and Fig.4.11 demonstrate the relationship between transmissivity and the brightness temperature contributed by vegetation ($\Delta T_{b\text{-}vegetation}$) at different frequencies and polarization states. According to these figures, transmissivity value is negatively correlated to $\Delta T_{b\text{-}vegetation}$ indicating that higher density vegetation (lower transmissivity) tends to contribute more brightness temperature emission to the AMSR-E's observations.

Bands at different frequencies and polarization are not equally influenced by vegetation with, higher frequency band $T_b$s more sensitive to vegetation influences than lower frequency responses. For different polarization, the H-pol response is more sensitive to vegetation than at V-pol. This result is significant because it indicates that at the typical snow scattering channels (36 and 89 GHz) .a more aggressive correction is required.

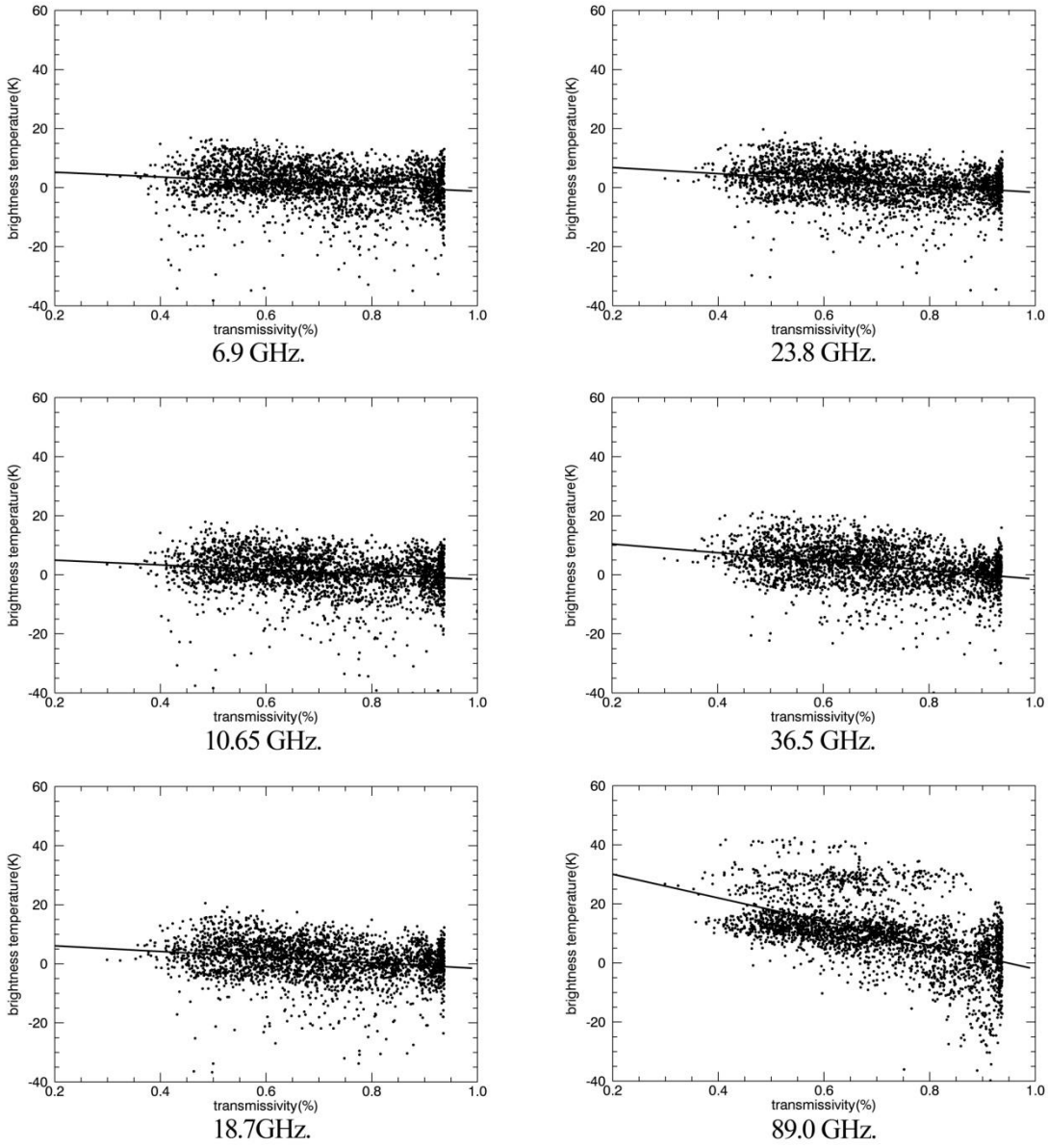


Fig.4.10 Relationship between $\Delta T_{b\text{-}vegetation}$ and forest transmissivity at V-pol bands

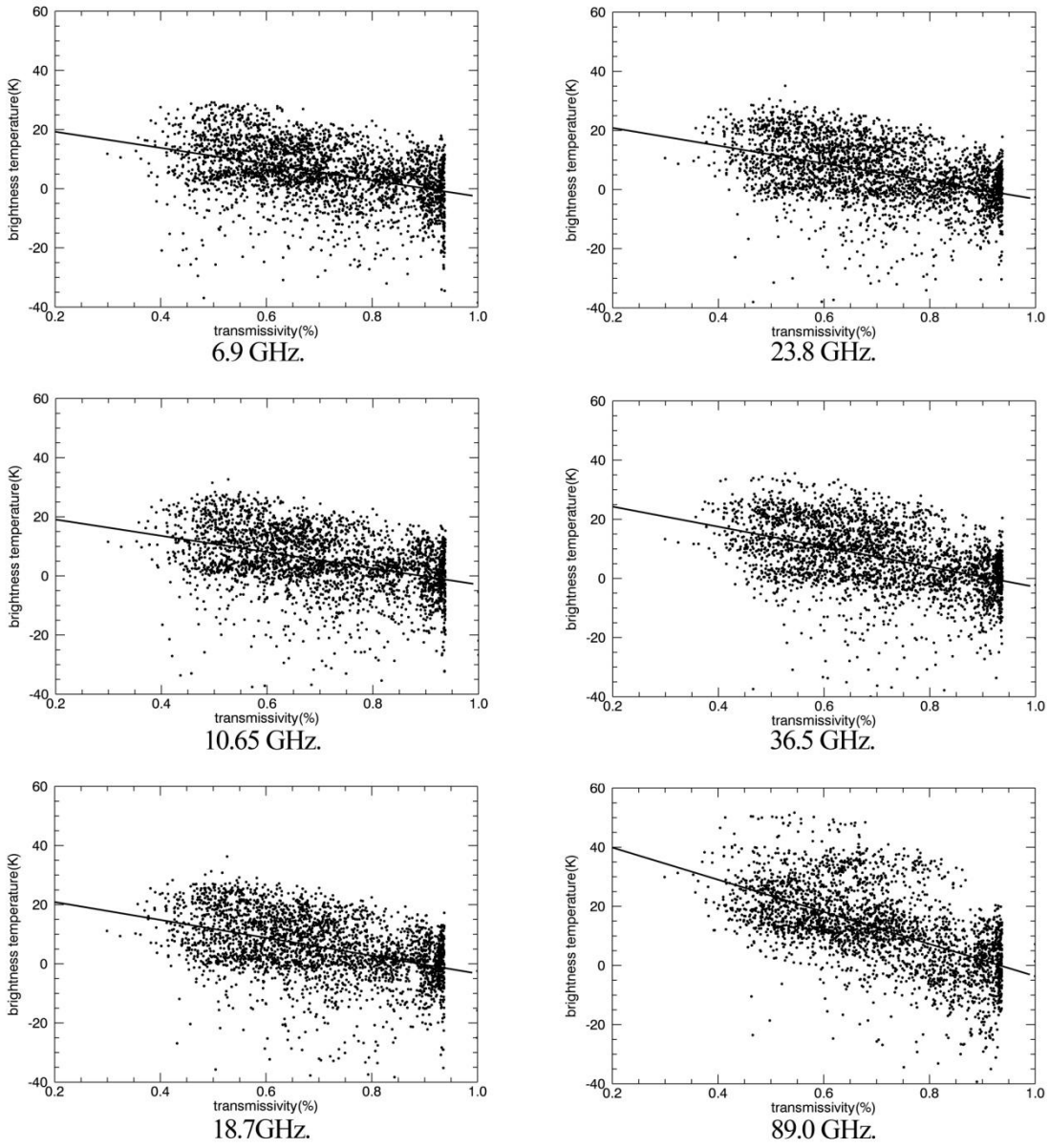


Fig.4.11 Relationship between $\Delta T_{b\text{-}vegetation}$ and forest transmissivity at H-pol bands

The coefficients of the regression equations are shown in Table 4.4 and the regression performance statistics ($R^2$, sums of squares of errors [*SSE*] and error of the prediction [*RMSE*]) are shown in Table 4.4. According to this table, the slope increases with increasing frequency and the slope in H-pol is higher than in V-pol as indicated in Figs.4.10 and 4.11.

| Band(GHz) | V-pol | H-pol |
|---|---|---|
| **6.9** | *y = -8.06x + 6.83* | *y = -27.39x + 24.76* |
| **10.65** | *y = -8.08x + 6.58* | *y = -27.52x + 24.57* |
| **18.7** | *y = -9.57x + 8.00* | *y = -30.26x + 26.95* |
| **23.8** | *y = -10.54x + 8.94* | *y = -30.07x + 26.86* |
| **36.5** | *y = -14.85x + 13.42* | *y = -33.97x + 31.07* |
| **89.0** | *y = -40.17x + 38.07* | *y = -54.38x + 50.77* |

Table 4.4 Regression models for $\Delta T_{b\text{-}vegetation}$ and forest transmissivity

In Table 4.5 the *SSE* represents the total deviation of the response values from the fit to the response values. (It is also called the summed square of residuals.) A lower *SSE* means that the explanatory value has better ability to explain the response value. The $R^2$, or coefficient of determination, is the square of the correlation between the response values and the predicted response values. $R^2$ represents the goodness of fit about regression models in Table 4.3; an $R^2$ closer to 1.0 means the goodness of fit is better.

The *RMSE* is also known as the fit standard error or the standard error of the regression. It is an estimate of the standard deviation of the random component in the data. *RMSE* represents the sample standard deviation of the differences between predicted values and observed values. This index is a frequently used measure of the differences between values predicted by a model or an estimator and the values actually observed.

According to Table 4.5, the *SSE*s for all the bands are greater than 100000. The $R^2$ of the H-pol bands are greater than the V-pol $R^2$ values. The *RMSE* of horizontal bands are

higher than equivalent vertical bands. It is important to note that the $R^2$ values are still relatively small and so it was necessary to calculate the *P* values for the relationships.

| **Polarization** | **Frequency (GHz)** | ***SSE*** | $R^2$ | ***RMSE*** |
|---|---|---|---|---|
| **V-Pol** | 6.9 | 1.280e+05 | 0.03 | 6.68 |
| | 10.65 | 1.289e+05 | 0.03 | 6.70 |
| | 18.7 | 1.273e+05 | 0.04 | 6.66 |
| | 23.8 | 1.042e+05 | 0.06 | 6.02 |
| | 36.5 | 1.185e+05 | 0.11 | 6.42 |
| | 89.0 | 2.623e+05 | 0.28 | 9.57 |
| **H-pol** | 6.9 | 2.425e+05 | 0.17 | 9.24 |
| | 10.65 | 2.526e+05 | 0.16 | 9.43 |
| | 18.7 | 2.641e+05 | 0.18 | 9.64 |
| | 23.8 | 2.481e+05 | 0.19 | 9.32 |
| | 36.5 | 2.876e+05 | 0.21 | 10.04 |
| | 89.0 | 3.674e+05 | 0.34 | 11.37 |
| **Average** | | 2.109e+05 | 0.16 | 8.42 |

Table 4.5 Goodness of fit for regression models for transmissivity and $\Delta T_{b\text{-}vegetation}$ for all data

The *P* value is considered as the estimated probability of rejecting the null hypothesis of a study. In a regression analysis, the null hypothesis is accepted if the coefficient of explanatory value and response value is equal to zero (no effect). Low *P* values (less than the critical *P* value) indicate that the null hypothesis should be rejected and that the explanatory value and response value is related, or there is a relationship between the variables.

In this study, the *p* value was used to evaluate if $\Delta T_{b\text{-}vegetation}$ and transmissivity are related. A *P* value less than 0.05 means $\Delta T_{b\text{-}vegetation}$ and transmissivity are very likely related. According to Table 4.6, *P* value for all the bands are less than 0.05.

| | | | | | | | |
|---|---|---|---|---|---|---|---|
| **Vertical** | **Frequency (GHz)** | **6.9** | **10.65** | **18.7** | **23.8** | **36.5** | **89** |
| | *P* value | 5.05E-22 | 5.42E-22 | 2.15E-30 | 8.20E-44 | 2.20E-73 | 8.32E-211 |
| **Horizon** | **Frequency (GHz)** | **6.9** | **10.65** | **18.7** | **23.8** | **36.5** | **89** |
| | *P* value | 8.51E-114 | 5.67E-111 | 2.20E-126 | 4.19E-133 | 7.87E-145 | 5.25E-258 |

Table 4.6 *P* values between transmissivity and $\Delta T_{b\text{-}vegetation}$

### 4.2.3.2 Relationship between $\Delta T_{b\text{-}vegetation}$ and forest transmissivity for transmissivity-aggregated data

In the previous section, the regression fits ($R^2$) were shown to be relatively low even though there were strong degrees of associations between the dependent variables ($\Delta T_{b\text{-}vegetation}$) and the independent variable (transmissivity) indicated by *P* value. In order to explore whether the relationship could be better generalized, $\Delta T_{b\text{-}vegetation}$ data for each frequency and polarization state were averaged within defined forest transmissivity intervals. Fig.4.11 and Fig.4.12 are the box plots of transmissivity and $\Delta T_{b\text{-}vegetation}$ for all AMSR-E frequencies and polarizations. Transmissivity values were divided into seven equally-spaced intervals (from 0.3 to 1), the step length of each interval being 0.1 with the defining midpoint half-way along each interval (i.e. 0.35,

0.45, 0.55, 0.65, 0.75, 0.85 and 0.95). Within each transmissivity interval, the statistics of the $\Delta T_{b\text{-}vegetation}$ was calculated and this is what is shown.

It was important to define what part of the statistical distribution (mean, median, mode) in $\Delta T_{b\text{-}vegetation}$ should be used as the dependent variable, given that the transmissivity data were to be represented by the midpoint of each interval. In addition, it was necessary to determine whether or not the data were skewed in each transmissivity interval. Tables 4.7 and 4.8 shows the kurtosis and skewness value for the distributions of the value of the $\Delta T_{b\text{-}vegetation}$ contributed by vegetation for each transmissivity interval. According to Table 4.7, kurtosis value for most intervals are around 2 to 6. Few intervals are greater than 10 or less than 2.

| Transmissivity interval | Frenquency (GHz) | Transmissivity intervals | | | | | | | |
|---|---|---|---|---|---|---|---|---|---|
| | | 0.3 to 0.4 | 0.4 to 0.5 | 0.5 to 0.6 | 0.6 to 0.7 | 0.7 to 0.8 | 0.8 to 0.9 | 0.9 to 1 | Average |
| vertical | 6.9 | 3.73 | 8.92 | 8.36 | 4.85 | 4.75 | 6.40 | 3.85 | 5.84 |
| | 10.65 | 4.64 | 12.12 | 11.32 | 5.04 | 5.73 | 8.97 | 6.46 | 7.76 |
| | 18.7 | 3.28 | 12.10 | 13.68 | 4.91 | 5.41 | 9.59 | 18.69 | 9.67 |
| | 23.8 | 3.06 | 9.43 | 9.06 | 4.21 | 4.61 | 11.65 | 17.63 | 8.52 |
| | 36.5 | 1.75 | 6.09 | 7.54 | 4.14 | 3.66 | 7.91 | 6.42 | 5.36 |
| | 89.0 | 1.40 | 3.95 | 4.54 | 2.86 | 6.29 | 4.22 | 3.75 | 3.86 |
| horizontal | 6.9 | 2.44 | 4.99 | 3.62 | 4.35 | 3.22 | 4.30 | 3.77 | 3.81 |
| | 10.65 | 2.13 | 5.25 | 4.54 | 4.71 | 3.55 | 4.48 | 3.55 | 4.03 |
| | 18.7 | 1.83 | 3.54 | 3.50 | 4.49 | 4.32 | 4.82 | 4.28 | 3.82 |
| | 23.8 | 1.70 | 8.70 | 4.14 | 4.51 | 3.97 | 5.84 | 3.82 | 4.67 |
| | 36.5 | 1.55 | 9.68 | 4.47 | 4.66 | 4.02 | 4.27 | 3.95 | 4.66 |
| | 89.0 | 1.93 | 6.00 | 3.66 | 3.15 | 4.63 | 4.06 | 3.63 | 3.90 |

Table 4.7 Kurtosis for $\Delta T_{b\text{-}vegetation}$ distribution inside each transmissivity interval

Table 4.8 shows the skewness values for the distributions of the $\Delta T_{b\text{-}vegetation}$ contributed by vegetation for each transmissivity interval. According to this table, skewness values for most intervals are between -1 to 1. Few intervals were greater than 1 or less than -2.

| Transmissivity interval | Frenquency (GHz) | Transmissivity intervals | | | | | | | |
|---|---|---|---|---|---|---|---|---|---|
| | | 0.3 to 0.4 | 0.4 to 0.5 | 0.5 to 0.6 | 0.6 to 0.7 | 0.7 to 0.8 | 0.8 to 0.9 | 0.9 to 1 | Average |
| vertical | 6.9 | -0.03 | -1.99 | -1.19 | -0.72 | -0.92 | -1.28 | -0.68 | -0.97 |
| | 10.65 | 0.94 | -2.33 | -1.49 | -0.88 | -1.09 | -1.74 | -1.09 | -1.10 |
| | 18.7 | 0.57 | -1.94 | -1.48 | -0.96 | -1.01 | -1.72 | -2.55 | -1.30 |
| | 23.8 | 0.58 | -1.46 | -0.99 | -0.80 | -0.85 | -1.90 | -2.33 | -1.11 |
| | 36.5 | 0.37 | -0.75 | -0.68 | -0.68 | -0.57 | -1.22 | -1.15 | -0.67 |
| | 89.0 | 0.33 | 1.12 | 1.12 | 0.65 | -0.08 | 0.22 | -0.85 | 0.36 |
| horizontal | 6.9 | -0.08 | -1.07 | -0.37 | -0.71 | -0.53 | -0.84 | -0.66 | -0.61 |
| | 10.65 | 0.11 | -1.03 | -0.61 | -0.88 | -0.61 | -0.84 | -0.64 | -0.64 |
| | 18.7 | -0.11 | -0.48 | -0.47 | -0.88 | -0.86 | -0.84 | -0.81 | -0.64 |
| | 23.8 | -0.20 | -1.43 | -0.58 | -0.83 | -0.71 | -1.00 | -0.63 | -0.77 |
| | 36.5 | -0.23 | -1.45 | -0.69 | -0.82 | -0.67 | -0.40 | -0.70 | -0.71 |
| | 89.0 | -0.11 | -0.21 | 0.56 | 0.15 | -0.35 | 0.11 | -0.72 | 0.03 |

Table 4.8 Skewness for $\Delta T_{b\text{-}vegetation}$ distribution inside each transmissivity interval

Results from the skewness tests indicate that the majority of the boxplot data do not have substantial skewness; a skewness of greater than 1 or less than -1 indicates a distribution that is not symmetrical. As a result, the a regression was conducted on the paired mean $\Delta T_{b\text{-}vegetation}$ and interval value. The box plots in Figures 4.12 and 4.13

show the lower 25% and upper 75% interquartile values, the minimum and maximum values and the line within the box shows the median value of $\Delta T_{b\text{-}vegetation}$ for each transmissivity interval. Small circles are the mean values of $\Delta T_{b\text{-}vegetation}$ in each interval. The regression lines represent linear regression models of the mean value of $\Delta T_{b\text{-}vegetation}$ and transmissivity for each interval.

According to the two plots, the $\Delta T_{b\text{-}vegetation}$ increases as transmissivity decreases, which means the brightness temperature contributed by the vegetation increases as forest vegetation becomes higher density. The regression line slope coefficients in H-pol bands are higher than the V-pol data.

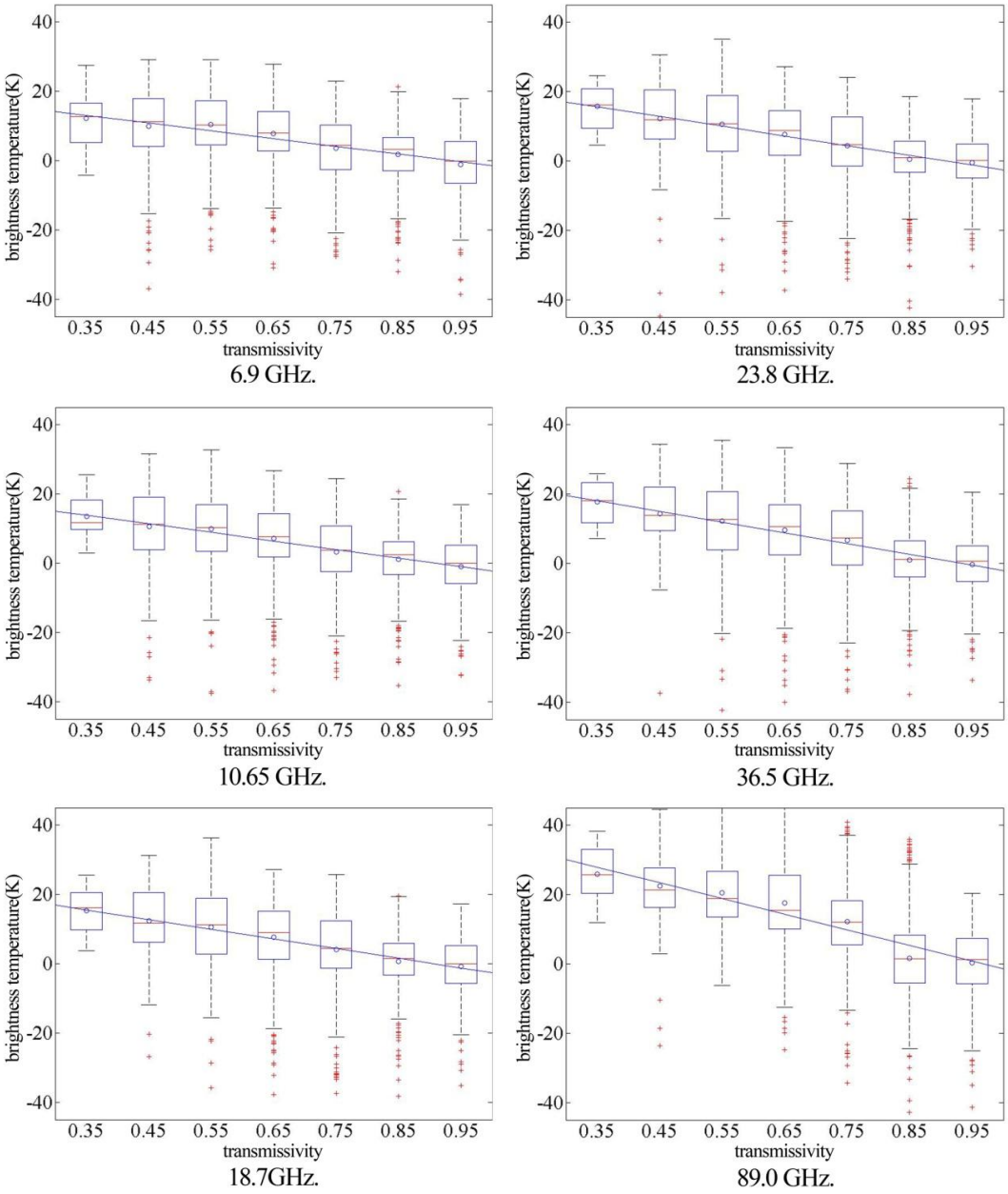


Fig.4.12 $\Delta T_{b\text{-}vegetation}$ distribution within each transmissivity interval and regression line at horizontal polarization bands

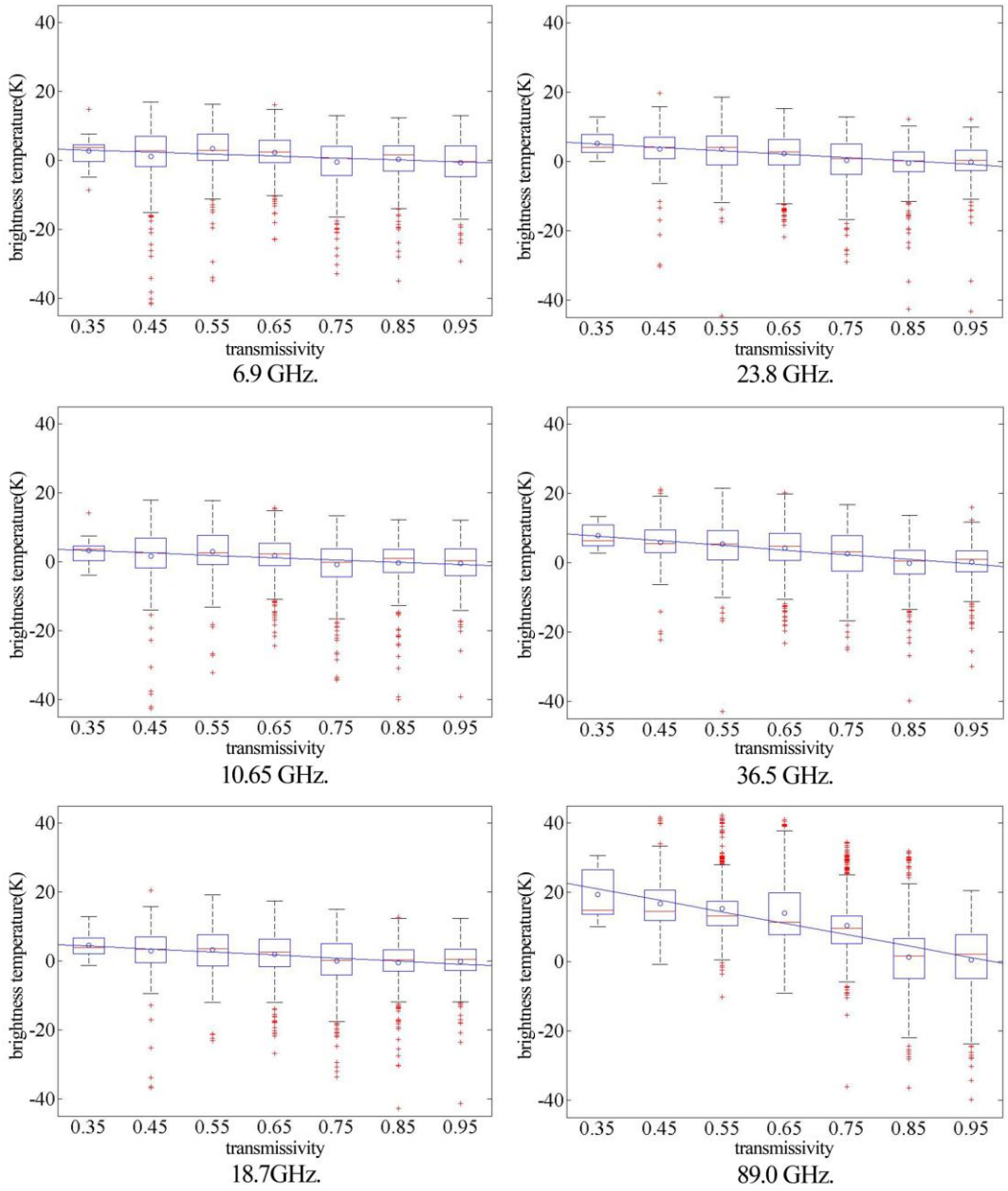


Fig.4.13 $\Delta T_{b\text{-}vegetation}$ distribution inside each transmissivity interval and tendency line at vertical polarization bands

Table 4.9 shows the regression model coefficients from Figures 4.12 and 4.13. According to this table, the slope increases with frequency. The slope in H-pol is greater than the slope in V-pol. In comparing regression models in Table 4.3 with

regression models in Table 4.9, transmissivity and $\Delta T_{b\text{-}vegetation}$ represent similar relationship, but the slopes of regression models in Table 4.9 are lower compared with their equivalent bands in Table 4.4.

| Band(GHz) | V-pol | H-pol |
|---|---|---|
| **6.9** | *y = -5.61 x + 4.89* | *y = -22.42 x + 20.93* |
| **10.65** | *y = -6.79 x + 5.58* | *y = -24.62x + 22.41* |
| **18.7** | *y = -8.76x + 7.42* | *y = -27.84 x + 25.22* |
| **23.8** | *y = -9.85x + 8.47* | *y = -27.99 x + 25.40* |
| **36.5** | *y = -13.47 x + 12.41* | *y = -30.85 x + 28.79* |
| **89.0** | *y = -33.05x + 32.58* | *y = -45.20 x + 43.73* |

Table 4.9 Regression models for transmissivity and the mean value of $\Delta T_{b\text{-}vegetation}$ in each transmissivity interval

Table 4.10 shows the regression performance statistics for regression models in Table 4.9. The *SSE* for most of the bands are less than 10. The average $R^2$ of the bands is 0.9, which is close to 1. The *RMSE* for all the bands is lower than 3 K, the average value is 7 K less than for the regressions based on the aggregated paired data in Section 4.2.3.1.

| polarization | Frequency(GHz) | *SSE (K)* | $R^2$ | *RMSE* (K) |
|---|---|---|---|---|
| vertical | 6.9 | 6.58 | 0.57 | 1.15 |
| | 10.65 | 7.88 | 0.95 | 1.26 |
| | 18.7 | 4.18 | 0.76 | 0.91 |
| | 23.8 | 2.92 | 0.98 | 0.76 |
| | 36.5 | 2.21 | 0.91 | 0.66 |
| | 89.0 | 1.97 | 0.99 | 0.63 |
| horizontal | 6.9 | 2.14 | 0.93 | 0.65 |
| | 10.65 | 2.87 | 0.99 | 0.76 |
| | 18.7 | 2.18 | 0.96 | 0.66 |
| | 23.8 | 5.07 | 0.98 | 1.01 |
| | 36.5 | 29.63 | 0.91 | 2.43 |
| | 89.0 | 38.37 | 0.94 | 2.77 |
| **Average** | | 8.83 | 0.90 | 1.14 |

Table 4.10 Goodness of fit for regression models for transmissivity and the mean value of $\Delta T_{b\text{-}vegetation}$ in each transmissivity interval

| | | | | | | | |
|---|---|---|---|---|---|---|---|
| vertical | Frequency (GHz) | 6.9 | 10.65 | 18.7 | 23.8 | 36.5 | 89 |
| | P value | 0.0489 | 0.000224 | 0.0111 | 1.27E-05 | 0.000929 | 2.61E-06 |
| horizontal | Frequency (GHz) | 6.9 | 10.65 | 18.7 | 23.8 | 36.5 | 89 |
| | P value | 0.000504 | 6.44E-06 | 0.000119 | 1.63E-05 | 0.000813 | 0.000344 |

Table 4.11 P values between transmissivity and the mean value of ΔTb-vegetation in each transmissivity interval

Finally, Table 4.11 shows that the calculated, *P* values for all the bands are less than 0.05, which indicates that transmissivity and the mean value of $\Delta T_{b\text{-}vegetation}$ are related at all the bands. Compared with Table 4.6, *P* values between transmissivity and the

mean value of $\Delta T_{b\text{-}vegetation}$ in each transmissivity interval are than $P$ values between transmissivity and $\Delta T_{b\text{-}vegetation}$. It is because when calculate $P$ values between transmissivity and $\Delta T_{b\text{-}vegetation}$, the sample size is 2846 (total pixels in transects), but when calculate $P$ values between transmissivity and the mean value of $\Delta T_{b\text{-}vegetation}$, the sample size is 7 (midpoint of transmissivity and mean value of $\Delta T_{b\text{-}vegetation}$ for each interval). Larger sample size can decrease $P$ value.

### 4.2.4 Application of $\Delta T_{b\text{-}vegetation}$ calculations at the northern hemisphere

#### 4.2.4.1 Correction map produced by regression models of $\Delta T_{b\text{-}vegetation}$ and transmissivity value

Fig.4.14 and Fig.4.15 are the correction maps calculated by the regression models represented in Table 4.7. These figures represent how much brightness temperature contributed by vegetation at different bands and different location. The vegetation's influence on AMSR-E's measurement can be corrected by subtracting the value of $\Delta T_{b\text{-}vegetation}$ which represented in correction map.

According to Fig.4.14 and Fig.4.15, the value of $\Delta T_{b\text{-}vegetation}$ in the high vegetation density area (boreal forest belt and near equator) is higher than low vegetation density area. Vegetation has a greater influence on higher frequency bands compared with the lower frequency bands, especially at 89 GHz bands for which the influence of vegetation has a strong effect (steeper slope) in the regression line. Compared with vertical polarized bands, horizontal polarized bands are more sensitive to vegetation.

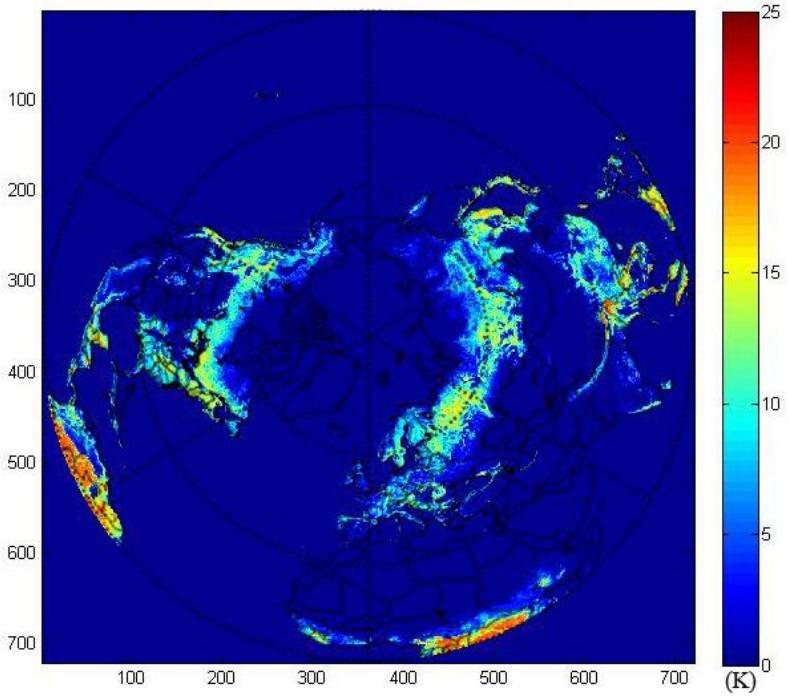


18GHz H-pol

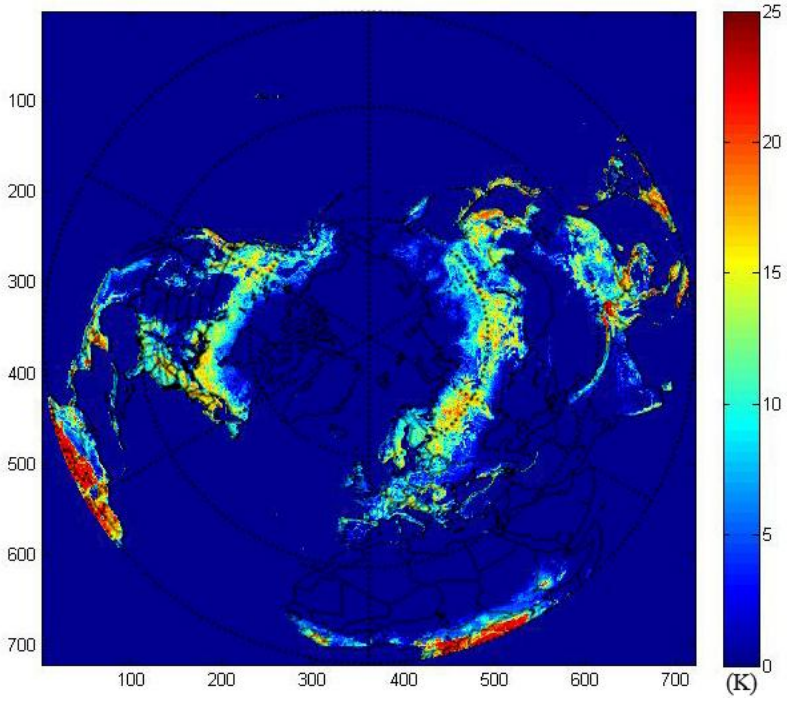


36GHz H-pol

Fig.4.14 Correction map produced by regression models of $\Delta T_{b\text{-}vegetation}$ and transmissivity value at horizontal polarization

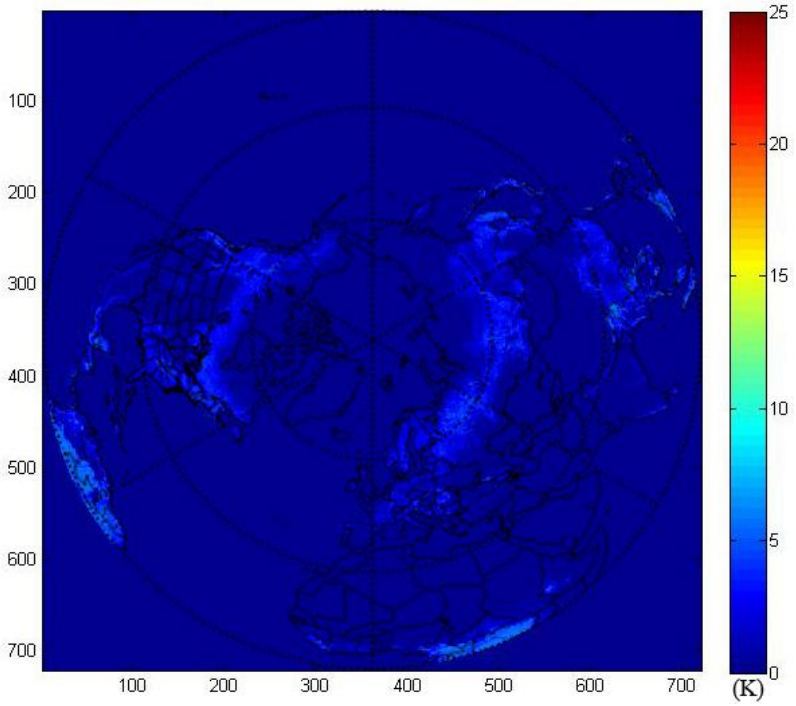


18GHz V-pol

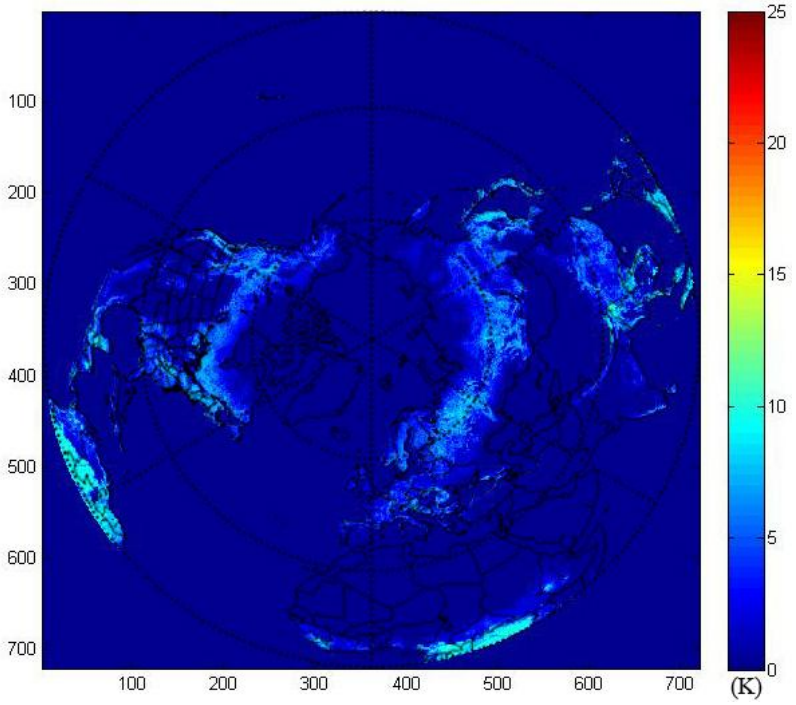


36GHz V-pol

Fig.4.15 Correction map produced by regression models of $\Delta T_{b\text{-}vegetation}$ and transmissivity value at vertical polarization

#### 4.2.4.2 Correction map produced by the regression model of mean value of $\Delta T_{b\text{-}vegetation}$ for each interval and transmissivity value

Fig.4.17 Correction map produced by regression models of mean values of $\Delta T_{b\text{-}vegetation}$ and transmissivity values for each interval at vertical polarization Fig.4.16 and Fig.4.17 are the correction maps calculated by regression models which were represented in Table 4.8. Fig.4.16 and Fig.4.17 also represent how much brightness temperature contributed by vegetation at different bands and different location as Fig.4.14 and Fig.4.15. The difference is that the models in Table 4.7 are the regression models between $\Delta T_{b\text{-}vegetation}$ and transmissivity values but models in Table 4.8 are the regression models between transmissivity and mean values of $\Delta T_{b\text{-}vegetation}$ for each interval.

In the correction maps represented in Fig.4.16 and Fig.4.17, $\Delta T_{b\text{-}vegetation}$ has a similar response to vegetation density as correction maps represented in Figs. 4.14 and 4.15. But the derived corrections shown in the maps in Fig.4.16 and Fig.4.17 are weaker than those represented in Fig.4.14 and 4.15.

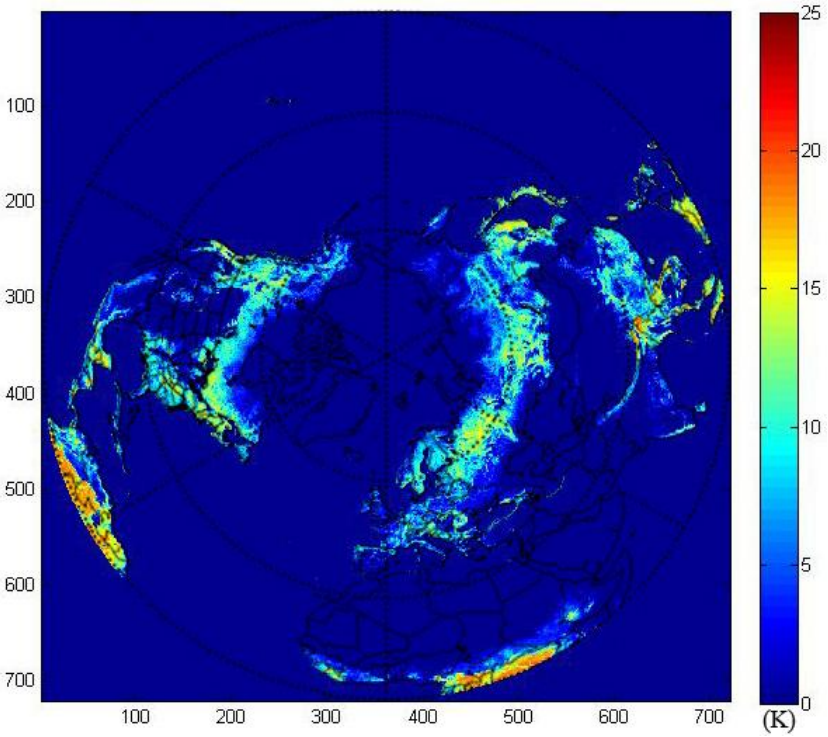


18GHz H-pol

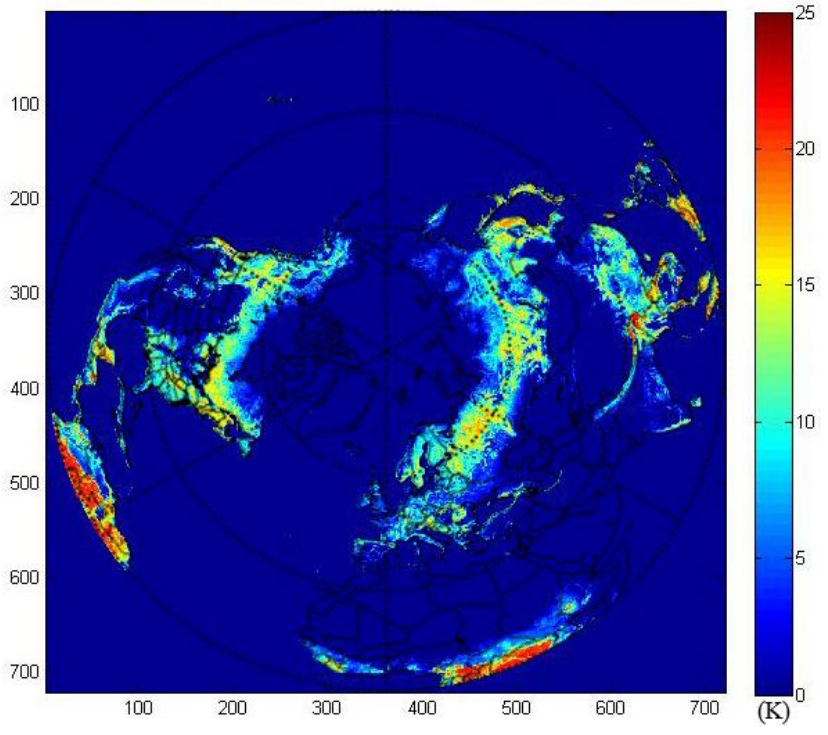


36GHz H-pol

Fig.4.16 Correction map produced by regression models of mean values of $\Delta T_{b\text{-}vegetation}$ and transmissivity for each interval at horizontal polarization

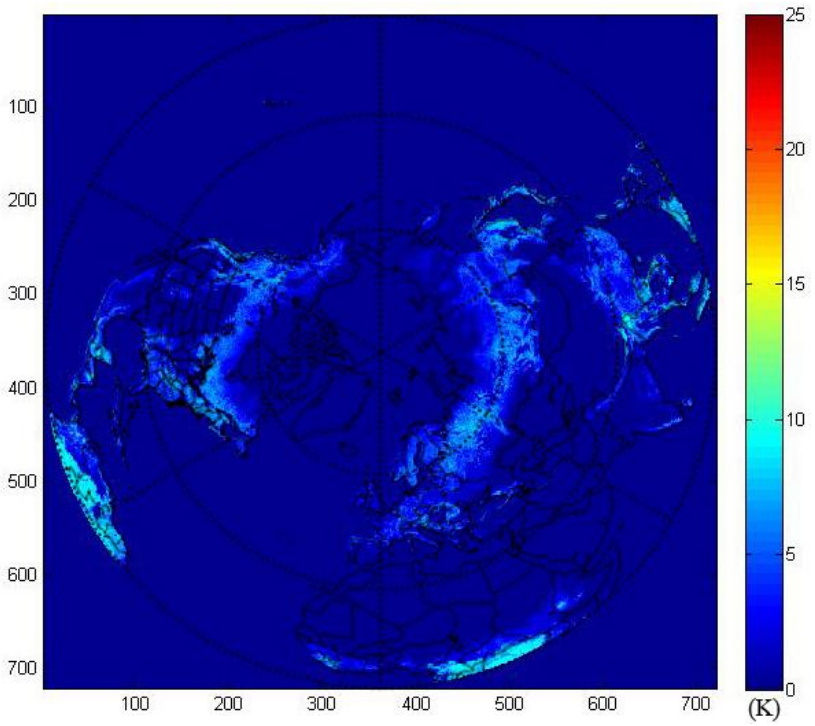


18GHz V-pol

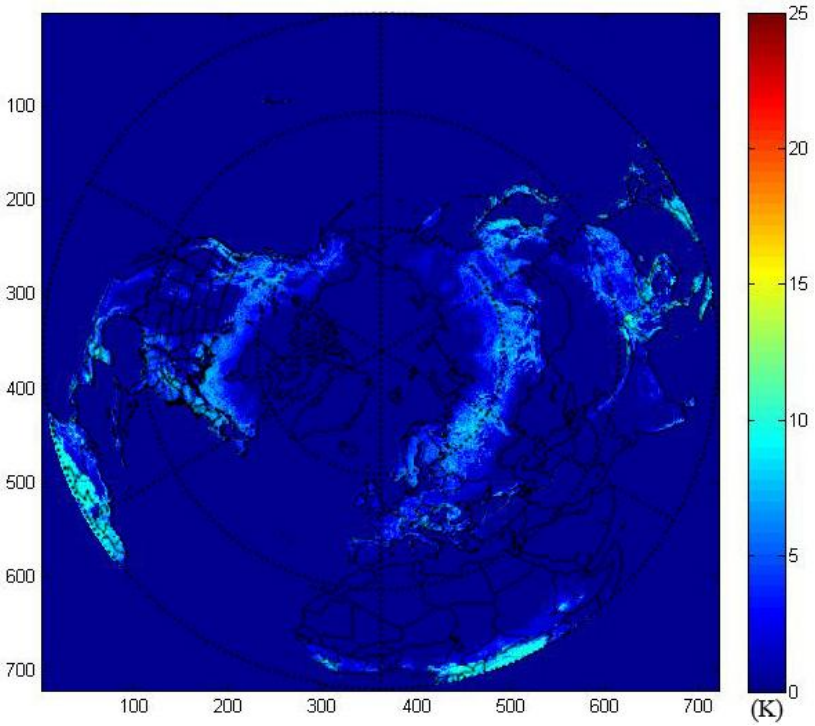


36GHz V-pol

Fig.4.17 Correction maps produced by regression of mean values of

$\Delta T_{b\text{-}vegetation}$ and transmissivity for each interval at horizontal polarization

## 4.3 Uncertainty assessment

The uncertainty assessment section will be discussed in two parts. The first part discusses the uncertainty in transmissivity retrieval, while the second part discusses the uncertainty in $\Delta T_{b\text{-}vegetation}$ estimation.

### 4.3.1 Uncertainty of transmissivity estimated by the SCAmod method

#### 4.3.1.1 Change detection

Fig.4.18 represents forest coverage in the selected sampling area (34560000 $km^2$ in total, demonstrated in methodology part, Fig.3.2). According to this figure, forest coverage in the selected sampling area is about 11%. From 2002 to 2012, tree coverage slightly increased.

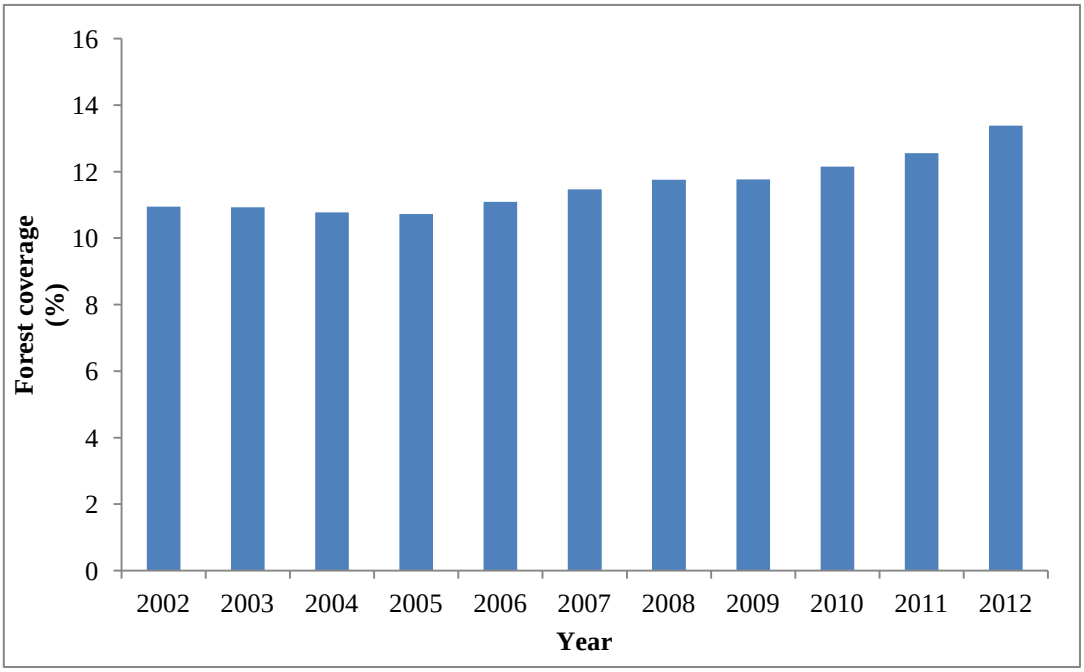


Fig.4.18 Annual forest coverage from MODIS MCD12Q1 IGBP data

Fig.4.19 provides more detail about the dynamic of forest coverage in selected areas from 2002 to 2012. In this case, 'Gain' means the percentage of new increased forest area (from un-forest coverage to forest coverage ) among the total selected area, and 'lost' means the percentage of new decreased forest area (forest coverage changed into un-forest coverage) among the total selected area.

Forest coverage has not changed dramatically over the 10-year period and has experienced both gains and losses with the net change remaining positive. But in general, forest coverage is stable.

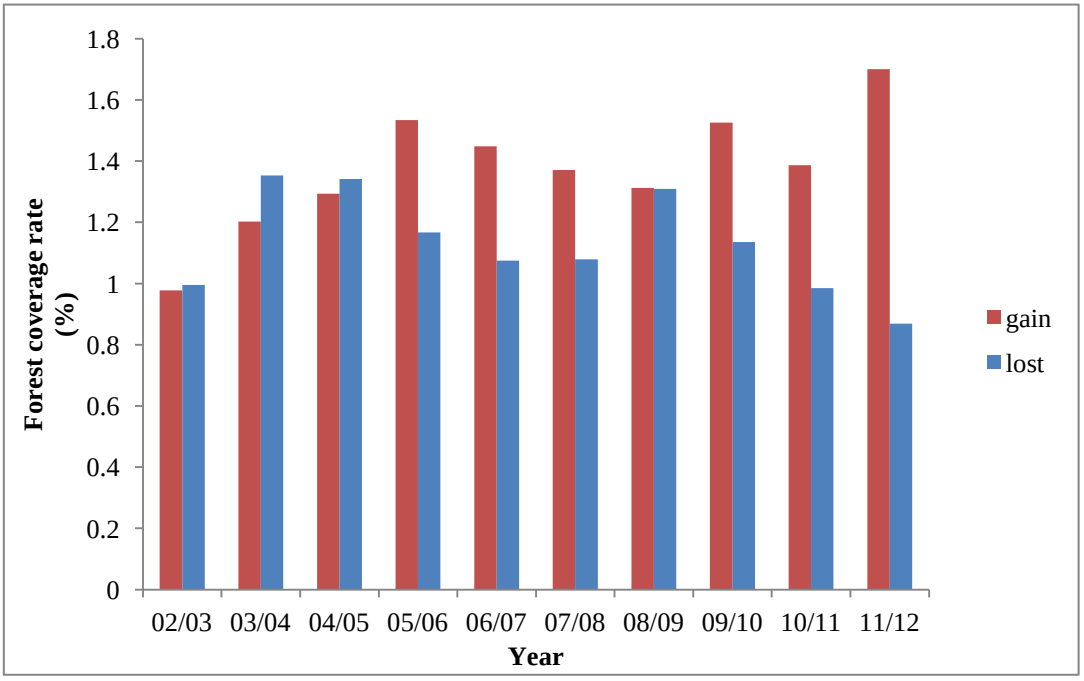


Fig.4.19 Annual variations in area of increased and decreased forest percentage from MODIS MCD12Q1 IGBP data

MOD09A1 reflectance data from 2010-2013 during winter time was used for transmissivity retrieval. Although forest coverage changed during this period, at a rate

of change of 1% per year, the change will not become a major source of uncertainty for transmissivity retrieval. Any land cover change will cause a change in reflectance values which can be detected by law of error propagation with statistical perspective.

#### 4.3.1.2 Statistical estimation of uncertainty

a) Forest transmissivity

Fig.4.20 represent the variance of transmissivity square which was calculated by the law of error propagation in statistical accuracy assessment. According to this figure, $S^2(t^2)$ is less than 2 in most areas.

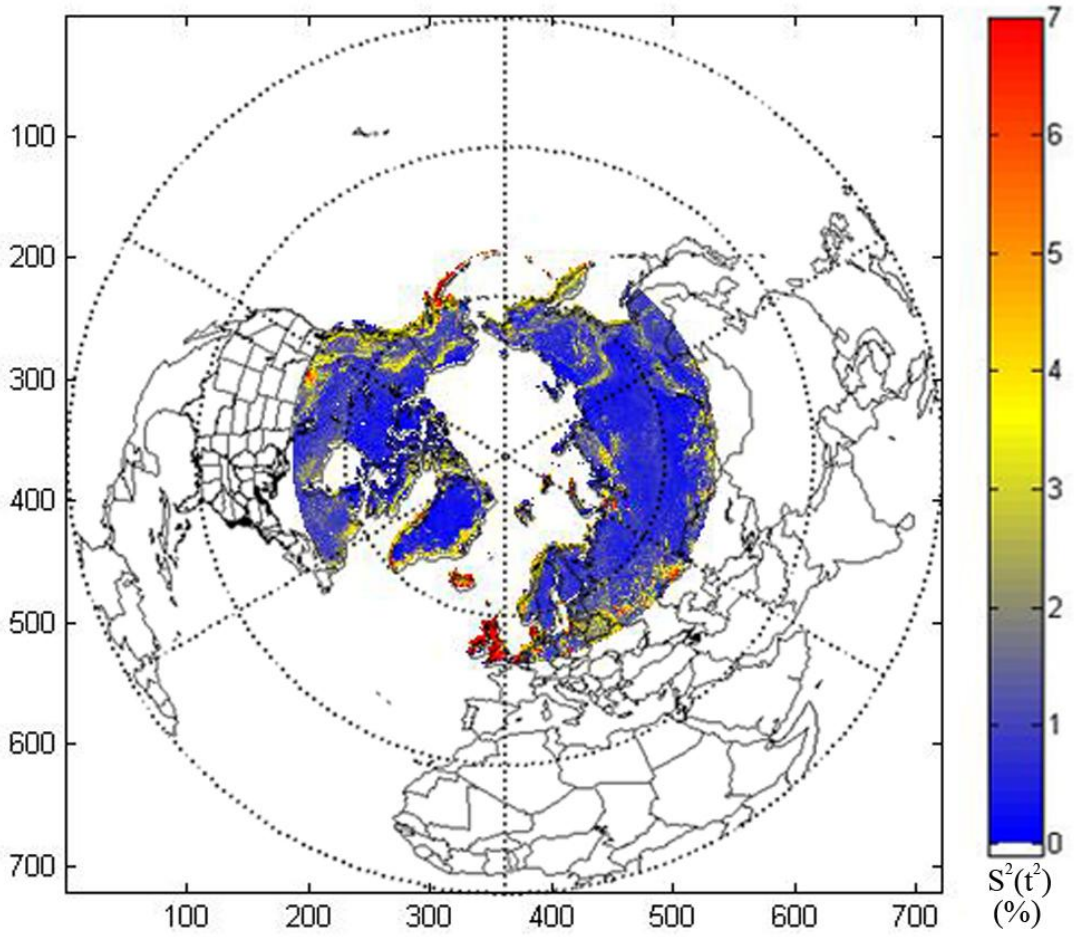


Fig.4.20 Uncertainty assessment for forest transmissivity estimated by SCAmod method

Areas which are near the water body and in mountain regions (*e.g.* Rocky Mountain) have the largest uncertainties. The low latitude regions also tend to have higher variance than higher latitude regions.

b) Variance distribution at different transmissivities

Fig.4.21 demonstrates how variance is distributed with different transmissivity values. According to this figure, the variance of most points is less than 10, very few points higher than 30. The variance of transmissivity is distributed evenly in the whole range of transmissivity value which means the variance is related to the quality of input data.

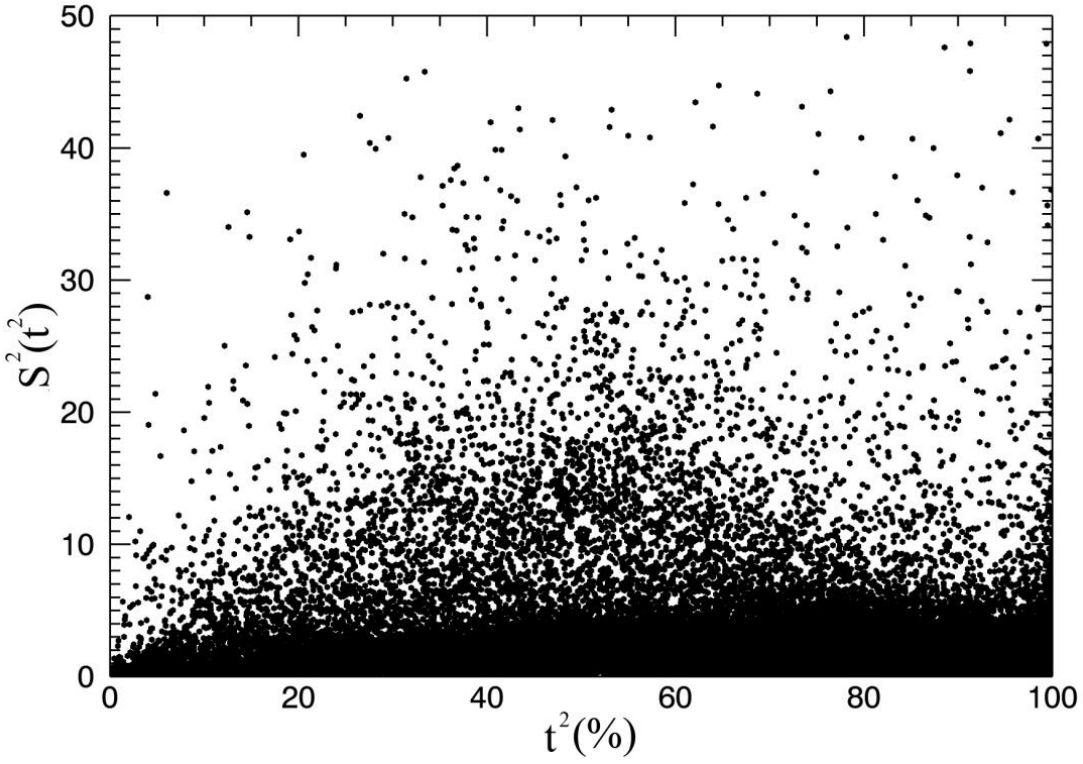


Fig.4.21 Variance of transmissivity distributed with transmissivity value

### 4.3.2 Uncertainty in $T_{b\text{-}vegetation}$ estimation

The variance of $T_{b\text{-}vegetation}$ was contributed by the variance of ground and variance of standardized brightness temperature ($T_{b\text{-}standardized}$). Thus, the variance of ground, the variance of $T_{b\text{-}standardized}$ and the total variance in $T_{b\text{-}vegetation}$ are separately discussed:

4.3.2.1 Variance of ground

Table 4.12 and Table 4.13 shows the variance of $T_{b\text{-}ground}$.

| | | Frequency(GHz) | | | | | |
|---|---|---|---|---|---|---|---|
| Transect ID | Sample size | **6.9** | **10.65** | **18.7** | **23.8** | **36.5** | **89** |
| 1 | 158 | 18.11 | 15.81 | 14.49 | 13.02 | 20.34 | 155.96 |
| 2 | 106 | 53.46 | 41.77 | 21.64 | 11.58 | 11.97 | 56.99 |
| 3 | 88 | 72.06 | 60.82 | 81.59 | 57.84 | 59.15 | 139.10 |
| 4 | 68 | 39.18 | 34.57 | 31.84 | 27.02 | 47.21 | 103.85 |
| 5 | 72 | 96.59 | 115.46 | 115.47 | 81.94 | 52.09 | 22.51 |
| 6 | 36 | 37.73 | 65.30 | 74.41 | 52.48 | 49.04 | 36.74 |
| 7 | 65 | 15.55 | 17.00 | 12.68 | 9.05 | 10.89 | 89.77 |
| 8 | 52 | 35.95 | 15.39 | 10.46 | 11.16 | 30.19 | 183.82 |

Table 4.12 Variance of brightness temperature of ground at vertical polarization

| | | Frequency(GHz) | | | | | |
|---|---|---|---|---|---|---|---|
| Transect ID | Sample size | **6.9** | **10.65** | **18.7** | **23.8** | **36.5** | **89** |
| 1 | 158 | 23.89 | 20.28 | 18.34 | 17.15 | 28.17 | 154.28 |
| 2 | 106 | 127.07 | 103.80 | 64.45 | 39.73 | 25.50 | 35.12 |
| 3 | 88 | 116.97 | 119.25 | 110.97 | 88.51 | 98.04 | 120.41 |
| 4 | 68 | 111.44 | 107.44 | 112.96 | 90.62 | 145.29 | 148.62 |
| 5 | 72 | 128.62 | 111.69 | 95.23 | 93.19 | 69.63 | 50.51 |
| 6 | 36 | 52.57 | 104.60 | 145.55 | 115.32 | 131.25 | 86.64 |
| 7 | 65 | 31.58 | 40.16 | 47.03 | 40.23 | 58.59 | 112.63 |
| 8 | 52 | 108.45 | 55.13 | 47.33 | 47.12 | 75.14 | 202.18 |

Table 4.13 Variance of $T_b$ of ground at horizontal polarization

Figs. 4.22 and 4.23 show variance the data in graphical form. According to Fig.4.3 and Fig.4.4, $T_{b\text{-}ground}$ in H-polarized bands tend to have higher variances than V-polarized bands. With the exception of transects 5 and 6, the 89 GHz bands tend to have a greater variance compared with lower frequency bands. This tendency is more evident at horizontal polarization.

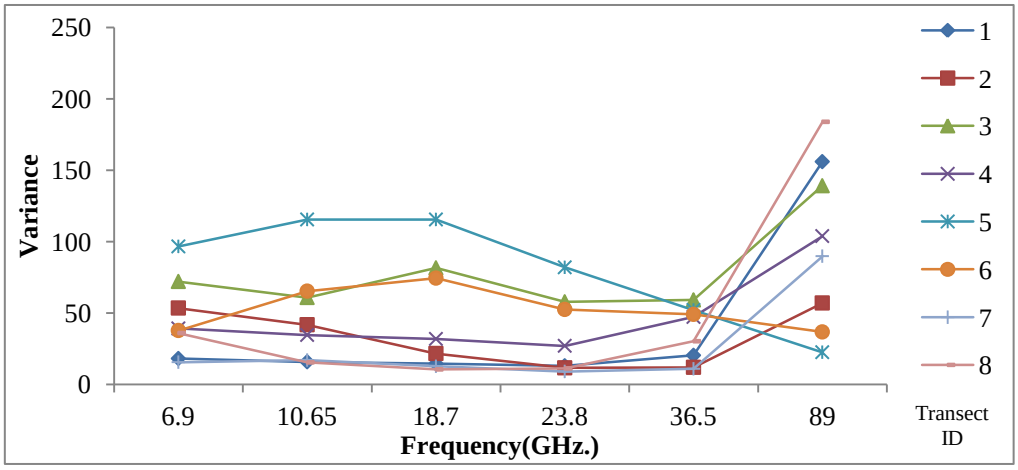


Fig.4.22 Variance of brightness temperature of ground at vertical polarization

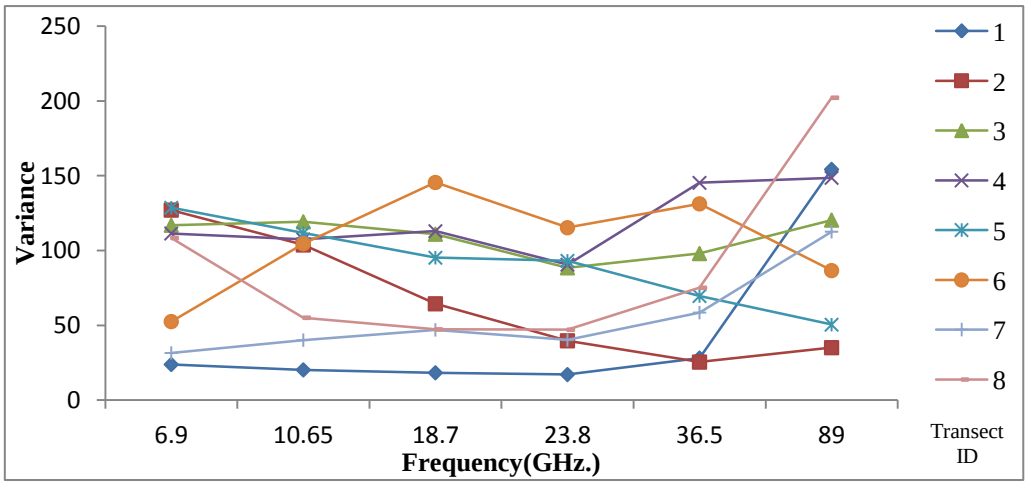


Fig.4.23 Variance of brightness temperature of ground at horizontal polarization

#### 4.3.2.2 Variance of $T_{b\text{-}standardized}$

Table 4.14 are the values of $S^2(T_{b\text{-}standardized})$ for each transect. This value was calculated by equation 3.16, and was used by equation 3.17 to calculate $S^2(\Delta T_{b\text{-}vegetation})$. In Table 4.14, sample size means the number of pixels was selected at each transect. $\Delta T$ is the difference between highest temperature value and lowest temperature inside each transect. Variance is the variance of $S^2(T_{b\text{-}standardized})$.

| **Transect ID** | **Sample size (pixels)** | $\Delta T(K)$ | **variance** |
|---|---|---|---|
| 1 | 568 | 13.22 | 0.05 |
| 2 | 304 | 12.08 | 0.05 |
| 3 | 392 | 14.72 | 0.06 |
| 4 | 504 | 12.54 | 0.05 |
| 5 | 344 | 12.92 | 0.05 |
| 6 | 244 | 13.02 | 0.05 |
| 7 | 400 | 14.98 | 0.07 |
| 8 | 276 | 13.70 | 0.06 |

Table 4.14 The value of $S^2(T_{b\text{-}standardized})$ for each transect

According to Table 4.14, differences between highest temperature value and lowest temperature value inside each transect are less than 15 K, and $S^2(T_{b\text{-}standardized})$ is less than 0.07 for each band.

#### 4.3.2.3 Total variance in $\Delta T_{b\text{-}vegetation}$

Table 4.15 and Table 4.16 are the $S^2(\Delta T_{b\text{-}vegetation})$ for each transect at each band. This value was calculated from equation 3.17, and was used by equation 3.18 to calculate the overall accuracy of $\Delta T_{b\text{-}vegetation}$ for each band.

| | Frequency(GHz) | | | | | |
|---|---|---|---|---|---|---|
| **Transect ID** | **6.9** | **10.65** | **18.7** | **23.8** | **36.5** | **89** |
| 1 | 18.16 | 15.87 | 14.54 | 13.07 | 20.39 | 156.01 |
| 2 | 53.51 | 41.82 | 21.68 | 11.63 | 12.01 | 57.03 |
| 3 | 72.12 | 60.88 | 81.65 | 57.91 | 59.21 | 139.16 |
| 4 | 39.23 | 34.62 | 31.89 | 27.06 | 47.25 | 103.89 |
| 5 | 96.64 | 115.51 | 115.52 | 81.99 | 52.14 | 22.56 |
| 6 | 37.79 | 65.35 | 74.46 | 52.54 | 49.09 | 36.79 |
| 7 | 15.61 | 17.07 | 12.75 | 9.11 | 10.96 | 89.84 |
| 8 | 36.00 | 15.44 | 10.51 | 11.22 | 30.24 | 183.87 |

Table 4.15 The value of $S^2(\Delta T_{b\text{-}vegetation})$ for each transect at vertical polarization bands

| | Frequency(GHz) | | | | | |
|---|---|---|---|---|---|---|
| **Transect ID** | **6.9** | **10.65** | **18.7** | **23.8** | **36.5** | **89** |
| 1 | 23.94 | 20.33 | 18.39 | 17.21 | 28.22 | 154.34 |
| 2 | 127.11 | 103.84 | 64.49 | 39.78 | 25.54 | 35.17 |
| 3 | 117.03 | 119.32 | 111.03 | 88.57 | 98.10 | 120.48 |
| 4 | 111.49 | 107.48 | 113.01 | 90.67 | 145.34 | 148.67 |
| 5 | 128.67 | 111.74 | 95.28 | 93.24 | 69.68 | 50.56 |
| 6 | 52.62 | 104.65 | 145.60 | 115.37 | 131.31 | 86.69 |
| 7 | 31.65 | 40.23 | 47.09 | 40.29 | 58.66 | 112.70 |
| 8 | 108.45 | 55.13 | 47.33 | 47.12 | 75.14 | 202.18 |

Table 4.16 The value of $S^2(\Delta T_{b\text{-}vegetation})$ for each transect at horizontal polarization bands

As Fig.4.24 and Fig.4.25 demonstrate, the values of $S^2(\Delta T_{b\text{-}vegetation})$ vary from 10 to 200 and depend on different bands and transects. The H-polarization bands tend to have

higher variance compared with the V-polarization bands. The 89 GHz bands tend to have higher variance compared with other bands.

Because the contribution of $S^2(T_{b\text{-}standardized})$ is small, the major source of uncertainty for $S^2(\Delta T_{b\text{-}vegetation})$ comes from $S^2(T_{b\text{-}ground})$.

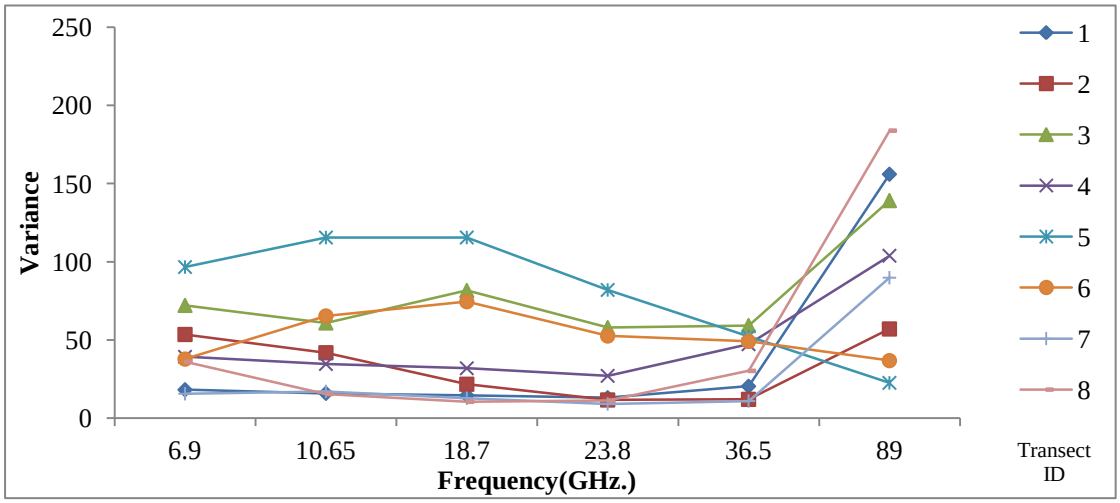


Fig.4.24 The value of $S^2(\Delta T_{b\text{-}vegetation})$ for each transect at vertical polarization bands

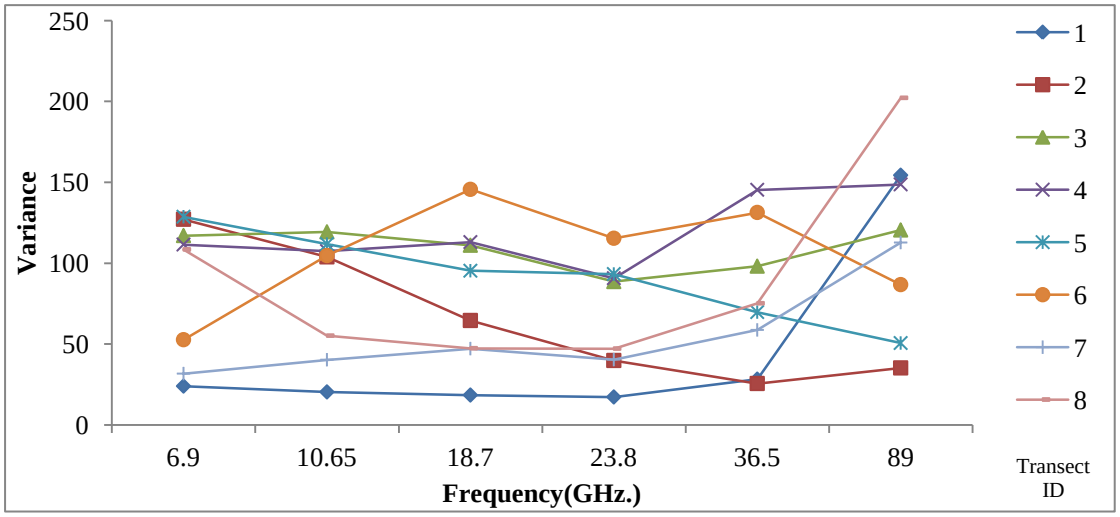


Fig.4.25 The value of $S^2(\Delta T_{b\text{-}vegetation})$ for each transect at horizontal polarization bands

Table 4.17 is the weighted average $S^2(\Delta T_{b\text{-}vegetation})$ for all the transects which was calculated by equation 3.18. these values were used to assess the overall quality of $\Delta T_{b\text{-}vegetation}$. Fig.4.26 shows the data in graphical form.

As Fig.4.26 represents, the H-polarization bands tends to have higher variance compared with V-polarization bands. The 89 GHz band tend to have higher variance compared with other bands.

| | Frequency(GHz) | | | | | |
|---|---|---|---|---|---|---|
| | **6.9** | **10.65** | **18.7** | **23.8** | **36.5** | **89** |
| **V-pol** | 44.59 | 42.22 | 40.81 | 29.77 | 32.13 | 105.98 |
| **H-pol** | 83.71 | 76.47 | 69.50 | 57.11 | 66.90 | 113.84 |

Table 4.17 The weighted average $S^2(\Delta T_{b\text{-}vegetation})$ for all the transects

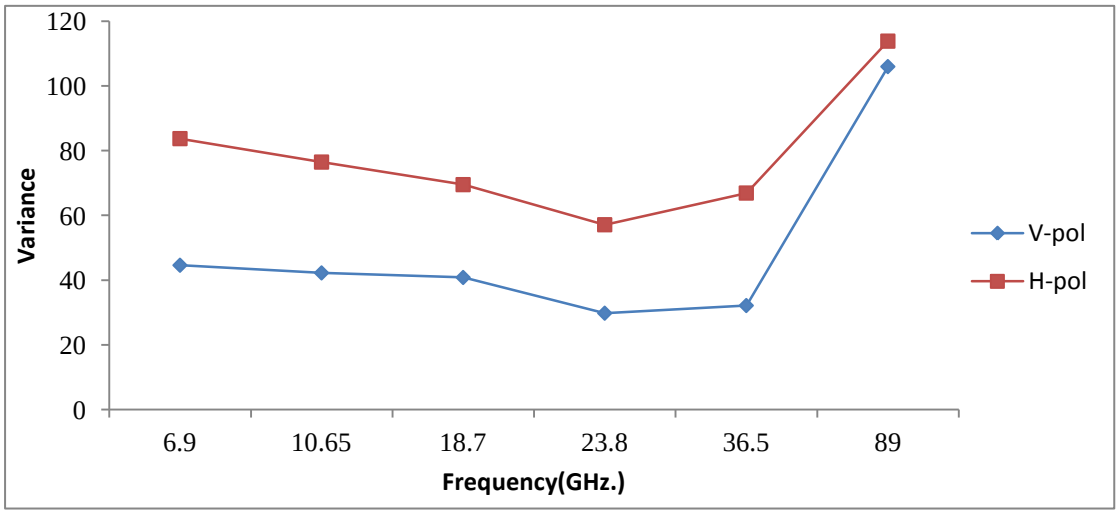


Fig.4.26 The weighted average $S^2(\Delta T_{b\text{-}vegetation})$ For all the transects

# Chapter 5: Discussion

## 5.1 Key findings

### 5.1.1 Correlation between transmissivity and forest fraction at 25 x 25 grid in Northen Hemisphere.

According to Fig.4.4 and the fitness assessment for equation 4.1, MOD44B data and transmissivity are significantly correlated. This means that MOD44B data can be used to estimate forest transmissivity at the 25x25 km grid. In SCAmod, transmissivity is a *regional* transmissivity, which means the transmissivity is calculated from the per-pixel scale (Metsamaki, *et al.*, 2012). At the scale of MODIS grid cells (500m) and EASE grid cells (25 x 25 km), landcover category is usually not a pure class. Both open areas (transmissivity ~1) outside a forest stand and canopy gaps (transmissivity ~1) within the forest stand contribute to the reflectance from the combined forest scene (transmissivity <<1) during the SCAmod transmssivity estimation procedure. Thus, transmissivity actually includes information of both forest fraction and the transmissivity from the canopy. MOD44B (VCF) is designed to represent vegetation coverage globally at sub-pixel-level, thus it provides the percentage of forest fraction for each pixel, which means both SCAmod transmissivity and MOD44B include information about forest fraction, i.e. they are physically related. Furthermore, the green reflectance band (495-570 nm) was used in both SCAmod's transmissivity and MOD44B retrieval, meaning that the input data for SCAmod's transmissivity and

MOD44B potentially could be correlated. These are the reasons to explain why transmissivity estimated by SCAmod and MOD44B are correlated.

SCAmod was originally designed to estimate snow coverage the forest regions since forest coverage is one of the challenges in snow mapping. Canopy can block the reflectance from the ground to the satellite sensor and can contribute its own reflectance. Thus, snow is mapped with lower accuracy in forested areas than in non-forested areas (Metsamaki, *et al.*, 2012). The SCAmod method has proven that can improve the accuracy of snow mapping based on the tests in European and Russia (Metsämäki, *et al.*, 2005, 2012). Thus, application of this model at regional to global scales should help to improve the accuracy of snow mapping.

Transmissivity estimation is one of the most challenging procedures for applying SCAmod at the global scale because it requires grid cells at full snow covered conditions. To select data with both cloud free and full snow covered condition is very time consuming. Metsämäki *et al.* (2012) tried to simplify this procedure by estimating transmissivity based on land cover type, but the variation inside each land cover type is difficult to characterize using information on land cover type alone.

With the regression model between transmissivity and MOD44B data developed in this thesis, an estimation procedure for transmissivity using SCAmod can be generalized and used to extend the application of the SCAmod method from regional to global scales. With this outcome, a goal of this thesis, therefore, is to apply the

transmissivity estimates to correct passive microwave brightness temperature in forest regions.

### 5.1.2 The influence of forest transmissivity on PM brightness temperature.

The influence of forest cover on PM measurement was examined by exploring the relationship between $\Delta T_{b\text{-}vegetation}$ and forest transmissivity. The relationship between $\Delta T_{b\text{-}vegetation}$ and forest transmissivity for all paired observations has been represented in Figs. 4.10, 4.11, and the relationship between $\Delta T_{b\text{-}vegetation}$ and forest transmissivity for transmissivity-aggregated data were shown in Figs. 4.12, 4.13. The regression models for those two kinds of regression approaches are represented in Tables 4.4 and 4.9.

According to goodness of fit tests in Table 4.5 and *P* value in Table 4.6, $\Delta T_{b\text{-}vegetation}$ and transmissivity are correlated, but the regressions do not account for all the variability . Goodness of fit (Tables 4.5 and 4.10) indicated that $\Delta T_{b\text{-}vegetation}$ and forest transmissivity for transmissivity-aggregated data have better goodness of fit measures. Furthermore, according to the result of skewness and kurtosis in Tables 4.7 and 4.8, the samples in each transmissivity interval are not significantly skewed, which means the mean value of $\Delta T_{b\text{-}vegetation}$ can be used to represent $\Delta T_{b\text{-}vegetation}$ for studying the relationship between $\Delta T_{b\text{-}vegetation}$ and forest transmissivity. For these reasons, regression models in Table 4.9 probably more reliable.

According to the results represented in Section 4.2.3, forest canopy increases brightness temperature in PM measurements especially at 36 and 89 GHz channels. In general, forest transmissivity is negatively correlated to $\Delta T_{b\text{-}vegetation}$ indicating that

higher density vegetation (lower transmissivity) tends to contribute more brightness temperature emission to the AMSR-E's observations. This finding is supported by the works of Ferrazzoli and Guerriero (1996) and Kruopis *et al.* (1999). Ferrazzoli and Guerriero (1996) tested the relationship between emissivity and dry biomass at L band. According to this study, emissivity increased with increased biomass (assuming it is related to transmissivity) which means that higher density forest tends to have a higher emissivity at PM band measurements. Kruopis (1999) also found a similar tendency based on EMAC-94/95 data. Therefore, these studies support the finding that transmissivity is negatively correlated with $\Delta T_{b\text{-}vegetation}$. However, PM responses at different frequencies and polarizations are not equally influenced by vegetation. Forest cover tends to increase brightness temperature more strongly in H-pol than V-pol. Furthermore, the relationship between frequency and $\Delta T_{b\text{-}vegetation}$ indicates that in higher frequency bands, vegetation tends to contribute more brightness temperature than lower frequency bands. This finding is matched with the work of Foster *et al*. (1991), and Chang *et al*. (1996).

### 5.1.3 Correction of PM brightness temperatures for snow property estimation.

The original principle of *SWE* retrieval is based on the linear relationship between the differences of the 18 and 37 GHz H-pol brightness temperature and *SWE* values (Chang, *et al.*, 1996) through a transfer function *f*:

$$SWE = f\,(T_{b\text{-}18H} - T_{b\text{-}37H}) \qquad (5.1)$$

However, as explained above, forest coverage tends to increase brightness temperatures in higher frequency bands than lower frequency bands, which means forest coverage will contribute more brightness temperature in $T_{b\text{-}18H}$ than $T_{b\text{-}37H}$. Thus, the value of ($T_{b\text{-}18H}$ - $T_{b\text{-}37H}$) will decrease due to the influence of vegetation. The relationship between $\Delta T_{b\text{-}vegetation}$ at different frequencies and forest transmissivity can explain the reason for the *SWE* underestimation in forested regions.

The approach to use forest transmissivity from MODIS indicates the potential of applying SCAmod's transmissivity product in PM *SWE* retrievals. By introducing the regression model between $\Delta T_{b\text{-}vegetation}$ and forest transmissivity, the brightness temperature contributed by forest can be compensated for, and the forest's influence on e.g. $T_{18H}$-$T_{37H}$ can be largely corrected. Furthermore, because the principle of snow depth estimation is similar as *SWE* retrieval, at least for more simple retrieval formulations (Foster, *et al.*, 1997), transmissivity estimated by SCAmod also has the potential to be used to correct snow depth estimate with PM measurement.

## 5.2 Uncertainties

Uncertainty assessment is an important part of this study. In the transmissivity retrieval, the uncertainty assessment procedure was used to improve the reliability of the regression model of transmissivity and forest fraction by masking out unreliable values (Sections 3.2.3 and 4.1.2) . Furthermore, the uncertainty assessment also provided a guideline to improve the methodology by identifying sources of uncertainty quantitatively (In both transmissivity and $\Delta T_{b\text{-}vegetation}$ estimation).

This section is divided into two parts. In the first part (section 5.2.1), the uncertainties in transmissivity retrieval are discussed. In the second part (section 5.2.2), the uncertainties in $\Delta T_{b\text{-}vegetation}$ estimation is discussed.

### 5.2.1 Uncertainties in transmissivity retrieval

A land cover change detection method (section 3.4.1.1) and a statistical error estimation procedure (equation 3.11) were developed and applied to evaluate the uncertainties in transmissivity retrieval. The statistical procedure was used to detect high uncertainty pixels of output transmissivity data. This procedure analyzed the variance of each input variable of the model to estimate the variance of estimated transmissivity. Because the factors such as land cover change, variation in vegetation cover, variation in atmospheric conditions, and different incidence angles can increase the variance of input MODIS green reflectance data, uncertainties introduced by these factors were largely detected by this statistical procedure. According to Fig.4.20, areas which are near the water body and in mountain regions (*e.g.* Rocky Mountain) have highest uncertainty. The low latitude regions also tend to have higher variance than high latitude regions.The ground condition near water body is complex and unstable. The factors such as the variation of water levels, ephemeral plants in shallow water and variation of soil moisture will affect reflectance. In mountain areas, different incidence angles have higher influence on reflectance than plains region. High variance in lower latitude because SCAmod need the image with full snow coverage to drive. But this condition is less likely fulfilled in lower latitude area. According to the result of

land cover change detection, forest cover did not significantly change in recent years. Thus, based on the results of land cover change detection and statistical approach, although multiple reflectance data were used in SCAmod, the uncertainty analysis indicated that the data errors were minimized.

### 5.2.2 Uncertainties in $\Delta T_{b\text{-}vegetation}$ estimation

#### 5.2.2.1 H-pol and V-pol differences

The same statistical procedure was applied to evaluate the uncertainties in $\Delta T_{b\text{-}vegetation}$ estimation. According to Table 4.17 and Fig.4.26, in general the uncertainties in H-pol data are greater than at V-pol. This is because H-pol is more sensitive to the variation in surface variations (*e.g.* vegetation, roughness, water content). In studies by Roy *et al.* (2012) and Kim *et al.* (2008), similar behavior of the influence of vegetation PM measurements was found.

#### 5.2.2.2 Variations of ground status: sub-scale heterogeneity

Comparison of the results represented in section 4.3.2.1 with 4.3.2.2, to estimate the brightness temperature of the ground status introduced larger uncertainties than brightness temperature standardization procedure, which indicated that the ground can have a significant impact. Many ground status factors can introduce uncertainties: soil moisture variations, soil type variability, mixing of vegetation cover types and the presence of water bodies within AMSR's footprint. Many of these factors can combine to influence the ground surface emissivity. In this study, ground conditions under forest

canopy was assumed as the same as the nearby open area inside each transect. This assumption simplified the procedure to estimate $\Delta T_{b\text{-}vegetation}$, but also introduced uncertainties.

#### 5.2.2.3 Different behavior of transects.

According to Figs. 4.22 and 4.23, for all the transects except transects 4 and 6, $T_{b\text{-}ground}$ values tended to slowly decrease from 6.9 GHz to 89 GHz In transects 4 and 6, $T_{b\text{-}ground}$ increased with frequency. This tendency is especially apparent in the 89 GHz channels. According to the research of Mätzler *et al*. (1994) and Comiso *et al*. (1997) in passive microwave signatures, the emissivity of water and unfrozen soils increases with frequency whilst the emissivity of ice and frozen soil decrease with frequency. The behavior of transects 4 and 6 are potentially consistent with emissivity signatures of water and unfrozen soils with the remaining transects similar to ice and frozen soil. According to Table 4.3, although the average skin temperature form MODIS is lower than 273 K, temperatures could be greater than freezing point (273 K) in some locations. Furthermore, inside selected transects, water-ice and frozen-unfrozen soils could easily exist. Since 89 GHz channels have a higher spatial resolution than the lower frequencies, it may have a higher sensitivity to this kind of ground status variations. The increased brightness temperature variance at 89 GHz bands can also support this assumption (Figs. 4.22, 4.23, 4.24, 4.25). This finding indicates that the status of water bodies and soils may introduce further uncertainty in $\Delta T_{b\text{-}vegetation}$ retrieval procedure.

The water fraction inside each grid and the condition of soil status are sources of uncertainties.

## 5.3 Limitations

Although progress has been made, limitations still remain from this work. First, the transmissivity data calculated in this research are based on visible-infrared reflectance data. While the applicability has been demonstrated, the ideal approach would be to have a simple passive microwave based model. The challenge, however, is that high spatial resolution passive microwave data at the forest scale are not available regionally or globally. MODIS data, despite their limited wavelength for microwave applications, are available. Second, the microwave emissivity data in this study are monthly data, but the condition of land surface in October changes rapidly. For this month, the temperature in some area will vary around freezing point (273 K), which means the emissivity of the ground might be variable as soils vary spatially between frozen and unfrozen states. Therefore, monthly emissivity may not be optimal in some locations. Finally, the canopy structures of deciduous trees have larger variations than coniferous trees. The canopies of deciduous trees, therefore, may change from October to winter season as trees may continue to senescence, although at higher latitudes this may be less of an issue. Further work on these topics is needed.

## 5.4 Future work

As discussed above, water is one of the factors introduced uncertainties. Although high percentage water grid cells (percentage of water greater than 50%) are masked out

based on reprojected IGBP MODIS landcover data, water mostly exists in every grid cell at the scope of 25 x 25 km grid. Therefore, finding an appropriate threshold or standard is necessary.

At higher frequencies (36 GHz and 89GHz especially), cloud scattering ice crystals can affect upwelling radiation as well. Therefore, cloud cover also could be one of the sources of uncertainty in the $T_b$ response of the high frequency bands. Although cloud cover areas were carefully avoided when selecting transects, some exploration about how cloud cover could affect PM measurement will be beneficial in the future.

The frozen and unfrozen state of water and soil is another source of uncertainty. Current work indicated that the skin and soil temperatures should be more carefully considered, although this is challenging. In future work, the temperature within all transects should be consistent: either below or above freezing point.

In addition to increasing the accuracy of $\Delta T_{b\text{-}vegetation}$ estimation, the optical transmissivity data estimated by SCAmod has the potential for application to physical models. HUT model or the $\omega$-$\tau$ model estimate vegetation transmissivity at PM frequencies based on the correlation between transmissivity and stem volume. Because the stem volume and optical transmissivity data estimated by SCAmod are potentially correlated, and transmissivity data estimated by SCAmod is globally available (unlike stem volume), further study of the relationship between stem volume and optical transmissivity may help to extend the application of physical based canopy models to global scale.

# Chapter 6: Conclusion

The purpose of this research was to explore a possible procedure to correct the influence of forest canopy in PM measurement. It started with the retrieval of forest transmissivity data with SCAmod. In SCAmod, the effective forest transmissivity can be determined with the reflectance of canopy at snow covered condition and three major contributors (generally applicable reflectance of wet snow, forest canopy and snow-free ground). In comparison with transmissivity estimation approaches that are reliant on ground-based measurement or models, this model can be applied globally based on MODIS reflectance data. However, because SCAmod needs reflectance observations from snow covered conditions, it can only be applied in mid to high latitude regions. MOD44B data were used to extend this transmissivity data to lower latitude areas because MOD44B data and transmissivity data are correlated. The regression model between MOD44B and transmissivity has been represented in this thesis. This regression model can be used to extend transmissivity data into lower latitude area, and can be used to simplify transmissivity estimate procedure of SCAmod also.

Finally, by comparing the PM brightness temperatures in open areas with forest covered areas the brightness temperature contribution from vegetation was calculated and observed to increase with increased forest vegetation spatial density. It was noted that forest canopy tends to contribute more brightness temperature emission in H-pol than V-pol bands. Also, at higher frequencies, vegetation typically contributes more

brightness temperature than at lower frequencies. Although water fraction and soil state (frozen or unfrozen) may introduce additional uncertainties, quantification of these forest attenuation contributions, as achieved in this thesis, can be used to help reduce *SWE* or *SD* estimation uncertainty in forested regions.

# Reference

Aoki, T., Aoki, T., Fukabori, M., Hachikubo, A., Tachibana, Y., & Nishio, F. (2000). Effects of snow physical parameters on spectral albedo and bidirectional reflectance of snow surface. *Journal Of Geophysical Research-Atmospheres, 105(D8),* pp. 10219-10236.

Ashcroft, P., & F. J. Wentz (2013). *AMSR-E/Aqua L2A Global Swath Spatially-Resampled Brightness Temperatures.* Version 3. Boulder, Colorado USA: NASA DAAC at the National Snow and Ice Data Center. http://dx.doi.org/10.5067/AMSR-E/AE_L2A.003.

Barnett, T. P., Dumenil, L., Schlese, U., Roeckner, E., & Latif, M. (1989). The effect of Eurasian snow cover on regional and global climate variations. *Journal of the Atmospheric Sciences, 46(5),* pp. 661-685.

Bernier, P. (1987). Microwave remote sensing of snowpack properties: potential and limitations. *Nordic Hydrology, 18(1),* pp. 1-20.

Betts, Alan K., & Ball, John H. (1997). Albedo over the boreal forest. *Journal of Geophysical Research, 102(D24),* pp. 28901-28909.

Bunting, J. T., & d'Entremont, R. P. (1982). *Improved Cloud Detection Utilizing Defense Meteorological Satellite Program near Infrared Measurements* (Environmental Research Papers No.765). Hanscom AFB, Massachusetts: Air force geophysics lab. Retrieved from www.dtic.mil/cgi-bin/GetTRDoc?AD=ADA118751

Butt, M., & Kelly, R. E. (2008). Estimation of snow depth in the UK using the HUT snow emission model. *International Journal of Remote Sensing, 29(14)*, pp. 4249-4267.

Kelly, R.E., Chang,A.T., Leung Tsang, Foster, J.L. (2003). A prototype AMSR-E global snow area and snow depth algorithm. *IEEE Transactions on Geoscience and Remote Sensing, 41(2)*, pp. 230-242.

Chang, A., Foster, J., & Hall, D. (1996). Effects of forest on the snow parameters derived from microwave measurements during the BOREAS Winter Field Campaign. *Hydrological Processes, 10(12)*, pp. 1565-1574.

Coll, C., Wan, Z., & Galve, J. (2009). Temperature-based and radiance-based validations of the V5 MODIS land surface temperature product. *Journal Of Geophysical Research-Atmospheres, 114* , pp. 1-15.

Comiso, J. C., Cavalieri, D. J., Parkinson, C. L., & Gloersen, P. (1997). Passive microwave algorithms for sea ice concentration: A comparison of two techniques. *Remote Sensing of Environment, 60(3)*, pp. 357-384.

Cracknell, A. P. (1997). *The advanced very high resolution radiometer (AVHRR)* (pp.14-26). London: Bristol.

Debbie, C. (2010). Global estimates of snow water equivalent from passive microwave instruments: History, challenges and future. *International Journal of Remote Sensing, 31(14)*, pp. 3707-3726.

Dietz, A. J., Kuenzer, C., Gessner, U., & Dech, S. (2012). Remote sensing of snow - a review of available methods. *International Journal of Remote Sensing, 33(13)*, pp. 4094-4134.

Eamer, J., Ahlenius, H., & Prestrud, P. (2007). *Global outlook for ice and snow.* Nairobi, Kenya: Division of Early Warning and Assessment DEWA, United Nations Environmental Programme.

Ferrazzoli, P., & Guerriero, L. (1996). Passive microwave remote sensing of forests: a model investigation. *IEEE Transactions on Geoscience and Remote Sensing, 34(2)*, pp. 433-443.

Folland, C. K., Karl, T. R., & Jim, S. M. (2002). Observed climate variability and change. *Weather, 57(8)*, pp. 269-278.

Foster, J. L., Chang, A.T.C., Hall, D.K. & Rango, A. (1991). Derivation of snow water equivalent in boreal forests using microwave radiometry. *Arctic, Annual, 44*, pp. 147-52.

Foster, J. L., Hall, D. K., & Chang, A. T. (1984). An overview of passive microwave snow research and results. *Reviews of Geophysics, 22(2)*, pp. 195-208.

Foster, J. L., Hall, D. K., & Chang, A. T. (1987). NIMBUS-7 SMMR derived global snow cover parameters. *Annuals of Glaciology*, pp. 39-44.

Foster, J. L., Hall, D. K., Chang, A., Rango, A., Wergin, W., & Erbe, E. (1999). Effects of snow crystal shape on the scattering of passive microwave radiation. *IEEE Transactions on Geoscience and Remote Sensing, 37(2)*, pp. 1165-1168.

Foster, J. L., Hall, D. K., Kim, E., Eylander, J. B., Riggs, G. A., Montesano, P. M., Nghiem, S.V., Tedesco, M., Kelly, R.E.J., Casey, K., Choudhury, B. (2011). A blended global snow product using visible, passive microwave and scatterometer satellite data. *International Journal of Remote Sensing, 32(5),* pp. 1371-1395.

Foster, J. L., Kelly, R., Chang, A., Dong, J., Powell, H., Sun, C., & Walker, J.P (2005). Quantifying the uncertainty in passive microwave snow water equivalent observations. *Remote Sensing of Environment, 94(2),* pp. 187-203.

Foster, J. L., Owe, M., & Rango, A. (1983). Snow cover and temperature relationships in North America and Eurasia. *Journal of Climate and Applied Meteorology, 22(3),* pp. 460-469.

Foster, J., Chang, A., & Hall, D. (1997). Comparison of snow mass estimates from a prototype passive microwave snow algorithm, a revised algorithm and a snow depth climatology. *Remote Sensing of Environment, 62(2),* pp. 132-142.

Foster, J., Liston, G., Koster, R., Essery, R., Behr, H., Dumenil, L., Verseghy, D.,Thompson, S., Pollard, D., & Cohen, J. (1996). Snow cover and snow mass intercomparisons of general circulation models and remotely sensed datasets. *Journal of Climate, 9(2),* pp. 409-426.

Garcia-Herrera, R., & Barriopedro, D. (2006). Northern Hemisphere snow cover and atmospheric blocking variability. *Journal Of Geophysical Research-Atmospheres, 111(D21),* pp.1-16.

Gloersen, P., & Barath, F. T. (1977). Scanning multichannel microwave radiometer for NIMBUS-G and SEASAT-A. *IEEE Journal of Oceanic Engineering, OE-2(2)*, pp. 172-178.

Goddard Space Flight Center. (2014). Retrieved from MODIS Land: http://modis-land.gsfc.nasa.gov/MODLAND_grid.html

Hall, D. K., Kelly, R. E., Foster, J. L., & Chang, A. T. (2005). Estimation of snow extent and snow. In M. G. Anderson, *Encyclopedia of Hydrological Sciences* (pp. 812-829). Chichester: John Wiley and Sons.

Hall, D. K., Riggs, G. A., & Salomonson, V. V. (1995). Development of methods for mapping global snow cover using moderate resolution imaging spectroradiometer data. *Remote Sensing of Envronment, 54(2)*, pp. 127-140.

Hansen, M. C., DeFries, R. S., Townshend, J. R. G., Carroll, M., Dimiceli, C., & Sohlberg, R. A. (2003). Global percent tree cover at a spatial resolution of 500 meters: first results of the MODIS vegetation continuous fields algorithm. *Earth Interactions, 7(10)*, pp.1-15.

Hollinger, J. P., Peirce, J. L., & Poe, G. A. (1990). SSM/I instrument evaluation. *IEEE Transactions on Geoscience and Remote Sensing, 28(5)*, pp.781-790.

Davies, T.D.(1994). Snow cover-atmosphere interactions. In Jones, H. G., Davies, T.D, Ohmura, A., Morris, E.M. *Snow and ice covers:interactions with the atmosphere and ecosystems* (pp.3-15). UK: IAHS Press.

Jones, H. G. (1999). The ecology of snow-covered systems:A brief overview of nutrient cycling and life in the cold. *Hydrological Processes, 13(14-15)*, pp. 2135-2147.

Karl, T. R., & Trenberth, K. E. (2003). Modern global climate change. *Science, 302(5651)*, 1719-1723.

Kelly, R. E. (2009). The AMSR-E snow depth algorithm: description and initial results. *Journal of the Remote Sensing Society of Japan, 29*, pp. 307-317.

Kerr, Y. H., Wigneron, J.-P., Pellarin, T., Kerr, Y. H., & Wigneron, J.-P. (2006). Global simulation of brightness temperatures at 6.6 and 10.7 GHz over land based on SMMR data set analysis. *IEEE Transactions on Geoscience and Remote Sensing, 44(9)*, pp. 2492-2505.

Kim, E. J., Durand, M., Kim, E. J., & Margulis, S. A. (2008). Quantifying uncertainty in modeling snow microwave radiance for a mountain snowpack at the point-scale, including stratigraphic effects. *IEEE Transactions on Geoscience and Remote Sensing, 46(6)*, pp. 1753-1767.

King, J.C., J.W.Pomeroy, D.M.Gray, C.Fierz, P.Fohn, R.Harding, R.Jordan, E.Martin, & C.Pluss (2008). Snow-atmosphere energy and mass balance. In R. L. Armstrong, & E. Brun (Eds), *Snow and Climate: Physical Processes, Surface Energy Echange and Modeling* (pp. 70-124). Cambridge: Cambridge University Press.

Kruopis, N. (1999). Passive microwave measurements of snow-covered forest areas in EMAC's 95. *IEEE Transactions on Geoscience and Remote Sensing, 37(6)*, pp. 2699-2705.

Kukla, G., & Gavin, J. (1981). Cool autumns in the 1970's. *Monthly Weather Review, 109(4)*, 903-908.

Lamb, H. H. (1972). Climate: present, past and future. In *Vol. 1.Fundamentals and climate Now* (pp.68-212). London: Methuen.

Langlois, A., Royer, A., Dupont, F., Roy, A., Goita, K., Dupont, F., & Picard, F. (2011). Improved corrections of forest effects on passive microwave satellite remote sensing of snow over boreal and subarctic regions. *IEEE Transactions on Geoscience and Remote Sensing, 49(10)*, pp. 3824-3837.

Liang, S., Fang, H., Chen, M., Shuey, C. J., Walthall, C., Daughtry, C., Morisette, J., Schaaf, C., & Strahler, A. (2002). Validating MODIS land surface reflectance and albedo products: Methods and preliminary results. *Remote Sensing of Environment, 83(1-2)*, pp. 149-162.

Lobl, E. (2001). Joint Advanced Microwave Scanning Radiometer (AMSR) science team meeting. *Earth Observer, 13(3)*, pp. 3-9.

Matson, M. (1991). NOAA satellite snow cover data. *Global and Planetary Change, 4(1-3)*, pp. 213-218.

Mätzler, C. (1994). Passive microwave signatures of landscapes in winter. *Meteorology and Atmospheric Physics, 54(1-4)*, pp. 241-260.

Mazurkiewicz, A. B., Callery, D. G., & McDonnell, J. J. (2008). Assessing the controls of the snow energy balance and water available for runoff in a rain-on-snow environment. *Journal of Hydrology, 354,* pp. 1-14.

Merritt, J. F. (1981). *Winter ecology of small mammals.* Pittsburgh: Carnegie Museum of Natural History.

Metsämäki, S. J., Anttila, S. T., Markus, H. J., & Vepsäläinen, J. M. (2005). A feasible method for fractional snow cover mapping in boreal zone based on a reflectance model. *Remote Sensing of Environment, 95(1),* pp. 77-95.

Metsamaki, S., Mattila, O. -P., Pulliainen, J., Niemi, K., Luojus, K., & Bottcher, K. (2012). An optical reflectance model-based method for fractional snow cover mapping applicable to continental scale. *Remote Sensing of Environment, 123,* pp. 508-522.

Mo, T., Choudhury, B., Schmugge, T., Wang, J., & Jackson, T. (2012). A model for microwave emission from vegetation-covered fields. *Journal of Geophysical Research, 87,* pp. 11229-11237.

Norouzi, H., Temimi, M., Rossow, W. B., Pearl, C., Azarderakhsh, M., & Khanbilvardi, R. (2011). The sensitivity of land emissivity estimates from AMSR-E at C and X bands to surface properties. *Hydrology and Earth System Sciences Discussions, 8(3),* p. 5667.

Pampaloni, P., & Paloscia, S. (1985). Microwave emission and plant water content: a comparison between field measurements and theory. *IEEE Transactions on Geoscience and Remote Sensing, GE-24(6)*, pp. 900-906.

Prigent, C., Rossow, W., & Matthews, E. (1997). Microwave land surface emissivities estimated from SSM/I observations. *Journal Of Geophysical Research-Atmospheres, 102(D18)*, pp. 21867-21890.

Pulliainen, J. T., & Grandel, J. (1999). HUT snow emission model and its applicability to snow water equivalent retrieval. *IEEE Transactions on Geoscience and Remote Sensing, 37(3I)*, pp. 1378-1390.

Qu, X., & Hall, A. (2007). What controls the strength of snow-albedo feedback? *Journal of Climate, 20(15)*, pp. 3971-3981.

Richard E, L. J. (1991). *Principles of Insect Low Temperature Tolerance.* US: Springer.

Roy, A., Royer, A., Langlois, A., Bergeron, J., Cliche, P., & Wigneron, J.-P. (2012, Sept.). A simple parameterization for a boreal forest radiative transfer model at microwave frequencies. *Remote Sensing of Environment, 124*, pp. 371-383.

Serreze, M. C., & Barry, R. G. (2014). *The Arctic climate system.* New York: Cambridge University Press.

Sommerfeld, R., Musselman, A., & Mosier, R. (1993). $CO_2$ , $CH_4$ and $N_2O$ flux through a Wyoming snowpack and implications for global budgets. *Nature, 361(6408)*, pp. 140-142.

Stephen, D. J., & Ross, B. D. (2007). Recent Northern Hemisphere snow cover extent trends and implications for the snow-albedo feedback. *34(22),* pp. 1-6.

Stiles, W., Ulaby, F., & Rango, A. (1981). Microwave measurements of snowpack properties. *Nordic Hydrology, 12(3),* pp. 143-166.

Strahler, A. (1999). MODIS land cover and land-cover change. In *MODIS Land Cover Product Algorithm Theoretical Basis Document (ATBD).* Boston: Center for Remote Sensing Department of Geography Boston University.

Sturm,M.,Benson,CS.(1997). Vapor transport, grain growth and depth-hoar development in the subarctic snow. *Journal of Glaciology, 43(143),* pp. 42-59

Taylor, J. R. (1997). *An introduction to error analysis: the study of uncertainties in physical measurements.* Sausalito, California: University Science Books.

Teruo, A., Tadao, A., Masashi, F., Akihiro, H., Yoshihiro, T., & Fumihiko, N. (2000). Effects of snow physical parameters on spectral albedo and bidirectional reflectance of snow surface. *Journal of Geophysical Research: Atmospheres, 105(D8),* pp. 10219–10236.

Treidl, R. A. (1970). A case study of warm air advection over a melting snow surface. *Boundary-Layer Meteorology, 1(2),* pp. 155-168.

Ulaby, F. T., & Jedlicka, R. (1984). Microwave dielectric properties of plant materials. *IEEE Transactions on Geoscience and Remote Sensing, GE-22(4),* pp. 406-415.

Vermote, E. F., Tanré, D., Deuzé, J. L., Herman, M., & Morcrette, J.-J. (1997). Second simulation of the satellite signal in the solar spectrum, 6s: an overview. *IEEE Transactions on Geoscience and Remote Sensing, 35(3),* pp. 675-686.

Wagner, A. J. (1973). The influence of average snow depth on monthly mean temperature anomaly. *Monthly Weather Review, 101(8),* pp. 624-626.

Walker, D., Halfpenny, J., Walker, M., & Wessman, C. W. (1993). Long-term studies of snow-vegetation interactions. *43(5),* pp. 287-301.

William, S. D. (1965). *Physical climatology.* Chicago: University of Chicago Press.

Winther, J. -G., Gerland, S., Ørbæk, J. B., Ivanov, B., Blanco, A., & Boike, J. (1999). Spectral reflectance of melting snow in a high Arctic watershed on Svalbard: Some implications for optical satellite remote sensing studies. *Hydrological Processes, 13(12-13),* pp. 2033-2049.